EXPERIMENTAL STUDIES OF PULSATILE FLOW CHARACTERISTICS OF AORTIC MODELS UNDER NORMAL AND DISEASED CONDITIONS

A Dissertation
Submitted to the Graduate Faculty
of the
North Dakota State University
of Agriculture and Applied Science

By

Ruihang Zhang

In Partial Fulfillment of the Requirements
for the Degree of
DOCTOR OF PHILOSOPHY

Major Department:
Mechanical Engineering

June 2021

Fargo, North Dakota

North Dakota State University
Graduate School

Title

EXPERIMENTAL STUDIES OF PULSATILE FLOW CHARACTERISTICS OF AORTIC MODELS UNDER NORMAL AND DISEASED CONDITIONS

By

Ruihang Zhang

The Supervisory Committee certifies that this ***disquisition*** complies with North Dakota State University's regulations and meets the accepted standards for the degree of

DOCTOR OF PHILOSOPHY

SUPERVISORY COMMITTEE:

Dr. Yan Zhang
Chair

Dr. Yildirim Bora Suzen

Dr. Yechun Wang

Dr. Zhibin Lin

Approved:

10/20/2021
Date

Dr. Alan Kallmeyer
Department Chair

ABSTRACT

Heart disease is the leading cause of death globally. Aorta is extremely important because of its critical function in blood circulation. Abnormal hemodynamics of aortic valve and arch is related to many severe diseases and has intrigued a growing of fluid dynamic researches over decades. However, due to the complexity of transient flow and fluid-structure interaction, many aspects of aortic hemodynamics have not been fully understood. The goal of this dissertation is to design and construct an in-vitro cardiovascular flow simulator for PIV hemodynamics research and understand the pulsatile flow characteristics of human aortic valve and arch under normal and diseased conditions.

First, we investigated the fluid dynamics of a complaint aortic root model under varied cardiac outputs. High turbulence kinetic energy was observed after peak systole. A reduction in cardiac outputs resulted in a lower post-systole turbulence, smaller circumferential deformation, smaller geometric orifice area, and a shortened valve-opening period.

Second, we investigated the pulsatile flow through stenotic aortic valve models. Results indicated that a severe prosthetic stenosis causes significant changes in the flow fields downstream. The hemodynamic changes, e.g., increased jet velocity and viscous shear stress, were associated with the stiffened leaflet materials, rather than the stent base structure.

Third, we presented a combined experimental and numerical study of the pulsatile flow characteristics within Gothic and Romanesque aortic arch models. The results revealed significantly different primary and secondary flow characteristics between two models. Low and oscillatory wall shear stress and the abnormal secondary flow in the Gothic arch are correlated to vascular endothelial cell remodeling and might provide hints to the increased risks of atherosclerosis, late systemic hypertension, and other cardiovascular complications.

Overall, this dissertation provides physical insights into pulsatile flow characteristics through aortic valve and arch models under varied normal and diseased conditions. In-vitro experiments using PIV can capture prominent flow characteristics within prosthetic aortic models, providing better controllability and spatial resolution that complements clinical diagnosis and a source of validation for computational simulations. Future improvements of artificial models' designs and the advanced flow diagnostic techniques can further enhance the accuracy and credibility of in-vitro flow researches.

ACKNOWLEDGMENTS

I would like to express my greatest appreciation to my advisor Dr. Yan Zhang, whose professional and enthusiastic research attitude has taught me a lot during my Ph.D. study. This doctoral dissertation could not been finished without the guidance and help from him.

My deep appreciation goes to my committee members, Dr. Yildirim Bora Suzen, Dr. Yechun Wang, Dr. Zhibin Lin and Dr. Amanda Brooks, for their kind help during my Ph.D. period. I also would like to express my great thanks to them for evaluating my research and providing me wise and helpful comments for my research. In addition, CFD research credits of Chapter 5 go to Nick Thomas and Dr. Yildirim Bora Suzen.

I also want to thank the persons who help me at Mechanical Engineering department on designing and setting up the experimental apparatus - Garrett Naughton, Louis Miller, and Benjamin Eichholz. At the same time, I would like to thank all the staff members at Mechanical Engineering Department for their kind help during these years at NDSU.

My deepest sincere appreciation to my dearest parents and my dearest boyfriend Kun, who always are my mental support and love me without any hesitation wherever and whenever. With their love, I have been able to go through every difficult moment in my lifetime. I really want to memorize my grandpa and grandma who passed away during my Ph.D. period. I didn't have much time to accompany them when they were alive. I felt sorry for that and hopefully I could be their proud grandchild.

In the end, thank you very much again for the kind, unconditional support and trust to me all the time in my life.

DEDICATION

This dissertation is dedicated to Mr. Ping Zhang and Ms. Guizhen Liu.

TABLE OF CONTENTS

LIST OF TABLES

LIST OF FIGURES

LIST OF ABBREVIATIONS

ACC..... American College of Cardiology

AHA.....American Heart Association

AS..... Aortic stenosis

AS..... Area strain

AV.....Aortic valve

AVA.....Aortic valve area

CAD..... Computer-aided design

CCD..... Charge-coupled device

CFD.....Computational Fluid Dynamic

CO.....Cardiac output

CoA.....Coarctation of the aorta

DAQ.....Data acquisition system

DMA..... Dynamical mechanical analysis

EOA..... Effective orifice area

FSI.....Fluid-structure interaction

GOA.....Geometric orifice area

HR.....Heart rate

LA..... Left atrium

LCOS..... Low cardiac output syndrome

LV..... Left ventricle

MV..... Mitral valve

MRI.....Magnetic Resonance Imaging

PC.....Polystyrene

PIV..... Particle Image Velocimetry

PMMA..... Polymethylmethacrylate

POM.....Polyformaldehyde

PC.....Polycarbonate

PS..... Polystyrene

RA.....Right atrium

RBC..... Red blood cell

RI.....Refractive index

RSS..... Reynolds shear stress

RV.....Right ventricle

SST.....Shear stress transport

TAVR.....Transcatheter aortic valve replacement

TKE.....Turbulent kinetic energy

TV..... Tricuspid valve

WSS..... Wall shear stress

LIST OF SYMBOLS

λ	Wavelength
Δt	Very short of time
Re	Reynolds number
$W_{o/\alpha}$	Womersley number
L	Length of the orifice in the investigated two-dimensional plane
S/D	Systole-to-diastole
N_{mix}	Refractive index of the mixture
N	Refractive index of refraction of each pure liquid
Φ	Component volume fraction of the mixture of each pure liquid
ρ	Density of each pure liquid
p	Component weight fraction of the mixture of each pure liquid
V_{sedim}	Sedimentation velocity
ρ_p	Porosity of particle
ρ_f	Porosity of fluid
d_p	Diameter of the particle
η	Dynamic viscosity of the fluid
μ	Dynamic viscosity
d_a	Diameter of the valve
u_a	Velocity of the maximum jet flow
ω	Angular frequency of the pulsatile flow

d_{max} ..... Maximum diameters during a cardiac cycle for a specific cross-section

d_{min} ..... Minimum diameters during a cardiac cycle for a specific cross-section

$\overline{u'}$ ..... Velocity fluctuations in x dimension

$\overline{v'}$ ..... Velocity fluctuations in y dimension

ω_z ..... Magnitude of the z-vorticity

U_{avg} ..... Reference velocity calculated by averaging the same CO flow with the same cross-sectional area

Ts ..... Systolic ejection period (s)

ΔP_m ..... Mean pressure gradient (mmHg)

Q ..... Cardiac output (mL/min)

HR ..... Heart rate (bpm)

H/W ..... Height-to-width

$\overline{u'^2}$ ..... Root-mean-square of velocity fluctuation components in horizontal direction

$\overline{v'^2}$ ..... Root-mean-square of velocity fluctuation components in vertical direction

De ..... Dean number

R_C ..... Radius of curvature

d ..... Diameter of the tube

Ω ..... Vorticity tensor

S ..... Rate of strain tensor

1. GENERAL INTRODUCTION

1.1. Aims and Scope

Aortic diseases related to aortic valve and arch lead to significant mortality all over the world. As one of the major risk factors, aortic hemodynamics is generally complex and attracts a growing number of interdisciplinary studies over the past decades. As the major diagnostic tool, clinical imaging has its own limitations in terms of spatial and temporal resolutions and limited controlled over flow conditions. Recent years, computational fluid dynamics (CFD) and advanced optical flow diagnostics based on in vitro mock flow loops have emerged as an efficient and powerful method to help understand the fluid dynamics related to the aortic disease. In particular, particle image velocimetry (PIV) method could provide detailed quantitative flow field data and is valuable for both clinical references and computational simulation validations under various physiological conditions.

The main goal of this Ph.D. dissertation research is to design and construct an in-vivo cardiovascular flow simulator for PIV hemodynamics research and to understand the pulsatile flow characteristics of human aortic valve and aortic arch under normal and diseased conditions, such as aortic stenosis and aortic arch deformations. The overall structure and main contents of this thesis, as shown in Figure 1.1, are summarized as follows:

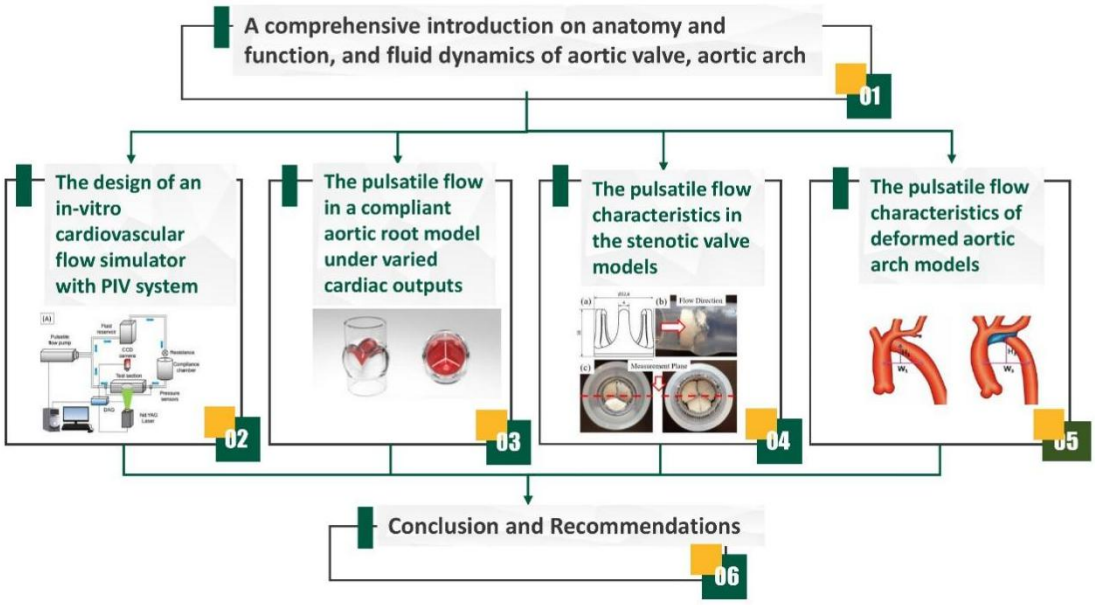

Figure 1.1. Roadmap of this thesis.

In Chapter 1, a comprehensive introduction to physiology and literature review on fluid mechanics of aortic valve and aortic arch are presented based on previous academic and clinical research.

In Chapter 2, the optimization and design of an in-vitro cardiovascular flow simulator with PIV system for this research are introduced and described.

In Chapter 3, we present a paper "An Experimental Study of Pulsatile Flow in a Compliant Aortic Root Model under Varied Cardiac Outputs", published in Fluids. The objective is to study the pulsatile flow characteristics and structural responses in a compliant aortic root model under varied cardiac outputs was investigated using PIV method.

In Chapter 4, we present a paper "Effects of Heart Rate On the Pulsatile Flow Characteristics of a Stenotic Aortic Valve Model: An in Vitro Experimental Study", published in Journal of Fluids Eng. and a paper "Experimental Analysis of Pulsatile Flow Characteristics in Prosthetic Aortic Valve Models with Stenosis", published in Medical Engineering and Physics, respectively. The objective is to study the flow characteristics in the stenotic aortic valve models

under pulsatile conditions generated by a closed-loop cardiovascular flow simulator using Phase-locked PIV method.

In Chapter 5, we present a manuscript "Experimental and Numerical Study of Pulsatile Flow Characteristics in Romanesque and Gothic Aortic Arch Models", submitted to Medical Engineering & Physics for review. The objective of this study is to investigate the pulsatile flow characteristics of the deformed aortic arches - Romanesque and Gothic aortic arch models and compared under pulsatile employing 2D and Tomographic PIV method. Computational Fluid Dynamic (CFD) method was used to verify the consistence with the PIV experimental results.

In Chapter 6, the research findings were summarized and the limitations associated with the directions for future research were also discussed in the end.

1.2. Heart

1.2.1. Anatomy and Function of Heart

It is known that the human heart plays a vital role in the blood circulation of the whole body. As a hollow muscular organ, heart is divided into right and left sides via partition septum and each side of heart has two chambers, i.e. four heart chambers, named as right atrium (RA), left atrium (LA), right ventricle (RV) and left ventricle (LV), respectively. Under normal conditions, there are four valves that connect the chambers working as the check valves to maintain the one-directional blood flow. These heart valves between the atria and the ventricles are called atrioventricular valves including tricuspid valve (TV) and mitral valve (MV). The TV is located between the right atrium and the right ventricle, while the MV is situated between the left atrium and the left ventricle. The remaining two heart valves are called semilunar valves – aortic valve (AV) and pulmonary valve (PV). The AV is located between the aorta and the LV

while the PV is situated between the pulmonary artery and the RV. The basic structure of heart and its key portions are shown in Figure 1.2.

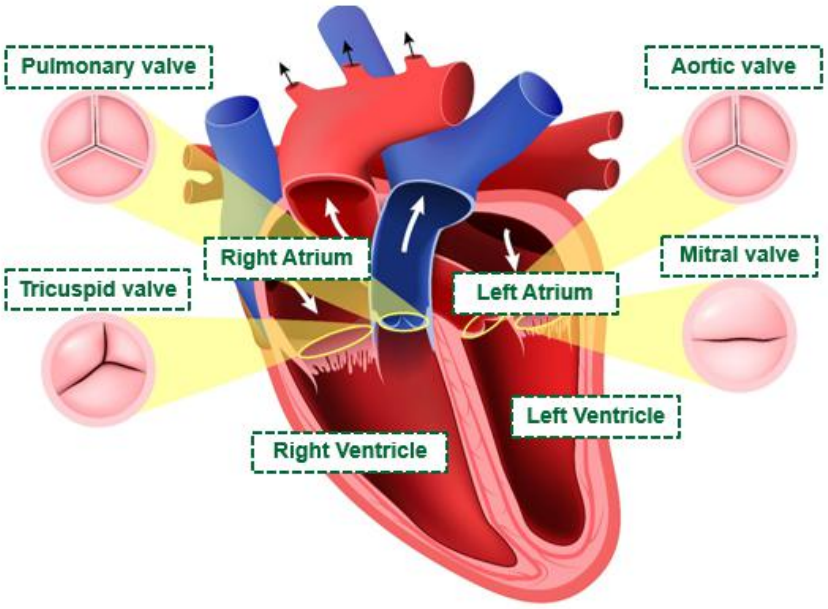

Figure 1.2. Schematics of the human heart and heart valves [1].

Heart works as an engine to pump blood through the entire body via two important circulations of body - pulmonary circulation and systemic circulation [2]. The right heart actually controls the pulmonary circulation. In this circulation, the deoxygenated blood returns to the vena cava and then transports into the RA of the right heart. The deoxygenated blood moves into the RV via the TV. After that, the deoxygenated blood in the RV pumps into the pulmonary arteries through the PV and moves to the lungs where Carbon dioxide and oxygen exchanging procedure occur. In the meantime, the left heart drives the systemic circulation. After being oxygenated in the lungs, the oxygenated blood from the pulmonary veins moves into the LA of the left heart. The oxygenated blood then pumps into the LV through the MV and then ejects from the LV through the AV to the aorta. Then the oxygen-enriched blood transports to all the organs and tissues of human body. After releasing the oxygen to organs and tissues, the deoxygenated blood travels back through vena cava again to the RA of the right heart [2], [3].

The whole process repeats and almost happens at the same time for the right and left heart during one heartbeat.

1.2.2. Cardiac Cycle

A heartbeat is also called a cardiac cycle. Typically, the adults' resting heart rate is between 60 and 90 beats per minute (bpm). During one heartbeat, it can be divided into systole and diastole stages. Figure 1.3 shows the systole and diastole timing with the valve configurations in an example cardiac cycle (0.8s / 75 bpm).

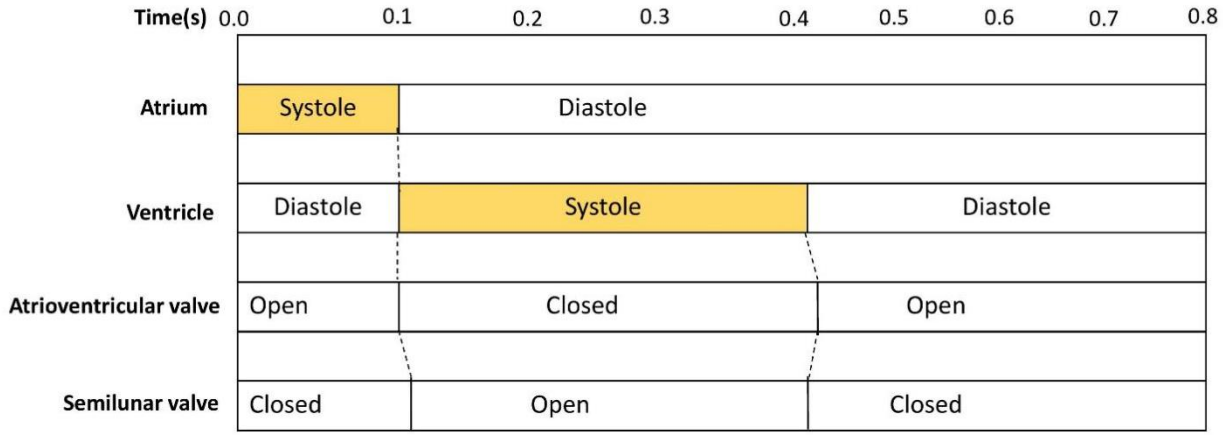

Figure 1.3. Systole and diastole process in one cardiac cycle [4].

Systole is the contraction of the heart muscle. From this figure, it can be seen that the atrial systole normally happens about 0.1s ahead of ventricular systole and then ventricular systole starts and lasts about 0.3s after previous atrial systole. During the atrial systole, the pressure inside the atria increases to push the atrioventricular valves (TV and MV) open. These TV and MV remain open until much higher pressure forms in the ventricles to push them back to close during the ventricular systole.

Diastole is the relaxation of the heart muscle. During the atrial systole, the ventricles experience blood refiling, the process of which is called ventricular diastole. The ventricular systole starts after being filled and the atrioventricular valves closed. In addition, after the

previous ventricular systole, the atria and ventricles are undergoing refilling process that indicate they are both in diastole. Both of the semilunar valves (AV and PV) remain closed. Although the atria and the ventricles both have their own systole and diastole during each heartbeat, the term is normally referred to the ventricular ones when they are mentioned.

A full cardiac cycle can be mainly divided into seven phases [5]. The left heart and 75 bpm (0.8s) are selected as an example. The events and details can be seen in Figure 1.4.

- **Phase 1:** Atrial contraction

Atrial contraction is the starting point of the whole cardiac cycle. At fisrt, all four chambers are relaxed. When the atria starts to contract, the inside pressure goes up, pumping the blood flow into the LV quickly. This process lasts about 0.1s during the whole cardiac cycle. At the end of this phase, the blood volume in the LV is called end-diastolic volume (EDV).

- **Phase 2:** Isovolumetric contraction

Phase 2 is defined as isovolumetric contraction which represents the ventricular systole. After atrial contraction, the ventricles start to contract,and then the pressure inside the LV increases quickly. The MV is forced to close when the pressure inside the LV becomes larger than that in the LA. At this point, the LV is a fully closed chamber with the inside pressure increasing. It still experiences contraction but no volume changes in the chamber.

- **Phase 3 - 4:** Ejection

Phase 3 – Rapid blood ejection: The AV is forced to open at this phase when the LV pressure exceeds the aortic pressure. The blood flow starts to pump into the aorta very quickly. The pressure gradient between the LV and the aorta is very small at this moment.

Phase 4: Reduced blood ejection: The LV pressure decrease due to the relaxation of the muscle. When the LV pressure becomes a little lower than the aortic pressure, the blood flow

keeps moving into the aorta due to inertial force. In the end, the LV pressure drops quicker and the aortic valve closes to prevent the blood back flow to the LV. The volume of blood flow in the LV now is called the end-systolic volume (ESV). So the stroke volume (SV) that means the ejected blood volume during the ventricular systole: SV = EDV – ESV.

- **Phase 5:** Isovolumetric relaxation

Phase 5 is isovolumetric relaxation. After blood ejection (aortic valve close), the LV remains relaxed and the pressure inside keeps decreasing. All the valves close at this point and the blood volume in the LV is constant. Then the ventricular diastole starts.

- **Phase 6 – 7:** Rapid inflow and diastasis (refilling)

Phase 6: Rapid inflow: the MV opens quickly when the LA pressure exceeds the LV pressure. The accumulated blood in the LA drops into the LV. After that, the LV continues to relax causing more blood in the LA flow into the LA.

Phase 7: Diastasis which is also called reduced inflow. In this process, the LV keeps filling and the LV pressure starts to rise, which shortens the pressure difference between the LV and LA.

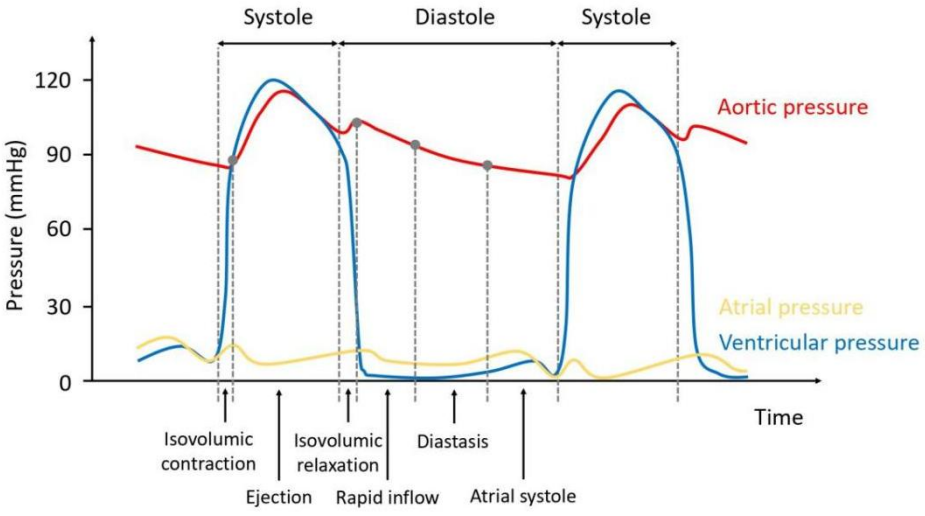

Figure 1.4. Events and details in one cardiac cycle.

1.3. Aortic Valve

1.3.1. Anatomy and Function of Aortic Valve

All four valves of heart play a very significant role in blood flow regulation to prevent the reversed flow. Among them, the aortic valve is in the most important position in maintaining efficient cardiac function especially for the systemic circulation. The AV locates at the junction of the LV and the aorta (the largest artery of human body). Because LV pumping power is the strongest among the four chambers, the AV sustains the highest blood pressure compared with the other three valves.

A normal AV (diameter ≈ 25 mm) has three thin semilunar cusps or leaflets (thickness ≈ 1.5 mm) within a connective tissue sleeve [6]. The three cusps are the left posterior (left coronary cusp), anterior (right coronary cusp) and right posterior (non-coronary cusp), respectively [6]. Each leaflet has three different layers, which is called fibrosa, spongiosa and ventricularis, respectively [7]. The side of the valve facing the aorta is the fibrosa, which the opposite side is the ventricularis that is made of collagen and elastin. Meanwhile, the ventricularis is thinner and smooth layer than the fibrosa. The mid-layer of the valve is the spongiosa that is composed of connective tissue and proteins [5]. When the AV is closed, the three leaflets will form a small overlapping surface (coaption surface) to make the valve sealed better. The fibrous annular ring is attached to the LV that is the inlet of the LV outflow tract. There are three bulges at the aortic root (structural support for leaflets) that are superior to the annular ring of the AV, which are called aortic sinus or sinus of Valsalva. The junction between the sinuses and the aorta is named the sinotubular junction (the outlet of the aortic root into the ascending aorta), while the junction facing the LV is called aortic annulus. Figure 1.5 shows the key components terminologies of AV in latitude and three major sites of aortic valve in longitude direction. The white arrows in

the Figure 1.5 (b) from the left to right indicate the blood flow from the LV to the ascending aorta direction.

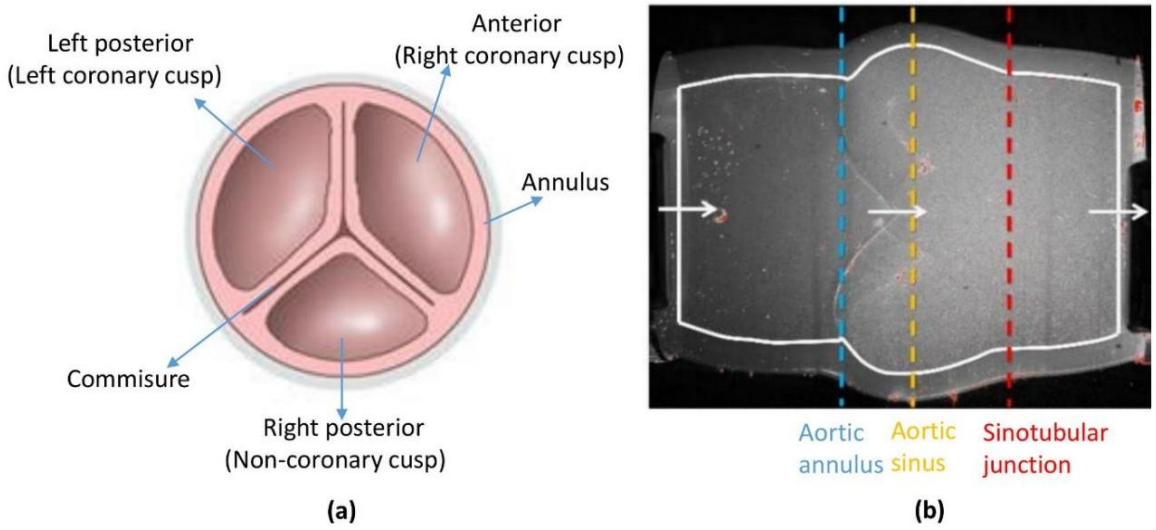

Figure 1.5. (a) Key components terminologies of aortic valve in latitude direction (b) three major sites of aortic valve in longitude direction.

The key function of the AV is acting as the check valve to ensure unidirectional flow, which prevents the blood backflow to the LV from the ascending aorta. When the LV contracts (during the ventricular systole), the pressure increases rapidly in the LV (larger than the pressure in the aorta) to push the AV open and then the high velocity and pressure blood flow pumps out from the LV via AV to the ascending aorta [8]. Thus, the inappropriate opening and closing of the AV may result in the abnormal flow velocity and pressure compared with the normal condition. Given its significant physiological function, a variety of aortic diseases can result from the dysfunction of the AV, including but not limited to aortic calcification, stenosis and regurgitation. Severe conditions could lead to heart failure or sudden death [9].

1.3.2. Aortic Valve Diseases

In the United States, approximately five million people are affected by the valvular heart diseases every year. According to the studies, the AV diseases are dominant and the most

prevalent of them are valvular stenosis and regurgitation [10]. Meanwhile, they are also considered to be the crucial predisposing causes for many cardiovascular diseases which include but not limited to aortic aneurysm, thromboembolism, and stroke [11], [12].

- **Aortic valve regurgitation:**

aortic valve regurgitation is the phenomenon that the blood flow reverses to the LV from the ascending aorta during ventricular diastole. This regurgitation may be given rise to the valve dysfunction or leak. This may be caused by many reasons such as aging processes and bacterial infection, etc. Therefore, the heart will work harder to compensate for the blood leakage to meet the body's need, which means that this abnormal blood flow condition can progressively lead to the volume and pressure overload of the heart and ultimately result in other cardiovascular complications or even heart failure.

- **Aortic valve stenosis:**

Aortic stenosis (AS) usually occurs when the leaflets of AV become stiff, which can lead to a narrowed valve orifice area. This valvular abnormality will result in an increased pressure gradient between the LV and the aorta. Different from the other AV diseases, AS is a progressive disease that can lead to a very high risk of mortality if untreated and usually asymptomatic before midterm stage, which means that AS is relatively difficult to be detected at its early stage (mild and moderate) [13]. In addition, AS is also the third prevalent cardiovascular disease except hypertension and coronary heart disease in the Western countries [14]. Therefore, AS has emerged as a study target for many researchers in recent decades.

Nowadays, the treatments of aortic valve regurgitation and stenosis are normally through surgical procedures such as valve repair and replacement.

1.3.3. Aortic Valve Repair and Artificial Valves

Aortic valve (AV) repair surgery is normally the first option due to its advantages such as lower infection risk and long-tern meditation, etc. AV repair is also called AV reconstruction, which is usually the traditional open-heart surgery to reconstruct the form and function of a diseased valve in order to enhance the blood flow. There are several kinds of surgical methods for the AV repair treatment frequently.

- **Commissurotomy:** Replace a wide valve cusp
- **Vavuloplasty:** Open a stenotic (stiff) valve using a balloon
- **Annuloplasty:** Reinforce the ring around annulus through inserting an artificial ring
- **Decalcification:** Eliminate the calcium from leaflets or annulus to stop blockage
- **Reshaping:** Reshape the tissue to make it open and close correctly
- **Patching:** Conceal or fix holes of valve by inserting tissue to prevent leakage
- **Repair of Chordae tendineae:** Fix or reshape the structural support of the valve

The AV repair approaches summarized above are selected depending on the realistic patients' health conditions. Specially, the repair of AV stenosis only can be treated through commissurotomy and decalcification [15].

When the patients have the severe aortic valve problems that cannot be treated through surgical repair, aortic valve (AV) replacements are often recommended with an artificial valve. Nowadays, there are basically two types of artificial replacement valves that dominate the current clinical market commercially, i.e. mechanical and bio-prosthetic valves.

- **Mechanical valves:**

Mechanical valves are the most traditional and widely-used valvular prosthesis in valve replacement surgery due to its long-term technical improvement, good durability (low risk of

valve deterioration), high level of commercialization and, as a result, relatively lower price [16]. However, because of its non-physiological structure and interactions, it may lead to abnormal hemodynamics which could result in the increasing risks of platelet activation and even hemolysis [17]-[19]. Therefore, patients who received mechanical valve implantation are often needed to take the anticoagulant medicines in the rest of their life. In the opposite, the use of bio-prosthetic valves has significantly increased in the last decades [20].

- **Bio-prosthetic valves:**

Compared with traditional mechanical valves, bio-prosthetic valves are relatively newly-invented valve type but quickly attracted a great number of clinical and academic attentions. The bio-prosthetic valves are normally made of porcine or bovine tissues with the native valve structures - three leaflets [21]. Because the anatomy and materials of bio-prosthetic valves are more similar to the native valves, the risks of thrombosis and hemolysis are relatively low compared with the mechanical valves [22]. However, the tissue-based bio-prosthetic valves are more prone to tissue failure due to its deteriorated materials [23]. This often result in its shorter durability than the traditional mechanical valves [24].

- **Polymeric valves:**

Polymeric valves, similar as mechanical valves, has emerged as another artificial valve prostheses alternative. It was a flexible polyurethane (PU) mitral valve that firstly implanted into humans [25], [26]. During that time, polymeric materials like silicone, Polytetrafluoroethylene (PTFE), Polyethylene terephthalate (PETE or Dacron) and Teflon were all possible choices due to great flexibility and biocompatibility. However, even with different designs, polymeric valves made in those materials had a lot of shortcomings, which, as a result, greatly limited its application. For instance, they are normally of lower durability due to rapid hydrolysis and low

resistance to thromboembolism, which made them unsuitable choices for fabricating valve prostheses [27], [28]. In the past 20-30 years, more superior polymers have been developed, which were more durable, bio-stable, and can better reproduce the real hemodynamics of natural valves.

Overall, a further understanding of valve hemodynamics is of significant importance to enhance the clinical assessment, deployment, and management of valve prostheses. Therefore, recently, numerous studies have been performed in attempts to quantify the fundamental hemodynamics and fluid-structure interactions of artificial heart valves using various computational and experimental methods.

1.4. Aorta

1.4.1. Anatomy and Function of Aorta

Aorta is the largest artery of the human body, which connects the heart (LV), ascending aorta, aortic arch, descending aorta and down to the abdominal aorta together (deriving from the LV of heart to the abdomen). Aorta carries the oxygenated blood flow from the LV to the systemic system of the body [29]. Generally, human aorta is an about 1-foot long in length and over 1-inch wide in diameter tube, which contains ascending aorta (normal diameter < 2.1 cm/m^2), descending aorta (normal diameter < 1.6 cm/m^2), thoracic aorta and then abdominal aorta (normal diameter < 3 cm) along the tube and three small branches (brachiocephalic artery, left common carotid artery and left subclavian artery) on the top of aortic arch (proximal to distal) [30]. This indicates that the aorta is the widest at the junction between the LV and the ascending aorta and becomes gradually narrower when it extends to the distal abdomen. The aorta basically consists of three layers including tunica intima (inner layer with a smooth surface), tunica media (middle layer made of smooth muscle, elastic tissue, and collagen) and tunica adventitia (outer

layer made of connective tissue), the wall of which has a very high elastic compliance (normal wall thickness < 4 mm, Young's modulus ≈ 3-6 $N/m^2 \cdot 10^5$) [31], [32]. Figure 1.6 below shows the terminologies of each important part of the human aorta in detail.

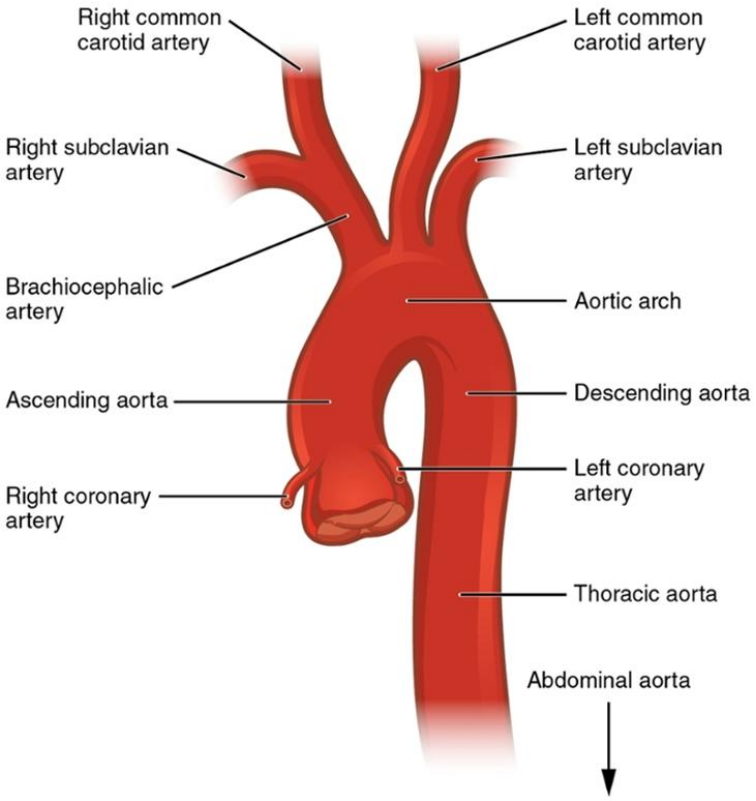

Figure 1.6. Schematic of human aorta with labeled terminologies of key segments [33].

In the cardiovascular system, fully turbulent flow is not common as most of the blood flow in human arterial and venous systems is normally laminar (Re < 30). However, turbulent flow condition at a high flow velocity can be observed in the human aorta (especially the descending aorta) [5]. In in vitro experiments, two non-dimensional parameters, i.e., the Womersley number and Reynolds number, are normally used to describe the periodicity and the dynamic similarity of physiological pulsatile flow. Generally speaking, the blood ejects from the LV to the aorta with a very high pressure and high velocity. This high pulsatile (high Womersley number around 13.83, normal artery ≈ 2.21) and turbulent blood flow (peak Re number ≈ 4500

indicates a high instability of blood flow passing through the aorta [34]. The aorta experiences this continuous type of shock and high working load through this repeated cardiac cycle. Furthermore, the aorta has a curved arch structure connecting the ascending aorta, descending aorta and the branched arteries towards head and neck. Due to the complex structure, the aortic flow tends to be more complicated and three-dimensional. The hemodynamics of the aortic arch and its relation to the potential diseases are still not fully understood and required a systematic study.

1.4.2. Aortic Arch Diseases

Due to the complex structure and hemodynamics of the aorta, the dysfunctional aortic arch can lead to the many fatal aortic arch diseases. Several common aortic arch diseases include aortic aneurysm, aortic dissection, and coarctation of aorta. Aortic aneurysm is the abnormal bulge of the aorta and the diameter of its injured part is normally 1.5 times larger than normal condition [35]. When the aortic aneurysm gradually forms, it can weaken the blood vessel wall and raise the possibility of rupture. Aortic dissection is a fatal condition which occurs when the blood flow into the layers through the injured inner layer (tunica intima). Aortic dissection can happen at any point of the aorta [36]. Aortic dissection will result in death very quickly due to insufficient heart blood supply or the complete aortic rupture [37]. Aortic dissection is actually a rare disease, which has an occurrence rate around 3/100000 people every year [38].

Coarctation of the aorta (CoA) is the narrowing of the aorta and occurs around the aortic arch portion, leading to altered hemodynamics in the aorta as well as a rising working load for heart. Different from other aortic arch abnormalities, CoA is a congenital defect which often occurs at birth and nearly occupies 6-8 % of the congenital heart diseases currently [39], [40]. Surgery is often necessary to remove the narrowed section of the aorta, however, even if the

patients received successful treatments, many young patients still develop cardiovascular related complications due to its complicated structure, particularly systematic hypertension (20-40 % young adult survivors) later in their adulthoods [39], [41], [42]. Recently, the reasons behind this complication have been investigated and one of the suggested causes has been proposed to be the deformation of aortic arch after successful surgeries due to the induced irregular hemodynamics [43]-[45].

The pathologies behind aortic arch diseases are usually varied and many of them are asymptomatic and life-threatening. The complicated hemodynamics increases the difficulty of diagnosis and always pose enormous challenges for the patients' treatments especially surgeries in the realistic life.

1.4.3. CoA Treatment and Deformed Aortic Arch

Catheterization or surgical removal are clinical options to treat the coarctation of the aorta. The catheterization is actually angioplasty method with or without stent. During this procedure, a long and thin catheter attached with a balloon at the end would be transported to the aorta through leg artery. As the thin catheter arrives the destination (coarctation), the balloon is inflated to enlarge the narrowed part. When the coarctation is corrected, the catheter and balloon will be removed. For the severe coarctation patient, a stent (a small mesh tube) will be inserted into the narrowed area to keep it open normally. The open surgery is another way to treat this defect. Normally, when the coarctation of the patient is small, the end-to-end anastomosis surgical method will be recommended to remove the small narrowed area. In addition, various kinds of bypass graft surgery are the other surgical alternatives for the patients. Even if the patient survives from the successful surgery, the medication care and the regular medical tests are still necessary to follow up the recovery.

However, according to researches, even if many young patients repair it successfully, they still have a large chance to develop other cardiovascular complications such as systematic hypertension (20-40 % young adult survivors) later in their adulthoods [41], [42], [46]. There are two mainly types of the deformed arch - Gothic and Romanesque based on statistics. Both of them are named based on the geometric structure of the architecture. While the Romanesque arch is close to a normal aortic arch with a round and smooth arch section, a Gothic arch is characterized by a triangular shape and an increased overall height/width ratio. Due to the induced irregular hemodynamics, the reasons behind this kind of complication have been widely investigated and one of the suggested causes has been confirmed to be the deformation of the aortic arch after successful surgeries [43]-[45].

1.5. Blood Flow

The blood flow problems was first studied by Young and Poiseuille [47]. Blood mainly consists of the blood plasma with the blood cells suspended. The blood plasma makes up approximately 55% of the overall blood volume, which is made of about 93% water, 6-8% proteins and 1.5% other solutes but it may vary [48]. The density of the plasma is about 1030 kg/m^3 and the normal plasma itself behaves as a Newtonian flow having a dynamic viscosity of 1.4×10^{-3} Pa·s under the normal body temperature [49]. There are mainly three types of blood cells: the white blood cells (leukocytes), the red blood cells (erythrocytes) and the platelets. The red blood cells take up around 45% of the blood volume, the shape of which is biconcave discoid with a diameter around 7 μm. This special shape of the red blood cells make them easier to squeeze and transport to small size capillaries [50]. Although the amount of the white blood cells and the platelets are small compared with the red blood cells, they play a very significant function in our immune system and blood clotting.

Since there are small numbers of the white blood cells and the platelets inside the blood, the rheology of blood is mainly impacted by the red blood cells. Thus, blood is known as a non-Newtonian fluid. However, the non-Newtonian effect is small and really depends. When the blood transports through small vessels (the red blood cells squeeze), it behaves like a non-Newtonian fluid. However, in the large vessels such as aorta, the non-Newtonian effect is really weak, so the blood can be approximately treated as a Newtonian fluid with a dynamic viscosity of 3.5×10^{-3} kg/(m·s) [47]. The most of blood flow inside the vessels are laminar, however, the blood flow in the arteries is highly pulsatile.

1.6. Fluid Dynamics Research

The relationship between hemodynamics and the pathology of aortic valve, aortic arch and related diseases underscores the need to further understand aortic fluid dynamics. In recent years, Hemodynamics related to aorta has been investigated by researchers employing multiple approaches such as computational fluid dynamics (CFD) and Particle Image Velocimetry (PIV), etc.

1.6.1. CFD Research Related to Aortic Valve Hemodynamics

Over the years, CFD simulation has evolved into a powerful technique to help understand the complicated physiological flows, and it also has been widely utilized to investigate the hemodynamics including instability, vorticity and fluid-structure interactions of artificial valves under various conditions.

Ge et al. [51] investigated the steady-state flow passing through a fully open mechanical valve with the help of CFD simulations. Shim and Chang [52] investigated a mechanical valve under steady flow conditions using three-dimensional modeling and found out the absence of the vortical flow downstream. Furthermore, through direct numerical simulation, Dasi et al. [53]

further revealed that the complicated vortical flow characteristics under the pulsatile flow conditions and its associated flow characteristics of a rigid bi-leaflet mechanical heart valve downstream. More recently, researches have attempts to study the relationships between the hemodynamic features and the leaflets motions with the assistance of CFD simulations. For example, Shi et al. [54] analyzed the pulsatile flow through bi-leaflet mechanical valves when they are in the opening condition using moving boundary to simulate the moving leaflets features via CFD method to figure out the impact of blood-leaflet interaction. In addition, Kelly et al. [55] predicted the 3D and time-dependent flow through a bi-leaflet mechanical valve via establishing the accurate CFD model and found out the small-scale flow around the pivot regions. Yun et al. [56] simulated the motion of platelets to detect the possibility of blood damage through fluid-structure interaction within the hinge recess of a bi-leaflet mechanical heart valve.

To date, the compliant artificial aortic valves, such as tissue-based bio-prosthetic valves have similar leaflets structures with native valves and, thus, could have better hemodynamics than mechanical valves. However, the bio-prosthetic valves still have the obvious shortcomings. For example, the characteristics of the bio-prosthetic valve make it easier to generate high pressure gradient than mechanical valves, so this feature increases the risks to acquire the stenosis and shortens its lifetime [21]. Hence, due to its durability and tissue rupture issues, the bio-prosthetic valves under simulated physiological conditions has also drawn great attention and its fluid dynamics have been widely investigated in recent years [57]-[61].

Bio-prosthetic valves have the flexible leaflet structure as the native valves and the computational simulation play a very significant role in accessing the performance of the valve structures and hemodynamics of bio-prosthetic valves. However, the primary shortcoming of this type of valve is the short durability. Thus, the computational analysis can provide insights into

the manufacturing processes and also contribute to improve the design of valves. Numerical analysis has attempts to detect the mechanical failure of bio-prosthetic valve, Krucinski et al. [62] simulated the leaflet open and closure of a tri-leaflet bio-prosthetic valve fabricated with bovine pericardial tissue using non-linear finite element and commercial finite element methods together and their results exhibited that the high flexural and compressive stresses occurs near the vicinity of sharp leaflet curvatures. Meanwhile, fluid-structure interaction (FSI) simulation is a common research direction to evaluate the hemodynamics of bio-prosthetic valves. Due to the flexible movement of the valve leaflets, Kamensky et al. [63] analyzed a three cusps bio-prosthetic valve during the entire cardiac cycle employing computational FSI method with immerse geometric analysis. Hsu et al. [64] further evaluated a bio-prosthetic valve inserted in the flexible artery using FSI simulation with various immersed-boundary and arbitrary Lagrangian–Eulerian methods. Furthermore, Makhijani et al. [65] combined the three-dimensional model with fluid-structure model to simulate a bio-prosthetic valve under various flow conditions such as pulsatile and laminar. Their simulation results around the valve orifice area agree well with the previous experimental data.

1.6.2. Experimental Fluid Dynamics Research Related to Aortic Valve Hemodynamics

In vitro experimental studies could greatly improve the understanding of artificial valve hemodynamics due to the controllable flow conditions and the enhanced spatial and temporal resolutions compared with the traditional clinical method [66]. PIV technique has emerged as a powerful visualization tool to utilize for in vitro studies of artificial valves.

Lim et al. [67] studied the fluid dynamics in four different prosthetic valves including mechanical valves under steady flow conditions employing PIV technique. Balducci et al. [68] investigated the downstream flow fields of a bi-leaflet mechanical valve using PIV and PTV

measurements. The results showed highly unsteady flow status and the presence of large-scale vortices in the two areas - aortic sinus and leaflet wakes, which came up with the similar results with the simulation studies [52], [53]. Bellofiore and Quinlan [69] conducted PIV experiments on flow passing through a mechanical valve with substantially enhanced spatial and temporal resolutions. This led to a better understanding of a Lagrangian analysis of blood cell trajectories and the platelet activation at different stages of the cardiac cycle. Li et al. [19] performed the PIV experiments to estimate the Reynolds stresses and the viscous dissipative stresses of a mechanical valve, which indicated that the valve-induced viscous stresses could possibly lead to platelet rupture. Apart from general flow characteristics, researchers have been able to investigate other flow indicators, e.g., energy loss, through various in vitro experimental studies to evaluate aortic stenosis associated with the performance of mechanical valves [70]-[72].

PIV method has also been used to investigate the hemodynamics of bio-prosthetic valves [23], [73]-[75]. Avelar et al. [76] employed PIV method to detect the leaflet flutter conditions and differences of two bio-prosthetic valves with various materials. Lim et al. [67] investigated the flow behaviors of four different prosthetic valves including a porcine bio-prosthetic valve and three different mechanical valves under the steady conditions using PIV technique and noticed that the porcine valve showed the highest pressure loss and Reynolds stresses in the experiments. In addition, Lim et al. [77] conducted the pulsatile flow PIV measurements to further investigate the velocity fields and Reynolds stresses downstream of a porcine bio-prosthetic valve during systole to make the estimation of the shear-induced damage. Saikrishnan et al. [78] also performed in vitro PIV experiments of a porcine tissue valve and the results showed that the turbulent kinetic energy (TKE) and vorticity of the flow downstream of the valve were significantly increased. Three-dimensional flow fields conditions of a bio-prosthetic

valve have been analyzed through Tomographic PIV technique by Toninato et al. The bio-prosthetic valve was inserted into different size aortic roots and their results exhibited that the aortic jet diameter can impact the characteristics of the flow fields [79]. A combination of doppler echocardiography and flow visualization imaging method is also another in vitro experimental approach to access the hemodynamics performances of a bio-prosthetic aortic valve [80].

Polymeric valves that have a similar structure as the natural valves have emerged as another artificial valve prostheses alternative. For instance, Haj-Ali et al. [60] predicted the kinematics and the structural behavior of the polymeric tri-leaflet aortic valves through nonlinear structural simulations and compared the simulation results to the experimental data to provide a benchmark for future artificial valve designs. Leo et al. [23] examined the velocity and Reynolds shear stress (RSS) downstream of tri-leaflet polymeric heart valves with PIV technique.

1.6.3. Hemodynamics Research of Aortic Arch

Multiple methods have been utilized to elucidate the hemodynamics of aortic arch for further understanding the pathologies behind the aortic arch diseases. Clinical imaging tools such as magnetic resonance imaging (MRI) is widely used to help doctors study and diagnosis the patients. Computational approaches are very powerful commonly employed to reveal the hemodynamics of aortic arch and clinical validation, thus many computational studies have been widely utilized by researchers to assess the flow fields of aortic arch and discuss the relations between the hemodynamic characteristics and aortic abnormalities [81].

Wall shear stress (WSS) and the secondary flow are usually treated as critical factors in the progression of the atherosclerotic lesions. Efstathopoulos et al. [82] analyzed the correlation between WSS in the ascending aorta and three different Poiseuille based flow conditions during

a full cardiac cycle through studying 20 non-atherosclerotic patient-specific MRI data and they found that this type of research method is feasible and helpful. Employing the MRI to acquire patient-specific data, Kliner et al. [83] revealed the relation between the retrograde secondary flow with the atherosclerotic formation due to the curvature of aortic arch. Through the direct computational method, Shahcheraghi et al. [84] simulated a human aortic arch through three-dimensional reconstruction and analyzed the flow fields of aortic arch under pulsatile condition. Their results showed that the primary and secondary flow were observed along aortic arch associated with high WSS along the outer wall near the branches and low along the inner wall that may lead to the development of early atherosclerotic lesions. Fujioka et al. [85] also studied the flow patterns of the realistic aortic arch model through the computational analysis, and they observed that the secondary flow near the inner wall which can induce the large WSS variation. Meanwhile, with the assist of MRI , the CFD results of aortic arch hemodynamics were validated by Miyazake et al. and agreed well. They observed the secondary flow in the distal aortic arch and WSS distribution [86]. The impact of different inlet boundary conditions on aortic arch hemodynamics also have been studied through computational methods with the help of MRI by several authors [87], [88]. Among them, Jin et al. [89] employed MRI dataset to build a computational model to study the effects of wall motion on the flow patterns around the ascending aorta.

Studies of aortic arch hemodynamics have also been conducted and studied for diseased aortic arch. For instance, the patients suffer aortic aneurysm or congenital aortic arch defect. Hardman et al. [90] utilized the various patient-specify inlet boundary dataset generated from MRI combined with the CFD method to analyze their impact on aortic aneurysm hemodynamics. Based on FSI modeling, Yeh et al. [91] simulated three ascending thoracic aortic aneurysms with

different diameters according to patient–specific data under different blood pressure. They observed that the aneurysm geometry and blood pressure have significant impact on the WSS. Shang et al. [92] evaluated the peak WSS for various thoracic aortic aneurysm models with different diameters through computational methods and they found that the growth rate of aneurysm was highly related to peak WSS that is an important predictor for treatments. For the most common congenital defect – CoA, the hemodynamics of the deformed aortic arch after surgery of coarctation have drawn much attention due to its debates of hypertension in recent years. Based on MRI study, Frydrychowicz et al. [93] suggested that in the altered shapes aortic arches, secondary flow characteristics such as helix and vortex flow were less common. Szopos et al. [94] studied the hemodynamics of idealized Gothic and Romanesque aortic arch employing CFD and FSI methods together and the results indicated that a Gothic arch resulted in an eccentric and higher wall shear stress (WSS) on the ascending and horizontal aortic segments. Olivieri et al. [95] also conducted a steady flow CFD simulation of three different deformed aortic arch geometries. Their results showed that Gothic arch has a unique location of peak WSS in the descending aorta compared with that in Romanesque and Crenel arches.

Overall, these findings imply the complex hemodynamic mechanisms and highlight the needs for detailed fluid dynamic studies of aortic arch hemodynamics. However, common clinical imaging has limited spatial and temporal resolutions, which is also limited to specific boundary conditions. Most of the previous CFD studies were concentrated on steady flow conditions in idealized geometries. Currently, there is a lack of experimental data of aortic arch hemodynamics, which is important for direct validation of particular flow phenomena. Therefore, in recent years, many researchers have used in vitro PIV experimentation as an important

approach to assist the in vitro hemodynamic studies associated with biomedical researches [75], [96], [97].

1.7. Motivation of Current Studies

Overall, based on the previous literature reviews and researches, there are several research gaps in the field of aortic hemodynamics, as summarized below:

1) The resolution of clinical imaging is very limited so that the detailed and time-dependent data are not easy to obtain. Also CFD studies need experimental data to validate. In vitro flow loop that simulates pulsatile flow waveforms provides a controllable method to research effects of different conditions. PIV measurements could provide detailed quantitative flow data that is valuable for both physiological understanding and computational simulation validations.

2) For the most of the above-mentioned aortic valve research that addressed the hemodynamics of the artificial aortic valves, the stented replacement valve models were mostly placed into simplified or rigid straight tube models. The geometric complexity and compliance of the aortic root and the valve leaflets were seldom considered. In addition, the influence of reduced flow rate or cardiac output (CO) on the aortic hemodynamics, which is often linked to the LV systolic and diastolic dysfunctions [98], has not been fully investigated.

3) Stenotic aortic valve is a very significant valvular disease which happens progressively. However, it is not easy to capture the flow field characteristics via clinical methods in vivo. At the same time, the questions of how the flow characteristics across a stenotic valve would change under varied physiological conditions and how these changes would affect the assessment results of stenosis severity have not yet been extensively studied in previous researches.

4) The key differences in the flow patterns and the relationship with the cardiovascular complications between these two types of deformed arches even if after successful surgeries, i.e.,

Gothic and Romanesque arches, have not been comprehensively investigated using experimental methods especially PIV technique.

1.8. The Objectives of Current Studies

To further study those research gaps, the detailed objectives of this thesis are listed in the following parts:

1. To mimic the physiological condition of in vivo pulsatile flow, in-vitro experimental apparatus relied on a mock circulatory loop was built. Along with the experimental setup, a phase-locked PIV system was employed to obtain clear instantaneous images so that the ensemble-average velocity, vorticity, and turbulence were calculated and analyzed for different phases under different conditions.

2. Conduct experimental tests to study the flow field characteristics in a compliant aortic valve root model under varied cardiac outputs using phase-locked PIV technique. In this study, the influence of the cardiac outputs on the hemodynamic and structural responses of the aortic root model was investigated and compared the results to the corresponding clinical studies.

3. Conduct experimental tests to investigate the flow characteristics of stenotic aortic valve models under pulsatile condition generated by a closed-loop cardiovascular flow simulator. Phase-locked PIV method was used to quantify the turbulent flow field information. Pressure gradient waveforms were generated to estimate the severity of the stenosis.

4. Conduct experimental tests to understand the significant differences in the flow patterns between these two typical deformed arches after successful CoA employing planar and tomographic PIV measurements, i.e., Gothic and Romanesque arch models, under typical aortic flow conditions. Conduct numerical simulations to validate the obtained experimental results. The abnormal flow behaviors of the Romanesque and Gothic arches was obtained and discussed.

2. DESIGN OF AN IN-VITRO CARDIOVASCULAR FLOW SIMULATOR FOR PIV RESEARCH

2.1. Design of Mock Circulatory Flow Loop

To simulate the physiological condition of actual aortic pulsatile flow, a mock circulatory closed-loop experimental system was constructed and utilized in this study as illustrated below in Figure 2.1. The design of this type of apparatus was firstly described by Rosenberg et al. [98] and have been reviewed by Deutsch et al. [99]. The details of each component in the mock circulatory system will be described in the following paragraphs.

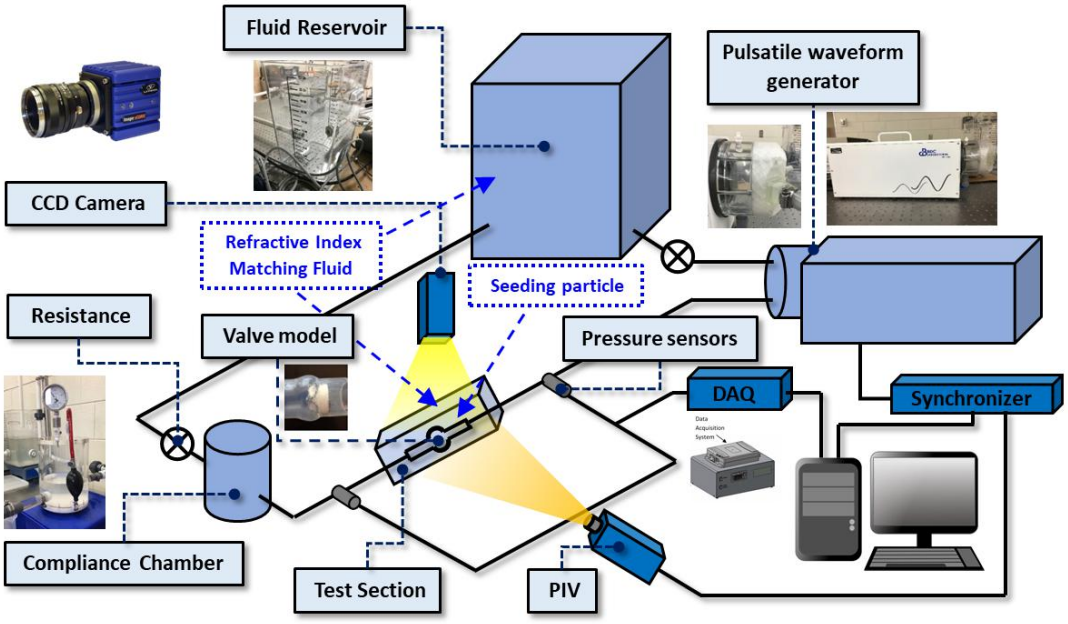

Figure 2.1. Schematic of a mock circulatory loop used for current pulsatile studies.

A programmable pulsatile pump (PD-1100, BDC Laboratories) was utilized to generate user-defined skewed sinusoidal waveform function with a frequency ranging from 2 to 240 beats per minute (bpm) and a stoke volume ranging from 0 to 300 ml. The corresponding flow rates can range from 0 to 10 L/min. A pump head module equipped with a left ventricular diastole module (BDC Laboratories) was connected to the pump to generate unidirectional flow and

adjust the diastolic negative pressure during the suction stroke of the piston pump. Either built-in or arbitrary physiological waveforms can be generated through using software installed on the computer, making the pulsatile pump suitable for generating different physiological flow conditions.

A compliance chamber and a flow resistance are installed to simulate arterial compliance and resistance in this circulation, which is crucial in adjusting the pressure waveform during the whole cardiovascular cycle (i.e., systolic or diastolic periods). A 20-liter fluid reservoir was installed upstream of the pulsatile pump to collect the returning fluid mixture and a magnetic stirrer was attached to mix the seeding particles to prevent particles clustered.

A test section was installed in the center of the system, which is a transparent acrylic cubic box with the silicone aortic valve models or aortic arch models placed inside. The aortic models (BDC laboratories) used in these experiments were manufactured by silicone molding based on a clinically scanned three-dimensional (3D) CAD model of an actual aortic root or arch. High frequency pressure transducers (BDC-PT, BDC laboratories, normal sensitivity: 5 μV/mmHg, < +/−1%, frequency response 5 kHz, operating pressure range −362 mmHg to 3878 mmHg) are implemented at several locations along the system to monitor the pressure changes either through the pump head or across the models upstream and downstream. The pressure data was acquired through a LabView DAQ module (National Instruments, Austin, TX, USA) and fully calibrated with a linear correlation between voltage and pressure values.

Particle Image Velocimetry (PIV) visualization setup was also employed to investigate the movement of fluid flow inside the aortic valve or arch models for data post-processing in this experiment. PIV technique will be detailed described in the following section.

2.2. Particle Image Velocimetry (PIV) System

PIV is a flow visualization method, which is utilized to capture instant velocity measurements and flow properties. A typical PIV system consists of light sources (lasers), optics (cylindrical and spherical lens), digital image recording - normally CCD (charge-coupled device) cameras, small seeding particles, a synchronizer and post-processing algorithm [100]. Figure 2.2 briefly shows a typical setup for PIV experiment. In our PIV system, the working fluid is seeded with small diameter seeding particles which could follow the fluid flow and are illuminated by the light sources emitted from lasers so the movements of seeding particles become visible. The CCD camera and the lasers were connected to a delay generator to synchronize PIV components as well as the external triggering signal from the pump. Temporal offsets between the external triggering signal and the laser trigger were controlled to get desirable phase-locked measurements from cycle to cycle. Then the captured raw images were used to post-process the speed and direction of the fluid flow in the experiments.

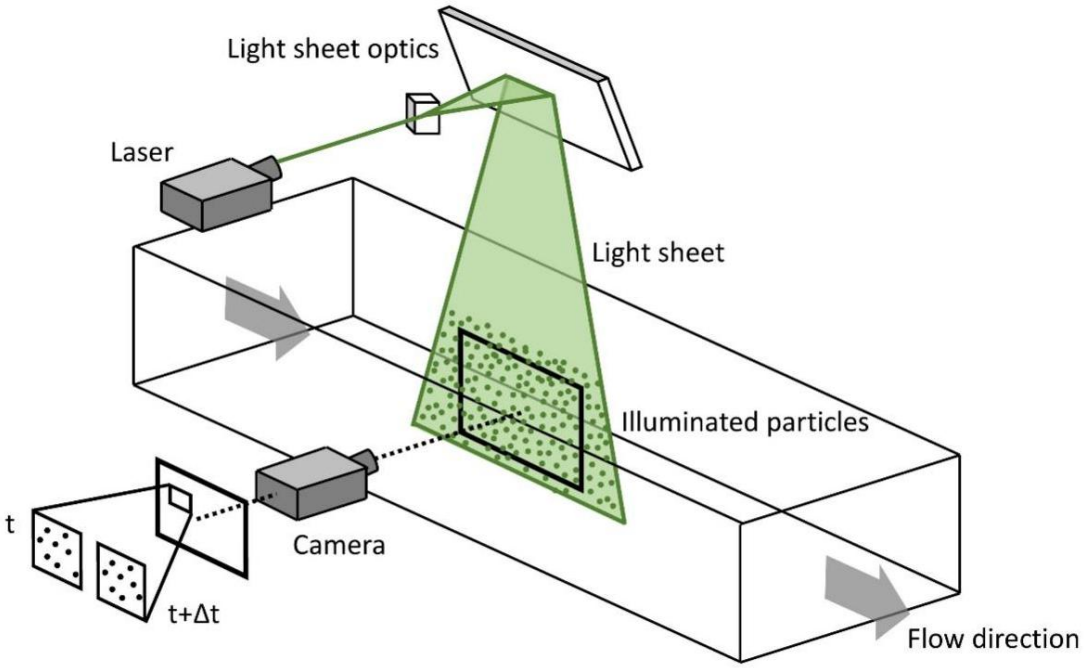

Figure 2.2. Schematic of a typical setup for PIV experiment [101].

There are several kinds of gas lasers used as light sources in PIV, including Helium-neon lasers (He-Ne lasers λ = 633 nm), Argon-ion lasers (Ar+ lasers λ = 514 nm, 488 nm), Semiconductor lasers, Ruby lasers (CrH lasers λ = 694nm, very first lasers) and Neodym-YAG laser (Nd:YAG lasers λ = 532nm) [101]. In our research, the Nd:YAG lasers (four-level system) are used, which are the most important and commercially used solid-state lasers in PIV. The first specific operation of Nd:YAG lasers was revealed by J.E. Geusic et al. in the year of 1964 [102]. In general, the Nd:YAG lasers are pumped through using a flash-lamp and it could be operated in either pulsed mode or continuous mode [103]. Normally, the Nd:YAG lasers operated in the pulse mode are also called the Q-switching mode. Under this Q-switching mode, there is an optical switch installed in the cavity of the laser, which is waiting for a max population inversion in the neodymium ions before it turns on. After that, the light wave from the lasers could go through its cavity, decreasing the excited laser medium [104]. The high energy pulses generated from the lasers could be successfully frequency doubled to form a wavelength of 532 nm laser light, or higher frequency. Generally, the Nd:YAG laser system and all requirements are made regarding a wavelength of 532 nm (green, visible) and a repetition rate of 10 Hz of the two pulses. The trigger signals from this type of laser are all TTL compatible. The basic operating properties of the Nd:YAG laser are listed in the Table 2.1.

Table 2.1. Basic properties of the Nd:YAG laser [101].

Property	Parameter
Working temperature	15°C - 35°C
Cooling water	10°C - 25°C
Power requirements	220-240 V, 50Hz
Resolution	5 ps
Repetition rate	10 Hz
Pulse energy for each of two pulses	320 mJ
Delay between two laser pulses	0 – 10 ms

In the PIV experiment, the laser beam emitted from the lasers need to be shaped into a very thin laser sheet to illuminate the seeding particles in the test section. Normally, the cylindrical and spherical lens are typical and good combination for various experiments in PIV. The function of cylindrical lens is to expand the laser beam into a plane and the spherical lens could compress the formed plane into a very thin laser sheet. This is very important because the PIV technique itself could not measure movement perpendicular to the sheet. The minimum laser sheet thickness depends on the wavelength of the laser and happens at a specified distance from the optics. Figure 2.3 shows the example of light sheet generation using cylindrical and spherical optics under different views. Theoretically, this is the best place to arrange the analysis area. However, the combinations of those lens do not have a very strict rules of numbers and positions as long as it could shape the laser beam into the required laser sheet of high intensity based on the actual experimental conditions. Actually, in some experiments, the triangular mirrors are also usually employed to adjust the path of the laser beam coming from the laser to the target optics workbench.

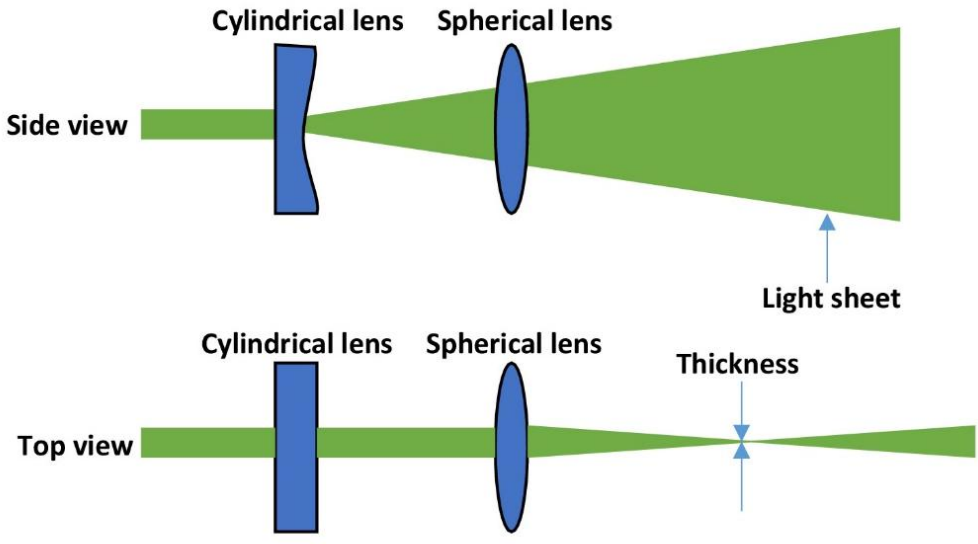

Figure 2.3. Example of light sheet optics arrangement.

In addition, the accuracy of the PIV measurement mostly depends on the quality of the captured images. Thus, a high quality and accuracy camera is critical and necessary to capture the images between a quite short time of double-pulsed lasers. Usually, the CCD faster digital camera that is made of semiconducting substrate material (usually silicon) is chosen as an electronic device to achieve this goal to take double frames at a very high speed during the PIV experiment, which could capture the frames within several hundred ns. Although the CCD cameras make it possible to take a pair of shots at a very high speed, they are much more expensive than the traditional cameras usually used at a slower speed. Nevertheless, the CCD cameras are selected in the actual PIV experiments due to making every exposure isolated, which is much more convenient and also could obtain a more precise cross-correlation analysis for the data post-processing in the PIV experiment. The CCD camera utilized in the current PIV study is shown in Figure 2.4 below, which was commercially manufactured and bought from LaVison Inc., Germany.

Figure 2.4. CCD camera used in the current PIV experiment.

Furthermore, the synchronization is also of great importance in the PIV experiment. In our PIV system, the lasers and CCD camera were synchronized by a delay generator (BNC Model 577, Berkeley Nucleonic Corp.), which was externally triggered by a digital signal from the programmable pulsatile pump. The delay to the trigger signals was then controlled

specifically for each test case to obtain phase shifts. The uncertainty of the synchronizing (based on the rise time of TTL signal) was less than 3 ns. In order to trace the movement of the flow field, the timing between each laser pulse and the camera exposure is quite critical, which can influence on the velocity data post-processing. Figure 2.5 shows a typical external trigger diagram.

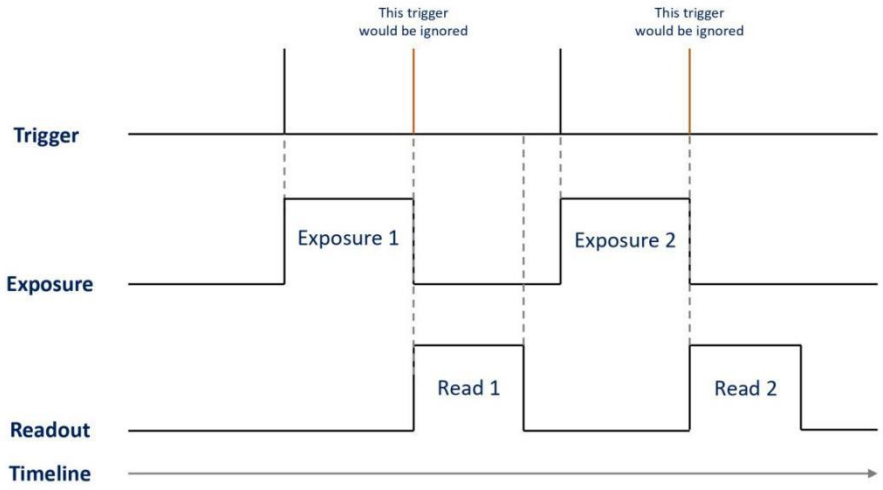

Figure 2.5. A typical external trigger diagram [105].

2.3. PIV Data Post-Processing

After collecting data, the analysis and processing of the obtained data are a great challenging that decide the final results of the flow field. In our studies, the post-processing are done by DaVis software commercially bought from LaVision Inc. to evaluate the instantaneous velocity vectors of the flow fields. During the PIV data processing, cross-correlation technique plays a key role, which is a signal processing methodology used to compute the similarity of two series (displacement of one relative to the other).

The algorithm processes two frames of particle images with multi-pass interrogation process. Most of the data processing procedure depends on the commercial software that uses multiple pass methods and interrogation-window choices to further improve the analysis to

obtain a more accurate results in the end. A certain percentage effective overlap was also chosen in order to satisfy the Nyquist criterion. Here, the cross-correlation are used to find the movement of the same particle in a very short of time (Δt) in order to determine the peak velocity vector in the certain interrogation domain, which is based on the two exposures during a very short time. The Fast Fourier Transform (FFT) algorithm is used in the cross-correlation processing. In addition, the quality of the raw images has a direct impact on the PIV results. So image pre-processing procedure need to be done to improve the quality of the obtained raw images before getting into cross-correlation procedure. Figure 2.6 illustrates the basic procedure of the cross-correlation technique during the data processing. In the selected interrogation windows, you can find f(i,j) in image 1 and g(i,j) in image 2 are selected at the same location with in a very short of time Δt (time gap). The cross-correlation procedure in this area can be described as follows: $\emptyset(i,j) = F[f(i,j), g(i,j)]$. Then, the cross-correlation peak's location related to the average shift of seeding particles (dx(i,j),dy(i,j)) within the interrogation windows can be found in this cross-correlation domain. This particle shift is converted to physical space that provides a velocity vector for flow fields [106].

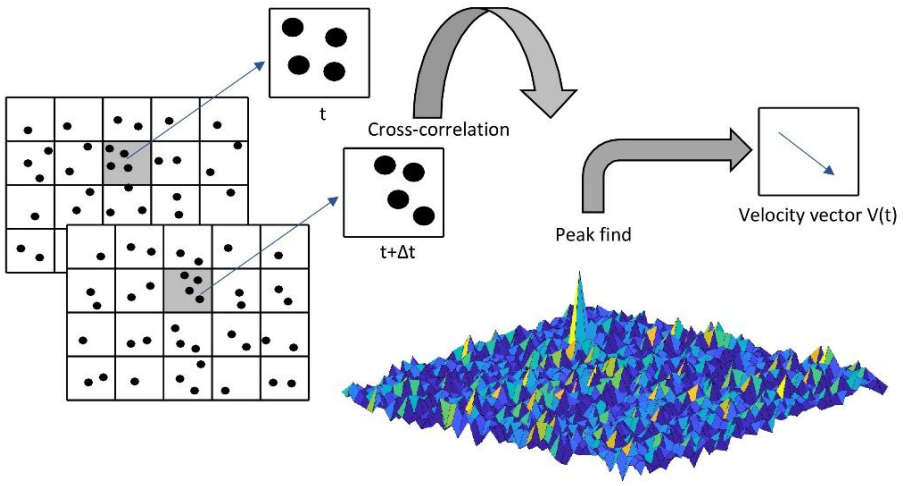

Figure 2.6. Schematic of cross-correlation technique in processing data [107].

In this study, during the image pre-processing, the sliding background of the raw images was subtracted with the scale length 16 pixel. The interrogation window was selected from window size of 32 × 32 to 16 × 16 pixels. A 50% overlap was chosen to meet requirements and saves more processing time (around 8 times faster than 75% overlap). The time-averaged quantities were obtained from a cinema sequence of 300 frames of instantaneous velocity fields for each case. The commercial tecplot 360 software was utilized to generalize the graphical flow fields based on the post-processed PIV data. Figure 2.7 indicates the realistic operational parameters for PIV data post-processing on the DaVis software.

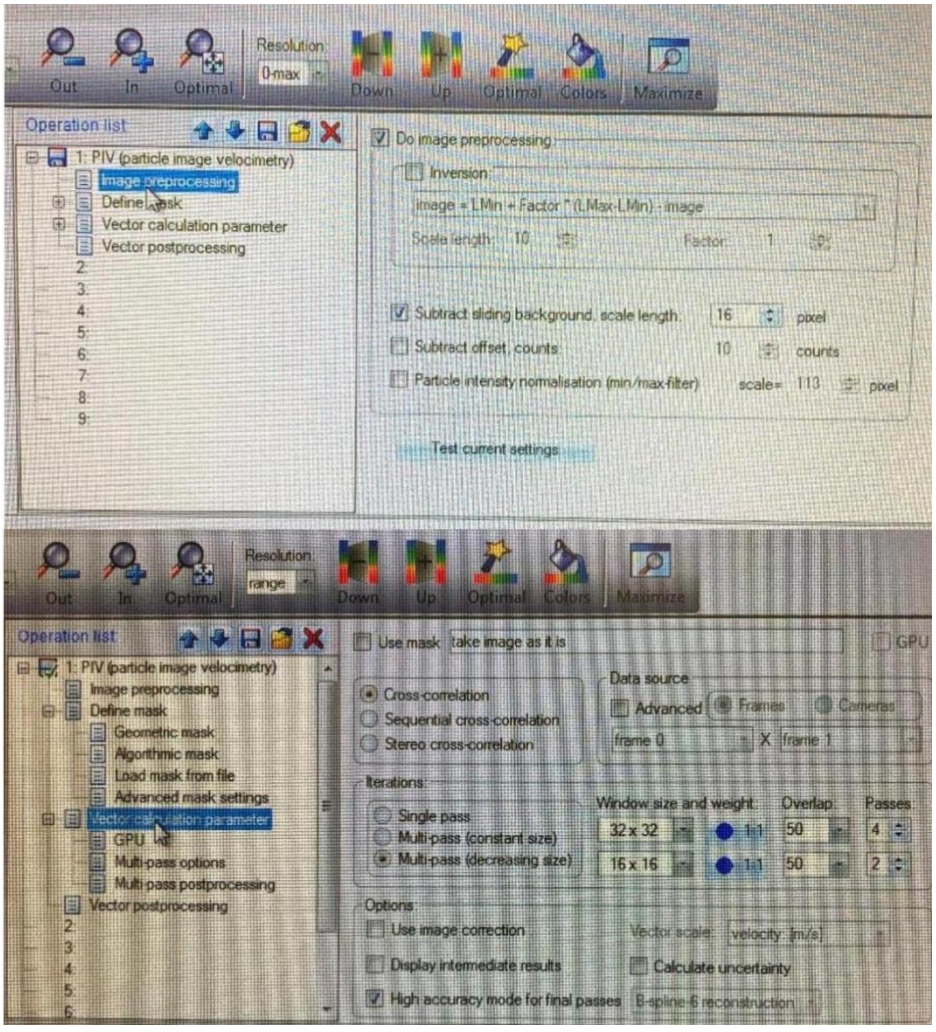

Figure 2.7. Operational parameters for data post-processing on the DaVis software.

2.4. Selection of Working Fluids

As blood analogs, the working fluid should comply with the properties of the blood and also suitable for the in-vitro experiment without involving too much errors or uncertainties. Fluid should be colorless, clear and transparent to avoid blocking and disturbance, and to ensure a minimal visual distortion. Therefore, the refractive index (RI) of the operating fluid is very important, which should be equal or close to that of the test section to forbid or minimize optical distortion under a certain light wavelength [108].

Two classic formulas for RI matching estimation are listed here. One of them is called the Newton equation which is shown in equation 2.1 below.

$$N_{mix}^2 = \emptyset_1 N_1^2 + \emptyset_2 N_2^2 \tag{2.1}$$

where N_{mix} is the RI of the mixture; N (i = 1, 2) is the index of refraction of each pure liquid; Φ (i =1, 2) is the component volume fraction of the mixture of each pure liquid.

The other one is the Gladstone-Dale equation and it is the simplest one which is easy for understanding and calculating especially for the water-glycerin mixture [109]. The equation 2.2 below shows the Gladstone-Dale relationship in detail:

$$\frac{N_{mix}-1}{\rho_{mix}} = \frac{N_1-1}{\rho_1} p_1 + \frac{N_2-1}{\rho_2} p_2 \tag{2.2}$$

where ρ_{mix} is the density of the mixture; ρ (i = 1, 2) is the density of each pure liquid; p (i = 1, 2) is the component weight fraction of the mixture of each pure liquid.

It should be noted that all the derived theoretical formulas are according to the basic electromagnetic theory of light and, thus, are limited to mixture that has no volume changed after mixing together [110]. For current PIV experiments, RI matching need to be examined ahead of each experiment due to the varieties of the experimental models used.

Representative operating fluids that fulfill this requirements using in PIV experiments are shown below in Table 2.2, in which the usage and properties of operating fluids are also summarized according to related literature reviews. Solution of around 40% glycerin and 60% water by volume is the most common and widely used operating fluid, which can maintain a viscosity of around 3.5 centistokes (cSt) and a RI about 1.42 (Table 2.2). However, given a high proportion of glycerin included, the viscosity of it may be greater than real blood. And also given its relatively low RI, the range of the choice of test section is relatively limited in fact. As a result, saturated aqueous sodium iodide or chloride is often included to replace some glycerin and water and increase the RI of the operating fluid. As an example, the solution of 79% saturated aqueous sodium iodide, 20% glycerin and 1% water can generate a RI of 1.49 which perfectly suits that of Polymethylmethacrylate (PMMA). In addition, glass, Polyformaldehyde (POM) and Polysiloxane (Silicon rubber) are also possible choices for other experimental conditions. Due to the limitation of RI that operating fluid can reach, materials like Nylon 6,6, Polycarbonate (PC) and Polystyrene (PS), etc. with RI higher than 1.57 - 1.58 are normally not applicable for test section [110].

Table 2.2. Summary of selected operation fluids in different PIV studies.

References	Test fluid Water	Glycerin	Sodium iodide	Sodium chloride	Viscosity (cSt)	Density (kg/m^3)	Refractive index (-)
Lim et al. [67]; Lim et al. [77]; Brucker et al. [111]; Manning et al. [112]; Kaminsky et al. [113]; Brunette et al. [114]	✓ 60-64%	✓ 35-40%			3.5	1010-1200	1.41
Brunette et al. [115]; Buchmann et al. [116]; Hegner et al. [117]; Hasler et al. [75]; Büsen et al. [118]	✓ 39-43%	✓ 57-61%			3.6	1110-1150	1.41-1.43
Ge et al. [51]; Leo et al. [23]; Dasi et al. [53]	✓ 1%	✓ 20%	✓ 79%		3.5	-	1.49
Haya and Tavoularis [119]	✓ 47%	✓ 37%	✓ 16%		3.65	1230	1.41
Vennemann et al. [120]	✓ 24%	✓ 57%	✓ 19%		3.5	-	1.48
Hasler and Obrist [121]	✓ 50%	✓ 33%		✓ 17%	4.8	-	-

Based on detailed previous research, the information of selected experimental liquid is stated below in detail. The experimental aortic models used in these studies are made of silicone which is nearly clear and soft material with a refractive index (RI) around 1.43 (slightly varies in models). To minimize the optical distortion caused by structure and material, a mixture of water - glycerin (40% and 60% respectively by volume) was chosen as the working fluid in the current experiments. The RI of the fluid mixture was measured by a digital refractometer under the ambient temperature, which technically matched the RI of the experimental silicone models. Meanwhile, to check the accuracy of the calculated data and the experimental data by ourselves, the RI of the mixture of water - glycerin by volume has been estimated through Eq. 2.1 and Eq. 2.2 mentioned above and compared with the experimental data shown in Figure 2.8. The RI of the water and glycerol used in calculation through the theoretical equations were 1.3334 and 1.4737 respectively, which were all measured in this experiment under ambient temperature. It could be seen that the experimental data showed a very similar trend as that of the calculated data (i.e., both through Eq. 2.1 and Eq. 2.2). Although some difference was observed, it was deemed as completely acceptable. It may be due to the limitation of the experimental conditions and the uncertainty of the experimental facilities themselves. Overall, the obtained experimental RI data of the mixtures for different fractions are all within the reasonable ranges based on the research of Cozzi et al. [122]. In addition, according to the measurements, the selected working mixture has a density of $\rho = 1{,}160\ kg/m^3$ and a dynamic viscosity of $\mu = 0.012\ Pa{\cdot}s$.

Figure 2.9 below shows the schematic of silicone models (aortic valve and arch) and RI matching. It should be noted that the non-Newtonian fluid property of blood due to the existence of red blood cells were not considered in the present studies. Although the non-Newtonian property of blood was found to have an impact on the increased wall shear stress (WSS),

numerous studies also suggested that non-Newtonian property does not significantly affect the overall flow patterns and characteristics particularly at mid-to-high flow velocities, as suggested by a lot of previous PIV studies [123], [124].

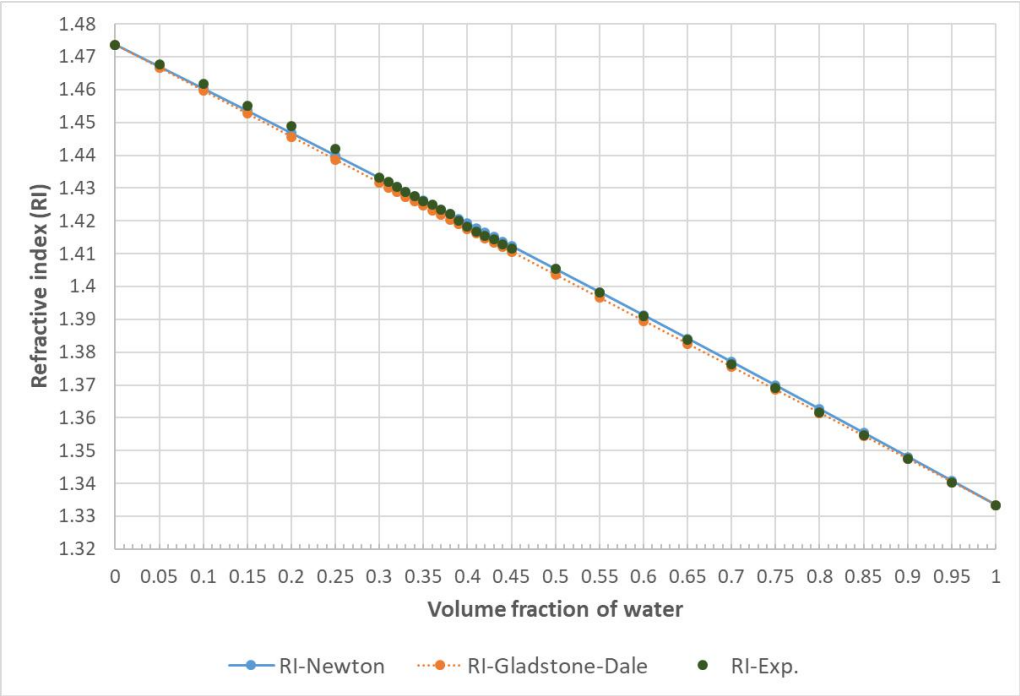

Figure 2.8. Comparison of experimental RI data (green dot) with those calculated by Eq. 2.1 (blue solid line) and Eq. 2.2 (orange dashed line).

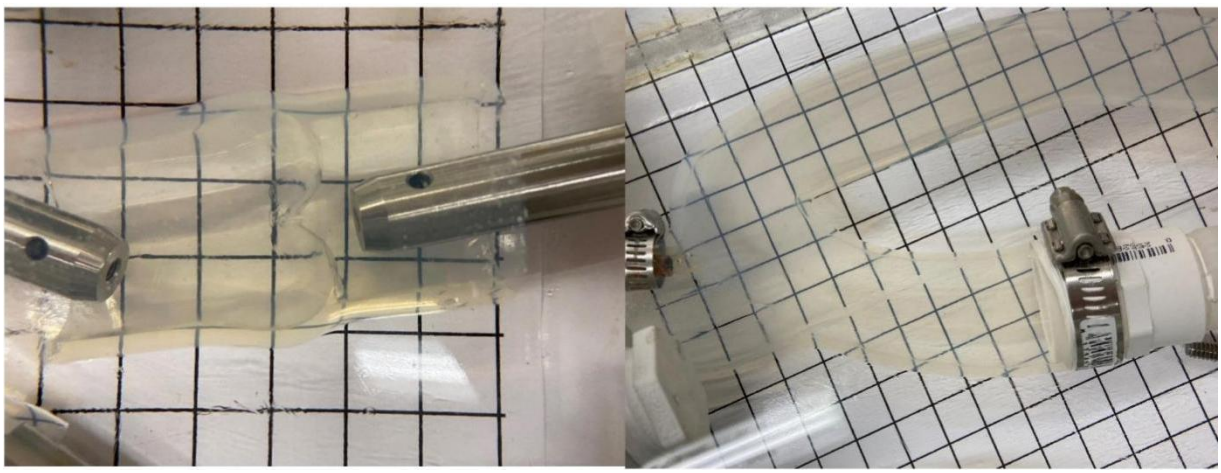

Figure 2.9. Schematic of silicone models and refractive index matching.

2.5. Selection of Seeding Particles

PIV relies on scattering particles suspended in the flow to provide velocity information of the working fluid. The selection of seeding particles has been summarized in a number of review papers [110], [125]. To obtain a good imaging resolution, the particles, firstly, should not absorb any radiation from the illumination source and also show a good reflectivity. Potential materials including groups of plastics, glass, and some certain synthetic rubbers could be selected as the candidates for this sort of experiments [110].

Besides, since PIV works in measuring the distance of particles moved in a certain period of time instead of measuring the velocity directly [126], the accuracy of PIV is usually related to the particles' quality to trace the movement of the flow field. This ability depends on the aerodynamic diameter of the particles, which is a function of the geometric diameter and density following the formula of $d_a = d_g\rho$. However, various factors need to be considered in choosing the optimal particle diameter. Basically, the seeding particles should be small enough to follow the working fluid and does not disturb the fluid characteristics. In the meantime, the seeding particles should also be large enough to reflect the required amount of light so that the movement of them could be captured [125], [127], [128].

In addition, to obtain the suitable aerodynamic diameters, the particles should also be better around the density of the liquid to obtain a good suspension condition by adapting to the liquid. It is permitted to be a little bit higher or lower because the density varies due to small variation in temperature and the existence of Boycott effect. But, normally, the density should be within a reasonable range, which is quantified by the sedimentation or rising time inside the fluid following the equation below (Eq. 2.3) [110], [129], [130]:

$$V_{sedim} = (1 - 6.55\emptyset)\frac{(\rho_p - \rho_f)gd_p^2}{18\cdot\eta} \tag{2.3}$$

where, V_{sedim} is the sedimentation velocity; ρ_p and ρ_f are the porosity of particle and fluid, respectively; d_p is the diameter of the particle; η is the dynamic viscosity of the fluid.

As a result, the selection of tracer particles should be made by considering the specification of the laser, the selection of operating fluid and the choice of particle materials. A compromise among the particle types, diameter and density can be obtained. Melling [125] has given the recommended diameter ranges for different particle types under different laser specifications. Seen from Table 2.3, particles with diameters ranging from 1 to 100 μm have been utilized with great variation among studies. Titanium dioxide TiO_2 particle is the smallest among all, which ranges from 2 – 5 μm [115]. Particles of melamine resin and hollow-glass particles are mainly around 10 – 20 μm [51], [112], [116], and Rhodamin B-particle ranges from 10 μm [111] and 20 – 50 μm [75]. Aluminum particles are the biggest among all, which is around 100 μm [67], [77]. The density of seeding particles does not vary too much, which normally ranges from 1,016 to 1,200 kg/m^3.

Therefore, based on careful consideration about previous studies and the experimental conditions, the working fluid was seeded with hollow glass microspheres with a seeding density of 0.1 ppm in our PIV experiments, which has been adopted by many experimental studies previously [51], [116]. The diameter of seeding particles we used range from 10 to 50 μm, and the density is about 1,100 kg/m^3, which was quite close to the density of the working mixture. A dimensionless parameter – Stokes number (Stk) is used to characterize the behavior of the seeding particles suspended in the fluid flow. The definition of Stroke number is the ratio of the characteristic time of the particle to a characteristic time of the obstacle. The definition equation of Stokes number is shown below (Eq. 2.4) [131]:

$$Stk = \frac{t_0 u_0}{l_0} \tag{2.4}$$

where t_0 means the relaxation time of the particle, u_0 means the fluid flow velocity well away from the obstacle, l_0 is the diameter of the obstacle. In this experiment, the Stokes number of the particle flow was much less than 1, which indicates that the seeding particles could follow the flow streamline very well.

Table 2.3. Summary of selected particle in valve and non-valve PIV studies.

Seeding particles	Diameter (μm)	Density (kg/m^3)	References
Aluminium particles	100	-	Lim et al. [67]; Lim et al. [77]
Hollow glass spheres	10	1,100	Manning et al. [112]; Ge et al. [51]; McNally et al. [132]
	20	-	Buchmann et al. [116]
	30	1,016	Susin et al. [133]
Polyamide particles	60	-	Hegner et al. [117]
PMMA micro	20-50	1,180	Hasler et al. [75]
particles	1-20	-	Leo et al. [23]; Dasi et al. [53]; Büsen et al. [118]; Okafor et al. [134]
Titanium dioxide particles	2-5	-	Brunette et al. [115]; Brunette et al. [114]
Rhodamin B-particle	10	-	Brucker et al. [111]
	35	1,200	Vennemann et al. [120]
Others	50	1,050	Kaminsky et al. [113]
	-	-	Amatya et al. [135]
	-	-	Hasler and Obrist [121]

3. AN EXPERIMENTAL STUDY OF PULSATILE FLOW IN A COMPLIANT AORTIC ROOT MODEL UNDER VARIED CARDIAC OUTPUTS[1]

3.1. Introduction

Valve replacement is one of the major treatments for valvular heart diseases. Each year, approximately 300,000 patients go through either percutaneous surgeries or transcatheter aortic valve replacement procedures [136] to replace calcified aortic valves [137]. However, the clinical outcomes of valve replacements are still far from satisfactory. Patients with replacement valves suffer from a 14 % chance of recurrence of regurgitation and more than a 60 % risk of death in five years [137]. Thus, an improved understanding of the fluid and structural dynamics in the real aortic geometry is very critical to enhance clinical outcomes and future prosthetic designs. Recently, experimental studies employing particle image velocimetry (PIV) technique have been an important method in cardiovascular hemodynamic researches. PIV studies on physiological phantoms provide reliable flow simulations resembling the in vivo flow from magnetic resonance imaging (MRI) [138] and help set benchmarks for patient-specific computational fluid dynamic (CFD) simulations [139]. Over the past years, in vitro experimental studies have made a great contribution to the knowledge of hemodynamics within the soft-tissue organs, such as heart and other vascular systems [140]-[144], and the evaluation and validation of cardiovascular assist devices [145], [146].

The hemodynamics of the aortic replacement valves have been a focus of experimental and fluid visualization studies in the past two decades. Lim et al. [67] investigated the fluid dynamics in four prosthetic mechanical valves under steady flow conditions using PIV measurements. Similar research on the mechanical valves has also been conducted under

[1] The material in this chapter is adapted from the publication - R. Zhang, and Y. Zhang, "An experimental study of pulsatile flow in a compliant aortic root model under varied cardiac outputs," Fluids, vol. 3, no. 4, Oct., pp. 71, 2018. https://doi.org/10.3390/fluids3040071.

pulsatile flow conditions [111]. Apart from flow characteristics, researchers have also been able to analyze other biomedical indicators through various in vitro experimental setups, e.g., energy loss, to assess aortic stenosis and the performance of mechanical valves and stented valve prostheses [70]-[72]. In addition, the fluid dynamics and fluid-structure interaction (FSI) of compliant aortic valves such as bio-prosthetics and native tissue aortic valves, which have soft leaflets that could result in better hemodynamics, have been studied extensively [57]-[59], [147]. For example, Leo et al. [23] assessed the fluid dynamic characteristics downstream of polymeric prosthetic valves through PIV measurements. Saikrishnan et al. [78] assessed aortic valves with native tissues leaflets, i.e., bicuspid aortic valves, and found that the turbulent kinetic energy and vorticity of the flow downstream of the valve were significantly increased in a bicuspid porcine tissue valve. Pisani et al. [148] and Salica et al. [149] further demonstrated the important role of the sinuses of Valsalva (aortic sinus) in the regulation of the aortic hemodynamics. They found that the presence of the sinuses of Valsalva increases the effective orifice area when the cardiac output increased, which helps minimize the flow energy loss during ejection. However, most of the above-mentioned research addressed the hemodynamics of the artificial aortic valves, where the stented replacement valve models were placed into simplified or rigid tube models. The geometric complexity and compliance of the aortic root and valve leaflets were seldom considered. Additionally, the effect of reduced cardiac output (CO) on the aortic flow hemodynamics, which is often associated with the left ventricular dysfunctions [150], has not been extensively studied. The reduced CO is not a rare medical condition, and particularly the low cardiac output syndrome (LCOS) is the most common and serious complication associated with short and long-term mortality after cardiac surgeries [150], [151], in which the cardiac

index can be lower than 2.0 L/(min·m^2). These research gaps result in a scarcity of important validation benchmark data for CFD and FSI simulations in realistic aortic root models.

In this chapter, we investigated the fluid dynamics of a 1:1 scale silicone aortic root model with a realistic three-leaflet aortic valve based on an experimental cardiovascular flow simulator in a closed flow loop. The system, which was equipped with high-frequency pressure sensors, was then synchronized with a PIV system to gather flow field data at different phases. The results were analyzed to obtain average flow information, ensemble turbulent characteristics, as well as the corresponding structural deformations. The results were then compared with those from experiments under varied COs to generate insights on the impacts of this common variation of physiological boundary conditions.

3.2. Experimental Methods

3.2.1. The Cardiovascular Flow Simulator

The experiments have been conducted in a closed-loop flow circulation system, as illustrated in Chapter 2 and shown in Figure 3.1. The pulsatile flow conditions were generated by a programmable pulsatile pump (PD-1100, BDC Laboratories, Wheat Ridge, CO, USA), which a pump head module is customized to simulate the left ventricle (LV) function. Compliance chamber and resistance units were used downstream to maintain appropriate flow and pressure conditions. And a reservoir was used to store the working fluid and seeding particles. Pressure transducers (BDC-PT, BDC laboratories, normal sensitivity: 5 μV/mmHg, < +/−1 %, frequency response 5 kHz, operating pressure range −362 mmHg to 3878 mmHg) have been installed to monitor the pressure either inside the pump head or across the model. A silicone aortic root model was fixed in a transparent acrylic test section. The model was constructed (Figure 3.2, commercially obtained from BDC laboratories) by silicone molding based on a clinically

scanned three-dimensional (3D) CAD model of a realistic aortic root, which has an inner diameter of 25 mm and an average wall thickness of 2 mm. The average thickness of the leaflets is less than 1 mm, and they are tapered from the root to the tip. Under room temperature and low frequency (1-Hz) loading, the dynamical mechanical analysis of the material shows high elasticity (storage modulus 1.3 MPa) and low viscosity (loss modulus 0.086 MPa), suggesting that minimal energy dissipation will occur during deformation under the current cyclic loading. It should be noted that although the silicone model represents a certain degree of the compliant nature of the aortic root and valve leaflets, the material properties do not replicate those of the non-linear viscoelastic native tissues.

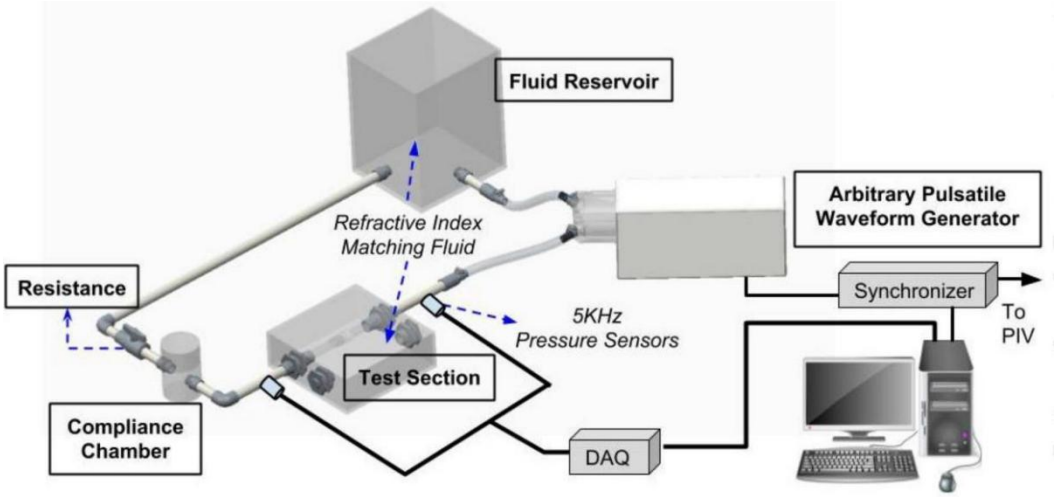

Figure 3.1. Schematic of the cardiovascular flow simulator.

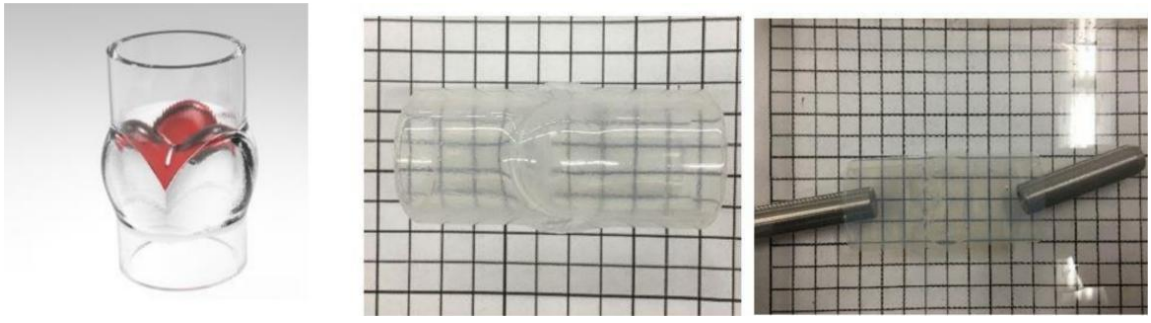

Figure 3.2. The silicone aortic valve model and refractive index matching.

3.2.2. Particle Image Velocimetry (PIV)

The quantitative flow parameters were measured by utilizing a phase-locked PIV system. A double-pulsed Nd:YAG laser (Gemini 200, New Wave Research, Inc., Fremont, CA, USA, 100 mJ, 532 nm) was used to illuminate the flow field. A set of spherical and cylindrical lenses and a 2M-pixel CCD (charge-coupled device) camera (LaVision, Ypsilanti, MI, USA) were together used to shape laser beam and catch images. Then, they were connected to a delay generator that synchronizes these components. The PIV system was externally triggered by the pulsatile pump signal to capture phase-locked images. For this study, instantaneous PIV velocity vectors were computed through cross-correlation method, which involved successive frames of patterns of particle images in a multi-pass interrogation process from a window size of 32 × 32 to 16 × 16 pixels. An effective overlap of 50 % was employed to satisfy the Nyquist criterion. The time-averaged quantities were obtained from a cinema sequence of 300 frames of instantaneous velocity fields for each case. The field of view is set to be 65 mm by 45 mm, resulting a spatial scale of approximately 0.0375 mm per pixel. Thus, the resolution of vector data based on the 16 × 16 pixels investigation windows is estimated to be 0.6 mm. The uncertainty factors affecting the PIV measurements are the optical error of the CCD camera and numerical error of the cross-correlation algorithm. The uncertainty of the PIV results in such an experimental setting is very low (approximately 0.2%) according to a similar study using the same LaVision CCD camera [78].

To minimize the optical distortion, a mixture of water–glycerin (40 % and 60 % respectively by volume) was used as the working fluid, which has a density of ρ = 1,160 kg/m^3 and a dynamic viscosity of μ = 0.012 Pa·s. The refractive index (RI) of the mixture measured by a digital refractometer was 1.43 under ambient temperature, which matched the RI of the silicone

valve model. It should be noted that the non-Newtonian fluid properties were not considered in the present study. The fluid mixture was seeded with hollow glass microspheres (10 μm in size, and of density at 1,100 kg/m^3) with a seeding density of 0.1 ppm, which has been adopted by many previous experimental studies [51], [116]. These particles were quite close to the density of the working liquid and results in a Stokes number that is much less than 1.

3.2.3. Experimental Conditions

In normal healthy population, the cardiac output (CO) varies from person to person due to aging. A significant reduction in CO could occur in relevant heart diseases, such as valvular stenosis, cardiac arrhythmia, and heart failure [152]. To study the effect of cardiac outputs on the flow and structure responses, three different flow rates, i.e. 4 L/min (normal), 2 L/min, and 1 L/min were tested in the present experiments, corresponding to a stoke volume of 66.7 mL, 33.3 mL, and 16.7 mL, respectively. In this experiment, a pressure waveform was generated by setting a 50 % systolic duration (compression of the LV) of a complete cardiac cycle. According to Sarnari et al. [153] and Chung et al. [154], the systole-to-diastole (S/D) ratio varies significantly among patients within different age, body surface area, and heart rate groups. Out of 752 patients from children to young adults [153], the S/D ratio ranges from 0.397 to 1.62, with a mean of 0.995 ± 0.23. Therefore, based on this clinical evidence, a 1:1 ratio sinusoidal wave (50% systole) has been used in many previous fluid dynamic studies [75], [78]. In all of these tests, the heart rate was fixed at 60 beats per minute (bpm), i.e., one second between two heartbeats, to enable a better synchronization between the pump and the laser system.

Two non-dimensional parameters, i.e., the Womersley number and Reynolds number, are normally used to describe the periodicity and the dynamic similarity of physiological pulsatile flow in in vitro experiments. The Wo and peak Re are defined by:

$$\alpha = d_a\sqrt{\omega\rho/\mu} \tag{3.1}$$

$$Re = \rho d_a u_a/\mu \tag{3.2}$$

where d_a is the diameter of the valve; u_a represents the velocity of the maximum jet flow; ρ represents the density of the working liquid; μ is the dynamic viscosity; ω is the angular frequency of the pulsatile flow. The Wo and peak Re results from this experiment are listed in Table 3.1. The peak Re is 4,370 for 4 L/min at the peak flow rate of a cycle, which is slightly lower than the normal range of peak Re for healthy subjects (around 4,500 – 10,000 reported from different literatures, e.g. Stein [40] and Fung [155], [156]) due to the current limitations of the setup. According to Trip et al. [157], when the mean Re is above 2,500, the turbulent statistics of the pulsatile pipe flow become almost independent of Re and Wo. Therefore, many similar research studies using a moderately lower Re between 3,000 – 4,500 have all successfully captured the major characteristics of the pulsatile flow [75], [147], [158].

Table 3.1. Basic hemodynamic and non-dimensional fluid dynamic parameters.

Cardiac Output [L/min]	Stroke Volume [mL]	*Re*	Wo
1	16.7	903	
2	33.3	2,249	11.7
4	66.7	4,370	

To evaluate the structure deformation under the pulsatile flow, two parameters, i.e., the area strain (AS) and geometric orifice area (GOA) were analyzed by digitizing the phase-averaged PIV raw images. The concept of AS is adapted from an in vivo clinical study of aortic valve [159], which quantifies the deformation of the aortic root wall based on the following equations:

$$AS = (d_{max}^2 - d_{min}^2)/d_{min}^2 \tag{3.3}$$

where d_{max} and d_{min} represent the maximum and minimum diameters during a cardiac cycle for a specific cross-section. Specifically, AS was quantified at three sites, i.e., aortic annulus, sinus, and sinotubular junction, as shown in Figure 3.3a.

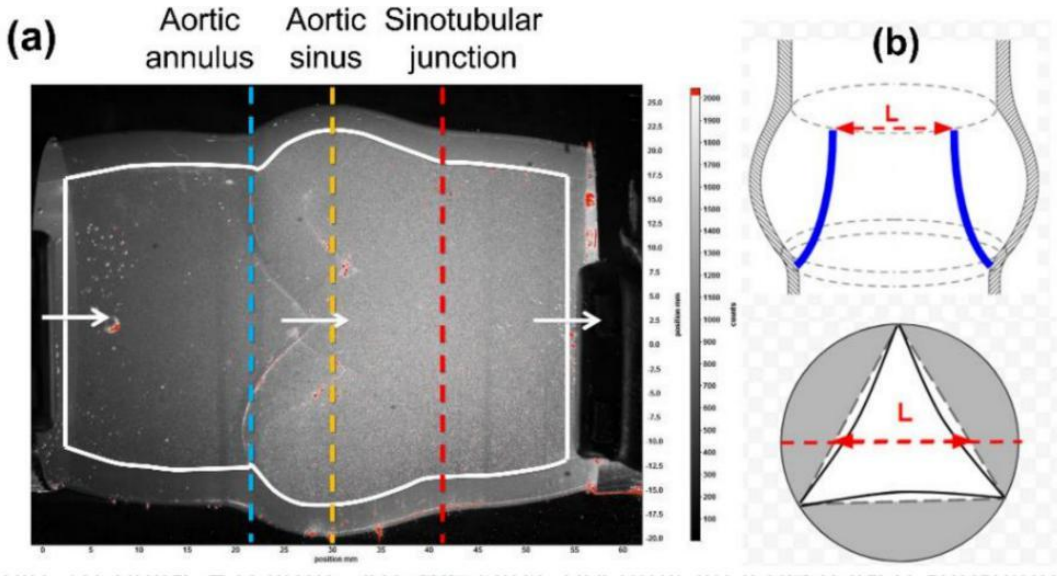

Figure 3.3. Example raw image of the aortic root demonstrating (a) three major sites (aortic annulus, sinus, and sinotubular junction) for deformation analysis and (b) the effective length of the orifice (L).

The GOA can be estimated by calculating the area of an assumed triangular-shape opening, which is defined as:

$$GOA = \frac{9\sqrt{3}}{16} L^2 \tag{3.4}$$

where L represents the length of the orifice in the investigated two-dimensional (2D) plane, which can be seen in Figure 3.3b. It should be noted that the GOA does not stand for the exact opening area due to the two-dimensionality of the measurements, but rather serves as a close estimate. Both the diameters and orifice length were measured manually using a computer image digitizer from the raw PIV images. The uncertainty of these calculations is estimated to be within 10% based on the limited temporal resolution of the measured PIV image data, which is calculated based on the standard deviation from many digitized data in a single phase. Since the

phase-locked results do not fully resolve the temporal variations, the current calculations regarding structural deformation only served as an estimation of the quantitative trend as a function of varied flow conditions.

3.3. Results and Discussion

3.3.1. Phase-Averaged Flow Patterns in a Typical Cardiac Cycle

In the present experiments, the pulsatile flow was driven by the time-dependent pressure gradient across the aortic valve generated by the reciprocating piston pump, i.e., the LV function. Figure 3.4 shows the pressure gradient across the valve model as a function of time and the relative piston displacement during two cycles for 4 L/min. It is clear that during the systolic stroke of the pump (LV contraction), the positive pressure gradient spikes, and the peak value occurs at the mid-systole (maximum piston velocity). Through the transition from systole to diastole (LV relaxation), a mild negative pressure gradient briefly occurs due to the reversed piston displacement. The pressure gradient restores to approximately zero toward the end-diastole phase. The pulsatile flow variation was in accordance with the changes of the pressure gradient over time. To quantify the variations, PIV measurements were conducted at eight phase-locked conditions, as illustrated by the red dots in Figure 3.4a. Figure 3.4b shows that the peak pressure gradient and the magnitude of the negative pressure gradient during diastole both decrease proportionally as the CO reduces from 4 L/min. Meanwhile, the time to reach the peak pressure gradient is also slightly delayed due to the reduced CO. It should be noted that the maximum pressure gradient generated in the present study under 4 L/min CO is higher than that which is normally expected in a healthy native tissue aortic valve [78]. This is potentially caused by the greater flow resistance of the stiffer silicone valve leaflets in this bioengineering model compared with that of a native tissue valve.

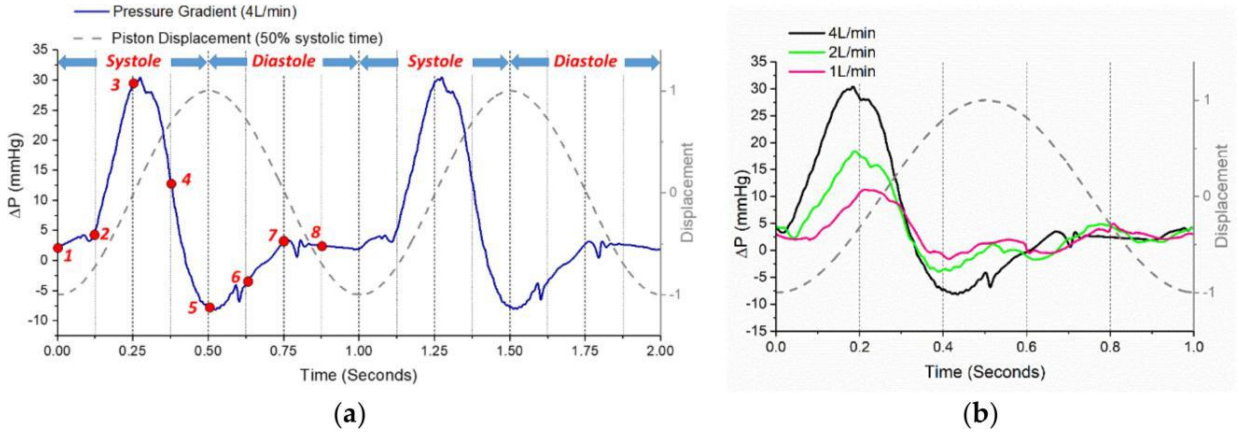

Figure 3.4. Pressure gradient waveforms (a) the pressure gradient in two cardiac cycles and the particle image velocimetry (PIV) measurement phases; (b) the pressure gradients under different reduced cardiac outputs.

Figure 3.5 shows the ensemble-averaged velocities in x and y directions inside the silicone model at different phases of a typical cardiac cycle. The boundary shapes of the aortic root and valve leaflets were also plotted as bold black lines based on the data extracted from the raw images, so that the interaction between the fluid and structures could be correlated. The dashed lines indicate the hinge locations of the valve leaflets. At phase 1 (Figure 3.5a), the heart valve was almost closed, and the phase-averaged flow velocities upstream and downstream of the valve were both very small. The v velocity contour clearly shows that a pair of vortices started to develop at the tip of the valve leaflets. At phase 2 (Figure 3.5b), the valve was pushed open, and the jet flow started to build up. The strength of both the u and v velocity components increased significantly. At phase 3 (Figure 3.5c), a clear central jet was developed, and the flow velocity increased dramatically both upstream and downstream (Figure 3.5c). At this peak systole phase, the valve reached its maximum opening, and started to close gradually afterwards. A strong out-of-plane vorticity ($\omega = \partial v/\partial y - \partial u/\partial x$) was observed at the interface of the jet flow (Figure 3.6a). At phase 4 (Figure 3.5d), the valve opening area decreased substantially, and the jet flow was weakened due to the decreased pressure gradient. The strength of flow

recirculation (vortices) was clearly enhanced at this phase at a few sites downstream from the valve, particularly in the sinus and near the wall boundary around the sinotubular junction (Figure 3.6b). At phase 5 (Figure 3.5e), due to the development of the negative pressure gradient, the jet started to dissipate, and the flow was split into a v-shaped pattern. The magnitude of vorticity downstream from the valve became much weaker (Figure 3.6c). At phase 6 (Figure 3.5f) and afterwards, the jet flow dissipated due to the vanishing pressure gradient and the closure of the valve. It is also clear that at this phase, the remaining flow upstream of the valve induced vortices near the root of the leaflets. Overall, it is evident that the variation of flow patterns is strongly associated with both the time-dependent pressure gradient and the dynamics of the flexible structures.

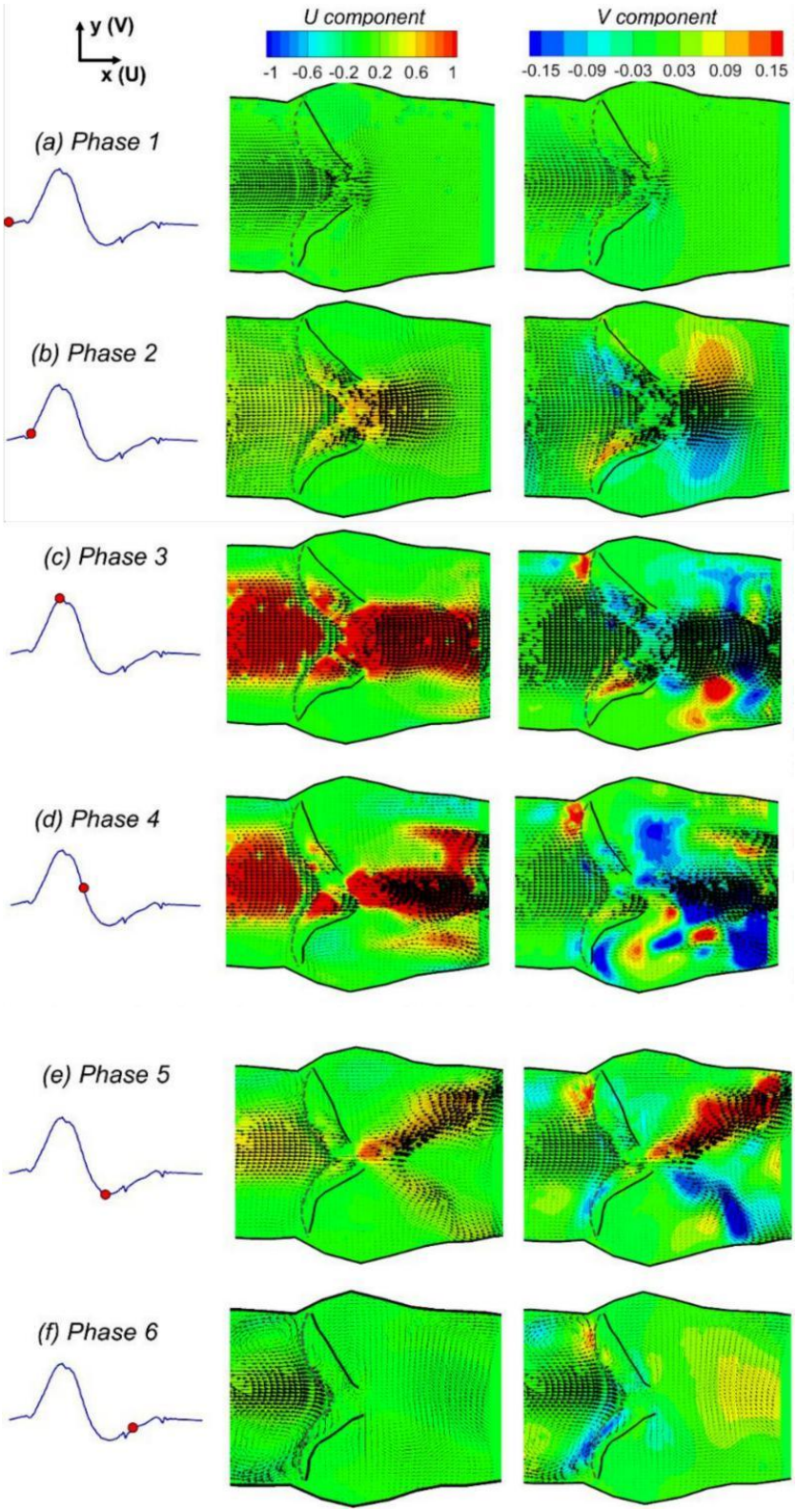

Figure 3.5. Contours of PIV phase-averaged velocity in *x* and *y* directions.

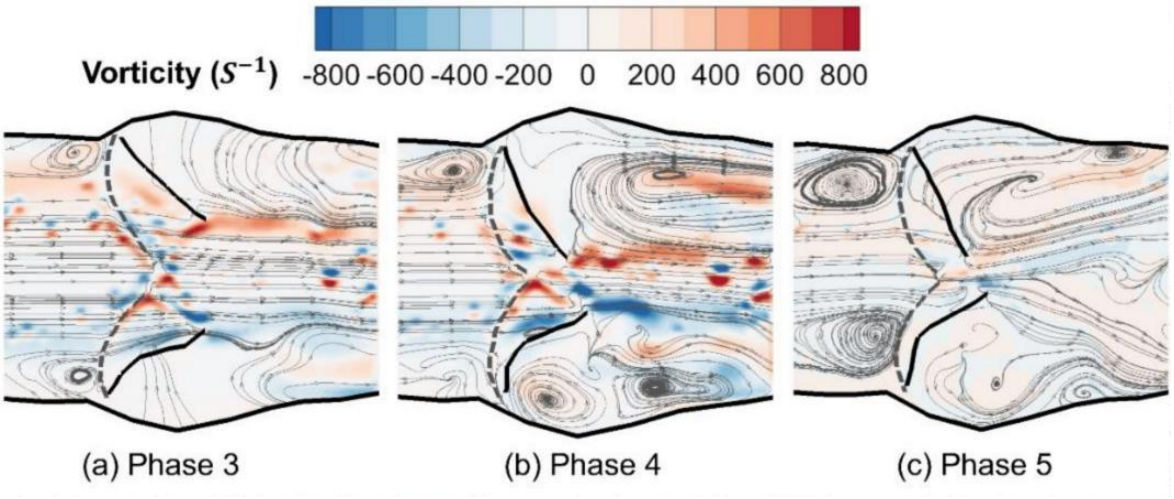

Figure 3.6. Out-of-plane vorticity fields at selected phases.

The level of turbulence during the pulsatile flow process was also obtained by evaluating the ensemble turbulence kinetic energy (TKE). The normalized 2D TKE were calculated as:

$$TKE = 0.5(\overline{u'^2} + \overline{v'^2}) / U_{peak}^2 \tag{3.5}$$

where u' and v' are the velocity fluctuation components in the horizontal and vertical directions, respectively, and U_{peak} is the peak centerline flow velocity, which is used for normalization for all of the phases. Figure 3.7 shows the TKE distributions at a few selected phases. It is clear that the turbulence was minimal at the beginning of the phases during the acceleration phase of the systole (Figure 3.7a,b). Particularly at phase 3 when the peak systolic velocity developed, the TKE was very low, and moderate TKE areas were only found near the interface of the jet flow downstream due to the fluid shear. However, at phase 4 (Figure 3.7c), right after the peak systole, the TKE downstream from the aortic valve increased dramatically as the valve started to close and the flow decelerated. At phase 5, when the negative pressure gradient built up, the overall magnitude of TKE was reduced. The flow energy dissipation caused a fan-shaped TKE distribution downstream from the narrowing orifice (Figure 3.7d). In the following phases, the TKE in the entire flow field quickly decreases to near-zero values (not shown for brevity) until

the next systolic jet flow develops. The entire process demonstrates that the instability of the pulsatile flow past the aortic valve bursts into turbulence during the initial deceleration phases and quickly dissipates (a quarter of a second in this study) during the diastole phases before the next cycle starts.

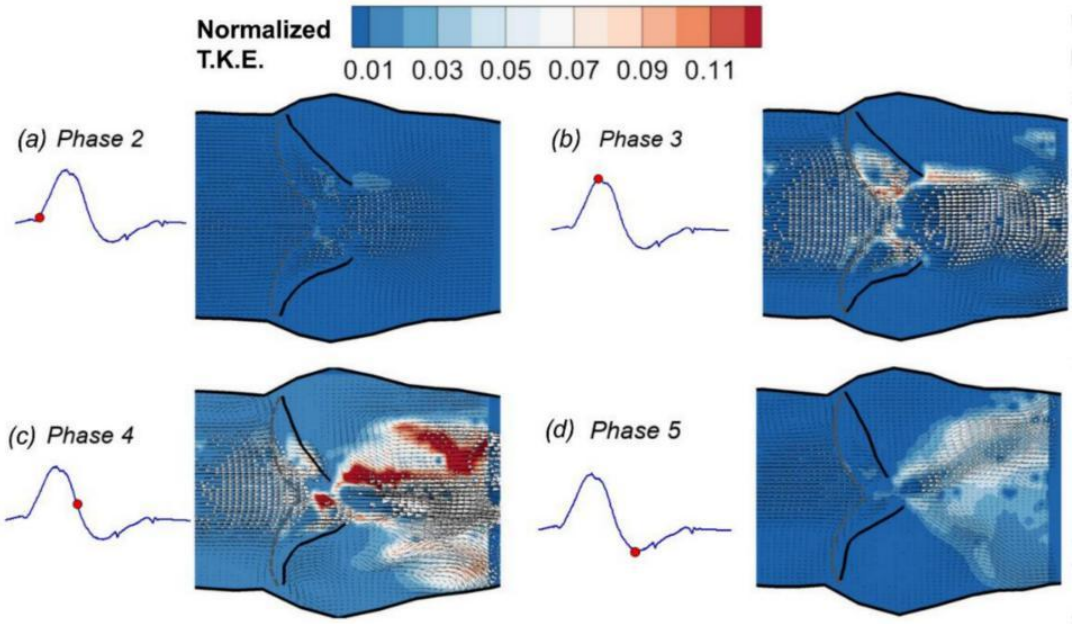

Figure 3.7. Normalized turbulence kinetic energy.

In sum, the PIV results clearly demonstrated the process of initiation and transportation of tip vortices, the development of the jet flow, as well as the dissipation of the jet at selected phases during a normal cardiac cycle. Strong vortices are also observed in the sinus region at this phase, which corresponds well with the results regarding the tension release of the compliant wall downstream from the valve [118]. The sinus vortices, which have been exclusively studied in previous in vitro experimental studies [160], are believed to contribute to the blood supply of the coronary arteries that originate from the sinus in the natural aortic root hemodynamics. Meanwhile, the highest jet velocity was found at the peak systole phase, with the highest TKE observed to occur during the deceleration phase of the pulsating flow (right after the peak

systole). This phenomenon corresponds well with the well-known instability growth in the deceleration phase of a pulsatile flow in a rigid pipe flow [157], and is also a prominent feature of human arterial blood flow [155], [156]. The present results suggest that the deceleration instability also occurs in the pulsatile flow within the complex aortic root wall boundaries.

In comparison to a PIV study by Saikrishnan et al. [78] in which native tissue valves with bicuspid and tricuspid morphologies were studied, the results show certain differences and similarities. On one hand, the orifice area of the current model is smaller than that measured for the tissue valves, resulting in a higher pressure gradient in the present study. This is potentially due to the stiffer material properties of the silicone material that was used in the present study. However, on the other hand, both trileaflet valve results show similar symmetric velocity, vorticity, and TKE distributions near the peak systolic phases. The magnitudes of TKE of the downstream jet flow at peak systole were also on the same order of magnitude (0.1 J/kg), despite the different experimental models and conditions that were used.

3.3.2. Structural Deformation in a Typical Cardiac Cycle

The deformation of the compliant model under the pulsatile flow was quantified by the variations of the tubular diameters and the leaflet orifice areas as shown in Figure 3.8. Figure 3.8a displays the changes of the normalized diameters (D/D_0, D_0 is the initial diameter at phase 1) during the cardiac cycle at the aortic annulus, aortic sinus, and sinotubular junction, respectively. The results show that the aortic annulus experiences the largest radial deformation during the course of the systole due to the direct exposure to the high upstream left ventricular pressure. In addition, it is interesting to note that while the maximum deformation of the aortic sinus and the sinotubular junction happened at phase 3 when the maximum jet flow occurs, the maximum deformation of the aortic annulus occurred at an earlier phase ahead of the peak systole. This

early area increase of the aortic annulus (base) was also found in previous clinical studies of aortic root dynamics [161]. Figure 3.8b shows the dynamic motion of the leaflet in terms of the changes of GOA, which was normalized by its maximum value in a cycle. It is clear that a significant increase of the orifice area also started to occur at an earlier phase before the peak systole. The opening area of the leaflets then increased as the systolic jet developed and decreased quickly past the peak systolic phase. It should be noted that the GOA is not completely zero during diastole due to the small gaps between the silicone leaflets and the limitation of the molding manufacturing process.

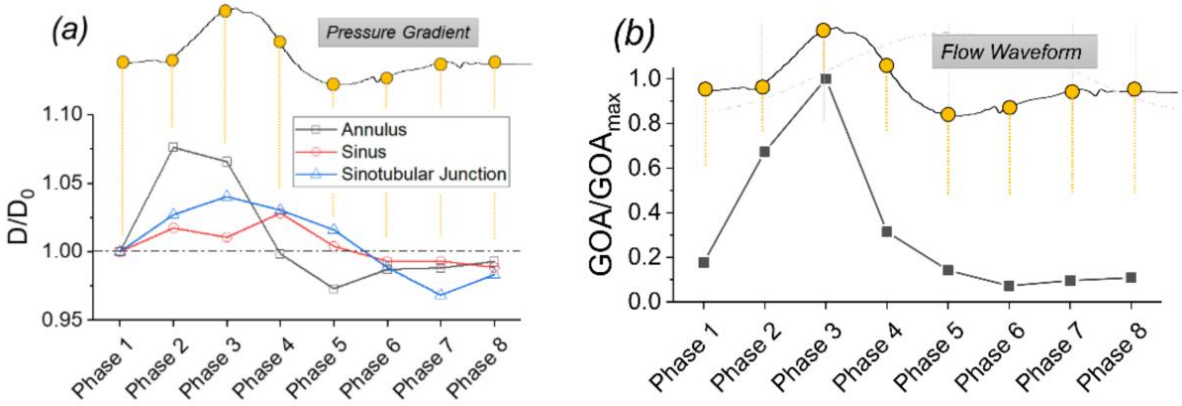

Figure 3.8. Deformation of the aortic root: (a) diameters at three sites; (b) the geometric orifice area of the valve during a cycle under the 4 L/min cardiac output.

3.3.3. Effects of Reduced Cardiac Output

Various cardiac diseases, such as myocardial infarction, hypertension, congenital heart disease, and arrhythmias, may lead to a reduction in cardiac outputs (CO). In this section, the results of the flow and structure responses of two reduced COs, i.e., 2 L/min and 1 L/min, were analyzed and compared with the results of the normal 4 L/min. Figure 3.9 summarizes the jet flow velocity both upstream and downstream of the aortic valve for all three cardiac outputs. The inlet and exit jet velocities were extracted from the PIV results along the centerline at the locations of the aortic annulus and the sinotubular junction, as illustrated in Figure 3.3a. It is

clear that when the CO was reduced from 4 L/min to 2 and 1 L/min, the peak flow velocity upstream of the valve decreased to a half and a quarter, respectively (Figure 3.9a). These linear trends were less obvious downstream of the valve due to the interaction of the leaflets (Figure 3.9b). Specifically, when the CO was reduced from 4 L/min to 2 L/min, the peak exit jet velocity decreased only by approximately 34%. A reduced CO also caused a faster dissipation of the downstream jet flow manifested by the sharp decrease of velocity right after the peak systole (phase 3 to 4).

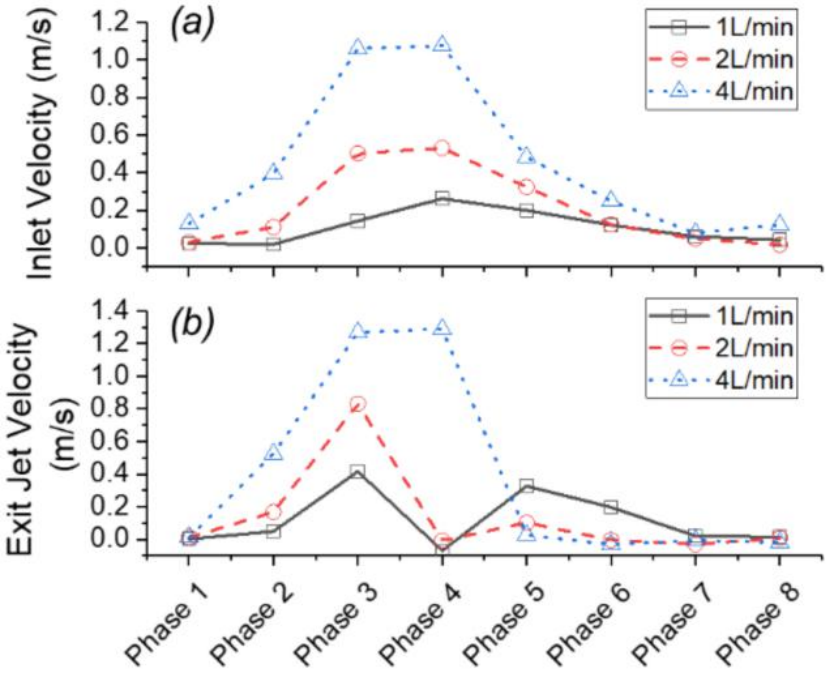

Figure 3.9. The inlet (a) and exit (b) jet centerline velocities at different phases under three cardiac outputs.

The effects of reduced CO on the diastolic turbulence have been analyzed using the ensemble 2D Reynolds shear stress (RSS), which is defined as:

$$RSS = -\rho \overline{u'v'} \tag{3.6}$$

where $\overline{u'}$ and $\overline{v'}$ represent the velocity fluctuations in x and y dimensions, respectively, and ρ is the density of the fluid. The RSS distributions are compared among the normal 4 L/min, and the

reduced CO, i.e., the 2 L/min and 1 L/min cases, at phases 3 (peak systole) and 4 (after peak) are shown in Figure 3.10 using the same color scales. At the peak systole phase (phase 3), the RSS magnitudes and distributions do not show apparent differences in reduced CO cases (Figure 3.10a). At phase 4, although the maximum values of RSS downstream of the valve are comparable among three CO cases, more scattered small-scale RSS distribution patterns are seen under reduced CO conditions (Figure 3.10b). Particularly, more small flow structures were observed near the center region downstream of the valve in the low CO cases. These results suggest that the turbulence is dissipated faster after the peak systolic phase under low CO conditions.

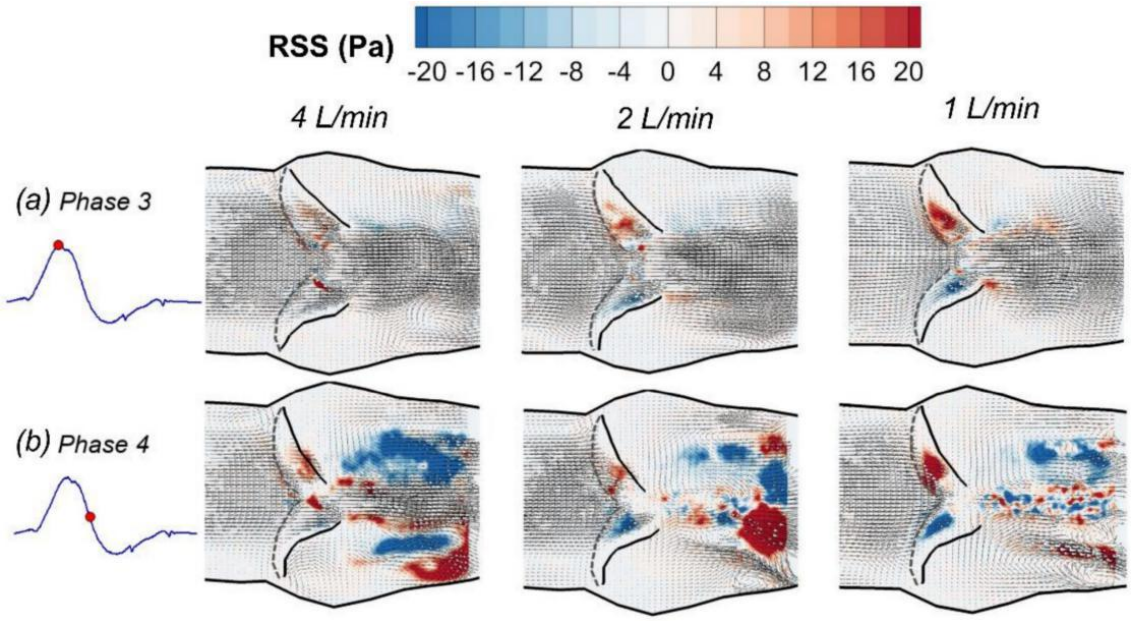

Figure 3.10. Reynolds shear stress under reduced cardiac outputs (a) peak systole (phase 3); (b) after peak systole (phase 4).

The deformation of the wall and the aortic valve leaflets is also different under reduced COs. Figure 3.11a shows the area strain (AS) at three different locations (aortic annulus, sinus, and sinotubular junction) and the corresponding peak systolic pressure under different cardiac outputs. It shows that the deformation at the aortic annulus is the most significant among the

three locations in all of the CO cases. As the CO is reduced from 4 L/min to 2 L/min and 1 L/min, the AS at the annulus decreased from 14.3 % to 11.3 % and 8.1 %, respectively. In comparison, the AS of the sinotubular junction downstream of the aortic valve is relatively small, and the AS at the aortic sinus is the least in all of the CO cases. However, the decreasing trends of the AS at these two sites are also apparent as the CO is reduced. These reductions are associated with the decreased peak systolic pressure when the CO is reduced.

Figure 3.11b displays the variation of geometric orifice area (GOA) over time for three different CO cases. As expected, the maximum GOA was significantly reduced as the cardiac output decreased. The maximum GOA at peak phase 3 was around 0.7 cm^2, 1.0 cm^2, and 1.6 cm^2 for cardiac outputs of 1 L/min, 2 L/min, and 4 L/min, respectively. It is also evident that the GOA started to increase at phase 2 in the 4 L/min case, while in low CO cases, the orifice area did not increase before the peak systole phase. These results imply that the blood transport efficiency would be significantly reduced under low CO conditions, since both the maximum orifice area and the effective time for pumping blood out of the ventricular chamber are decreased.

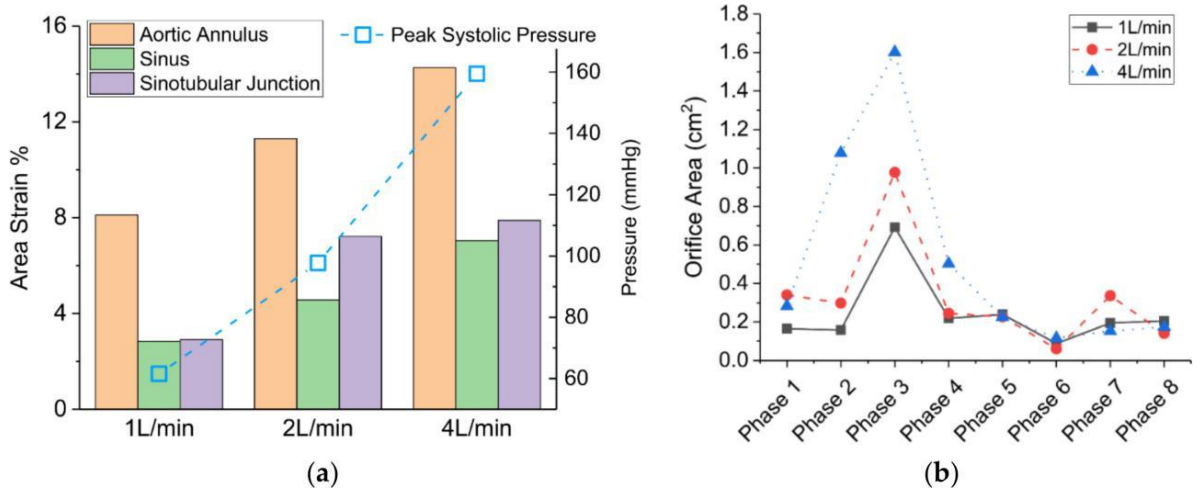

Figure 3.11. The structure deformation under reduced cardiac outputs. (a) The area strain; (b) geometric orifice area.

The structure deformation under different cardiac outputs were summarized and compared to some in vivo data in Table 3.2. It is clear that the maximum GOA of the silicone aortic valve under 4 L/min cardiac output was reasonably close to the in vivo value reported in Clavel et al. [162], in which the GOA of a transcatheter Edwards SAPIEN valve (Edwards Lifesciences, Irvine, California, USA) was evaluated. The area strain at the sinotubular junction under 4 L/min was found to be smaller, but close to that of a natural aortic valve from a magnetic resonance imaging (MRI) study [159]. These comparisons suggest that some major pulsatile flow characteristics are replicated in the present in vitro experiments. However, it should be noted that the current silicone model does not have the same stiffness and other viscoelastic properties of the natural myocardium tissue. The structure deformation results that were observed in the present experiments could not be directly translated into an in vivo biological setting, where the material properties and the extravascular environment are inherently different.

Table 3.2. Area strain (*AS*) and maximum geometric orifice area (*GOA*) comparisons.

Cardiac Output	1 L/min	2 L/min	4 L/min	Effective orifice area of a Bioprosthetic Aortic Valve [162]	Area Strain (Mean) [159]
GOA (cm^2)	0.7	1.0	1.6	1.37–1.9	-
AS (%) at Aortic Annulus	8.1	11.3	14.3	-	-
AS (%) at Aortic Sinus	2.8	4.6	7.0	-	-
AS (%) at Sinotubular Junction	2.9	7.2	7.9	-	8.1

3.4. Conclusions

An in vitro experimental study has been conducted to investigate the pulsatile flow characteristics in an intact silicone aortic root model. Particularly, the turbulent flow characteristics and structural deformation in response to varied COs were examined. The

pulsatile flow was generated using a programmable piston pump in a closed-loop cardiovascular flow simulator. A phase-locked PIV system and high-frequency pressure sensors were used to obtain the quantitative flow field and pressure time series data. The key results can be summarized as follows:

1) The flow field characteristics during a typical cardiac cycle have been revealed using phase-locked PIV. Both the jet flow patterns and the turbulence kinetic energy vary significantly at different phases with changes of the pressure gradient. High *TKE* was observed after the peak systole when flow started to decelerate.

2) The pulsatile flow caused noticeable structural deformations under normal cardiac output. The largest circumferential deformation was found at the aortic annulus upstream of the aortic valve at a phase prior to the peak systole. The significant increase of the valve orifice area was also found at a phase prior to the peak systole under the baseline 4 L/min condition.

3) Cardiac output (CO) plays an important role in the hemodynamics and structural responses of the aortic valve root. A decrease of CO from 4 L/min to 2 L/min and 1 L/min resulted in a reduced exit jet flow velocity and a deceased turbulence downstream. Reduced CO also contributed to a decrease in circumferential deformation, a decrease in orifice area, and a shortened valve opening period.

Overall, this study shows a preliminary effort to quantitatively investigate the fluid dynamics of an intact aortic root model under varied input flow conditions. The results demonstrate that an in vitro pulsatile flow system is capable of capturing some of the most prominent flow characteristics within a flexible aortic root, while providing better controllability and spatial resolution that complements the clinical imaging research. The results could provide validation benchmarks for future patient-specific CFD and FSI simulations.

4. EXPERIMENTAL ANALYSIS OF PULSATILE EXPERIMENTAL ANALYSIS OF PULSATILE FLOW CHARACTERISTICS IN PROSTHETIC AORTIC VALVE MODELS WITH STENOSIS[2]

4.1. Introduction

Clinical research suggests that about 5 million people were diagnosed with valvular heart diseases each year in the United States, such as aortic calcification, stenosis and regurgitation [10]. Among them, aortic stenosis (AS) is the most prevalent condition and leads to high risk of mortality. Thus, in this chapter, we would like to investigate the flow characteristics inside stenotic aortic valve models. Normally, AS is predisposed by age-related calcification, congenital aortic diseases, rheumatic valve diseases, etc. [12], [163] and is considered as the potential cause of some other cardiovascular complications [11]. As a progressive disease, AS is very difficult to be predicted due to the fact that it is an asymptomatic disease at its early stage (mild and moderate stage) [164] and the main predictors change with time irregularly given the influence of many factors [165]. Numerous clinical studies have been performed in attempts to clearly understand the hemodynamic characteristics for AS severity assessments and to evaluate the potential benefits provided by aortic valve replacement surgery or minimally invasive transcatheter aortic valve replacement (TAVR) [165]-[167].

Nowadays, two types of artificial valves dominate the market - mechanical and bio-prosthetic valves. While mechanical valves provide superior material strengths and lifelong durability, they also form increased wall shear stress (WSS) and turbulence due to the non-physiological interactions with the pulsatile blood flow [169], [170]. These alterations in

[2] The material in this chapter is adapted from two publications - R. Zhang and Y. Zhang, "Effects of heart rate on the pulsatile flow characteristics of a stenotic aortic valve model: an in vitro experimental study," Journal of Fluids Engineering, vol. 142, no. 10, Oct., pp. 101205, 2020. https://doi.org/10.1115/1.4047410, and Zhang, Ruihang, and Zhang, Yan. "Experimental analysis of pulsatile flow characteristics in prosthetic aortic valve models with stenosis," Medical Engineering & Physics, vol. 79, May, pp. 10-18, 2020. https://doi.org/10.1016/j.medengphy.2020.03.004.

hemodynamics increase the risks of platelet activation and even hemolysis [17]-[19]. In contrast, bio-prosthetic valves are normally fabricated from porcine or bovine valve tissues with the natural three-cusp configurations, which the anatomy is close to native valve and the risks of thrombosis and hemolysis are low [21], [22]. However, bio-prostheses suffer from material deteriorations and their durability is often much shorter than the mechanical valves [24]. A deeper understanding of valve hemodynamics is of critical importance for the clinical assessment, deployment, and management of aortic valve prostheses. However, how flow behaviors across stenotic valves would change under varied physiological conditions have not yet been extensively studied previously. Recently, interdisciplinary biomedical engineering research has made significant contributions to the fundamental hemodynamics and fluid-structure interactions of artificial heart valves. In the past decades, in vitro experimental fluid dynamics studies have made significant contributions to the understanding of aortic valve hemodynamics related to diseases and replacement valves [51], [67], [111], [146]. In particular, PIV has been employed in many of these experimental studies to clearly quantify the flow characteristics of aortic valves [67], [68]. PIV has also been used to compare the hemodynamics of congenital bicuspid and tricuspid aortic valve models [78] and to provide validations of the computational results of aortic valve disease hemodynamics [51], [53].

In this chapter, we applied the phase-locked PIV and high-frequency pressure measurements to study the pulsatile flow through polymeric aortic valve models with stenosis under varied physiological conditions. The first valve model was fabricated using polydimethylsiloxane (PDMS) by molding the leaflets and the aortic root wall together as a whole. The second model was constructed by installing a stented fabric-reinforced silicone valve into the PDMS aortic root. Due to the different material selection, a different degree of stenosis

was achieved as evidenced by pressure measurement data. High frequency pressure sensors were used to measure the pressure fluctuations across the stenotic valve models. The phase-locked ensemble-average flow fields and derived unsteady flow information were analyzed and discussed to reveal the impacts of stenosis on the flow inside the aortic root at 75 beats per minute (bpm) as a baseline. In addition, the flow characteristics of second constructed valve model were also investigated using PIV method under varied heart rates (50, 75 and 100 bpm).

4.2. Experimental Methods

4.2.1. Polymeric Aortic Valve Models

Two polymeric aortic valves representing different stenotic conditions were tested in this study. Figure 4.1(A-C) shows the first intact PDMS model (Model #1) which was fabricated via molding process based on a physiologically-realistic aortic root geometry with a tricuspid valve (Figure 4.1A, BDC laboratories). The model has three leaflets with an average thickness of about 1 mm, located within the three bulges of the sinus of Valsalva (i.e., aortic sinus). The inlet and exit coupling tube sections are both 1 inch (25.4 mm) in diameter. The PDMS (RI = 1.43) is soft, elastic, and easily customizable material, making it an excellent candidate for fabrications of biological models and phantoms. PDMS also has perfect optic property that is suitable for in vitro PIV testing. Figure 4.1B shows that the optical distortion was eliminated by using the RI matching fluid. The picture of the PDMS valve without pressure gradient is shown in Figure 4.1C. To understand the viscoelasticity of the material, dynamical mechanical analysis (DMA Q800) was performed on a rectangular isotropic PDMS model specimen with dimensions of 17.3 × 4.3 × 2.7 mm (length × width × thickness) under ambient temperature. A drive force of 0.0136 N (0.0869 % strain) was applied on the specimen at a low frequency of 1 Hz. Data showed that the sample has a storage modulus of 1.3 MPa, a loss modulus of 0.086 MPa, and a low modulus

ratio (damping) tan δ = 0.0011, suggesting that the viscous energy dissipation was minimal and the PDMS deformation was highly elastic.

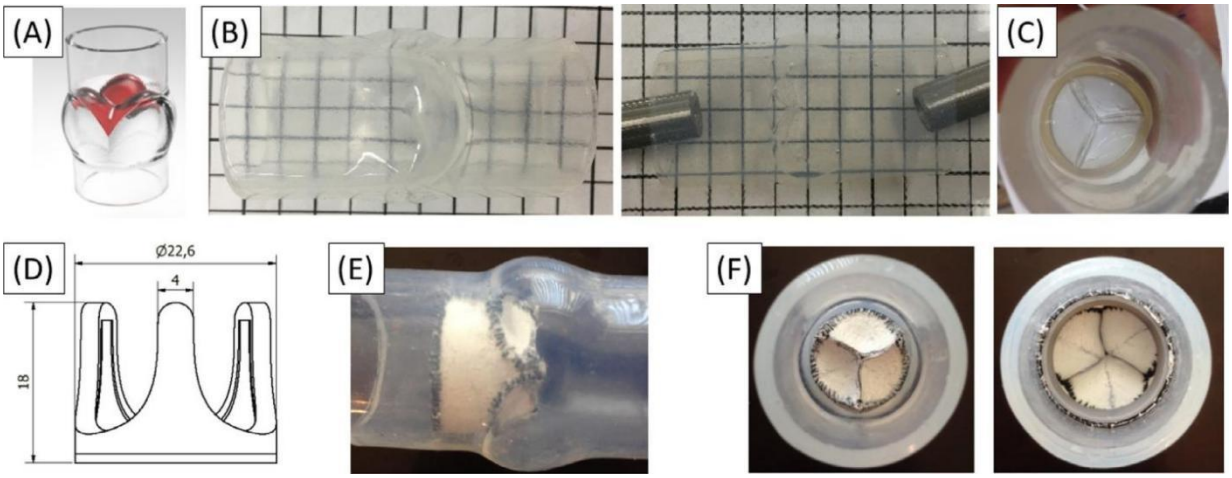

Figure 4.1. Two polymeric aortic valve model: model #1 (A–C) and model #2 (D-F). (A) Model #1: the molded PDMS aortic root with three leaflets; (B) Model #1 with optical distortion and after refractive index matching; (C) the internal view of the molded valve leaflets of Model #1; (D) the 3-D printed stent base for Model #2; (E) Model #2 implanted in the same aortic root model; (F) internal views of the implanted stented valve of Model #2.

Figure 4.1 (D-F) shows the second polymeric valve model (Model #2) to be considered. This model used exactly the same PDMS aortic root model, while the leaflets were replaced by a stented silicone valve whose leaflets were stiffened. The stent geometry and dimensions (in mm) is presented in Figure 4.1D. The valve leaflets were created using a composite of silicone and cotton fabrics via a molding process. The three-dimensional (3D) leaflet mold was 3D-printed based on a smoothed geometry of a natural aortic valve similar to that of the Model #1. The fabric, used to increase the valve stiffness and tensile strength, was impregnated with the silicone solution and then carefully laid on the center mold for the curing process. After curing, the root of the valve was fixed to a polystyrene stent ring to hold its shape. The average thickness of the valve was about 0.8 mm. Tensile testing was performed to determine the properties of the fabric-enhanced silicone valve material. Rectangular specimen with a size of 50 mm by 5 mm were cut and subjected to testing using a mechanical tensile tester at a rate of 12.5 mm per minute. Data

showed that the valve leaflet has a Young's modulus of 70 MPa, a peak strain at break of around 26 % at a peak stress of 5 MPa, suggesting a much stronger and stiffer material property than that of the pure PDMS leaflet. Additionally, for Model #1 and Model #2, the hemodynamic characteristics, i.e. the aortic valve area (AVA), of the aortic valve were evaluated via the measured pressure gradient data using Gorlin equation. Based on the results, the AVA of the artificial valve Model #1 and Model #2 is 1.65 ± 0.04 cm^2 and 0.74 ± 0.01 cm^2, respectively, indicating that Model #1 is a moderate aortic stenosis and Model #2 is severe aortic stenosis according to the ACC/AHA guidelines [171].

4.2.2. The Cardiovascular Flow Simulator

A closed-loop cardiovascular flow simulator, as illustrated in Figure 4.2A, was used to provide flow conditions for this experiment. A programmable piston pump (PD-1100, BDC Laboratories) with a left ventricular diastolic pressure module was selected in this loop. Compliance and resistance units were installed downstream of the test model to tune pressure flow conditions before a fluid tank (collect return flow). High frequency pressure sensors (response 5 kHz, BDC-PT, BDC lab) were installed across the test section to measure the pressure. High-frequency pressure sensors (5 kHz) with a LabView DAQ module (Natinal Instruments) have been used to record the pressure waveform at multiple locations. More details regarding the simulator are to be found elsewhere [172].

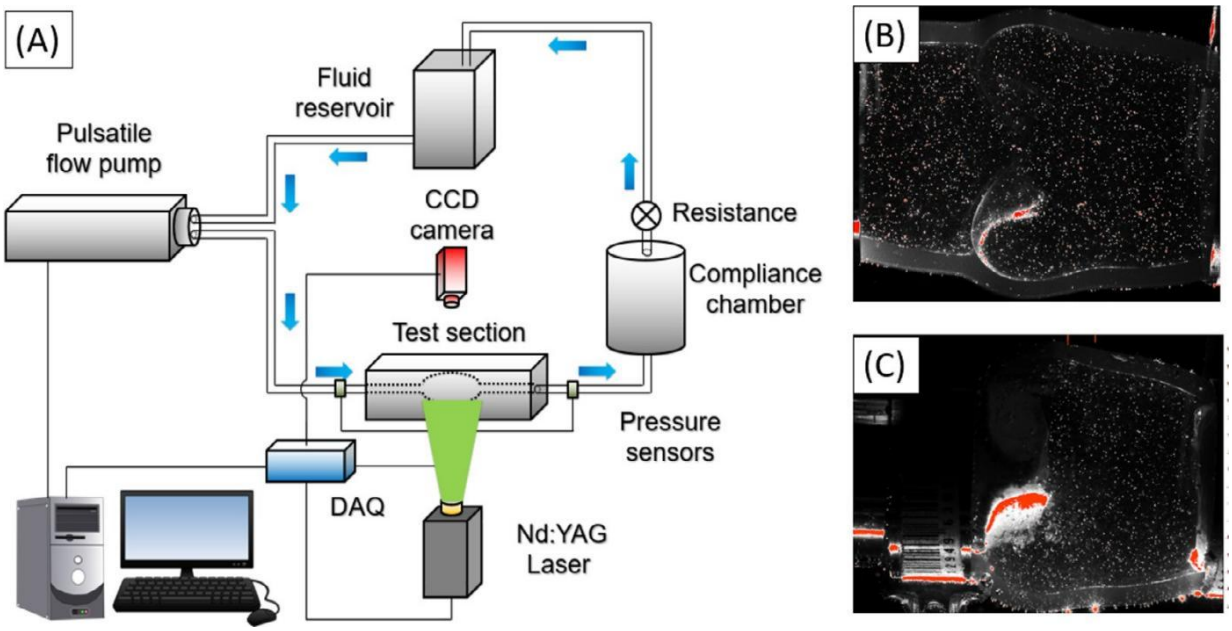

Figure 4.2. The schematic of the experimental setup: (A) The cardiovascular flow simulator; (B) raw PIV images from the two models.

4.2.3. Particle Image Velocimetry (PIV)

For the phase-locked PIV system, a double-pulsed Nd:YAG laser (NewWave Gemini 200, 100 mJ, 532 nm) was used for illumination. A set of lenses and a 2M-pixel CCD camera were employed in this experiment. The lasers and camera were synchronized by a delay generator (BNC Model 577, Berkeley Nucleonic Corp.), which was externally triggered by a digital signal from the pulsatile pump. The delay to the trigger signals was then controlled specifically for each test case to obtain phase shifts. The uncertainty of the synchronizing (based on the rise time of TTL signal) was less than 3 ns. Cross-correlation technique was used to compute the instantaneous PIV velocity vectors, which connected continuous frames of patterns of images with multi-pass interrogation process from window size of 32 × 32 to 16 × 16 pixels. A 50 % effective overlap was selected to fulfill the Nyquist criterion. For post-processing, time-averaged parameters were achieved from a cinema sequence of 300 frames of instantaneous velocity fields per condition. The gathered data was post-processed using DaVis software (LaVision Inc.). For

the uncertainty of PIV measurements, the bias or accuracy error mainly comes from the standard cross-correlation analysis of the raw particle images. Although the bias limit of the PIV measurements was not studied in this paper, a good estimate of a standard PIV cross-correlations is within 5 % based on the detailed study [26]. The precision limit of the current phase-locked PIV average velocity is very small and estimated to be ±0.2 % (confidence interval of 95 %), based on the calculation of 300 velocity data samples extracted at a low turbulence flow region (standard deviation less than 2 % of the mean velocity). Thus, the maximum uncertainty of the PIV is estimated to be less than 5 % of the measured data.

A mixture of water-glycerin (40 % and 60 % by volume, respectively) was also used as the working fluid (density ρ = 1,160 kg/m^3 and a dynamic viscosity μ = 0.012 Pa·s) in this study to match the RI to minimize the optical distortion. Figure 4.3 shows the visual effects of the silicone model before and after RI matching. It should be noted that the non-Newtonian fluid property of blood due to the existence of red blood cells were not considered in this study. The working fluid was seeded with hollow glass microspheres (10 μm in diameter) with a seeding density of 0.1 ppm [51], [116]. The density of the particles is very close to water and the resultant Stokes number is much less than 1, making them perfect seeders for water-based PIV measurements. The raw images with seeding particles obtained for Model #1 and #2 are shown in Figure 4.2 (B-C), respectively.

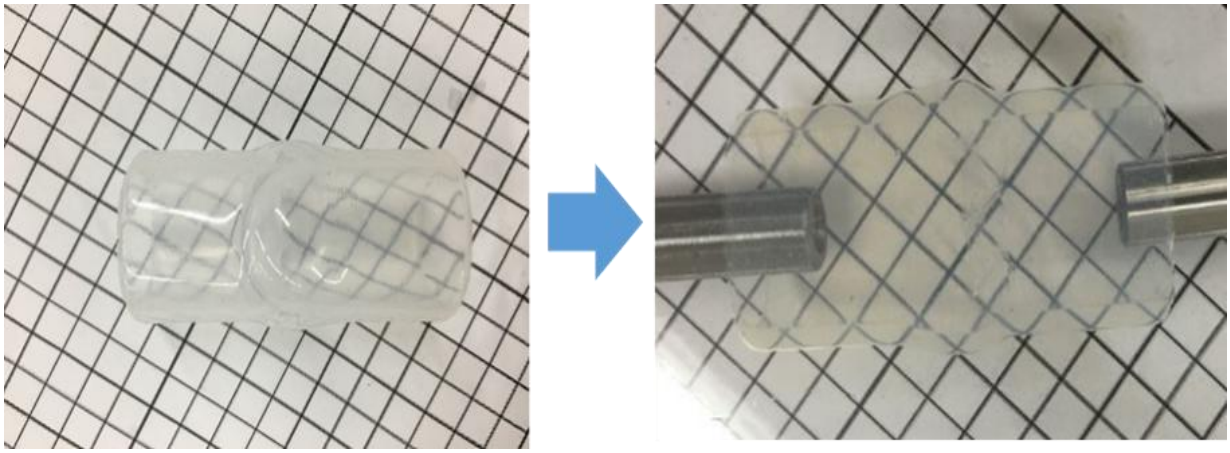

Figure 4.3. The refractive index matching of silicone aortic root model.

4.2.4. Experimental Conditions

A systole-to-diastole ratio (S/D ratio) of 40 % was selected according to the normal physiological range based on clinical research [173], [174], and the total CO was fixed at 4 L/min. Reynolds number (Re) and Womersley number (Wo) of the test conditions were calculated at the peak systolic flow conditions using the equation as follows (Eq. 4.1 - 4.2):

$$\mathrm{Re} = \rho d_a u_a / \mu \tag{4.1}$$

$$\mathrm{Wo} = r_a \sqrt{\omega \rho / \mu} \tag{4.2}$$

where d_a and r_a indicate the inner diameter (25 mm) and radius of aortic valve; u_a is the maximum jet flow velocity; ρ, μ, and ω are the density, dynamic viscosity and angular frequency of pulsatile flow, respectively. The Re and Wo in the these experiments both fall within the normal range of human physiology [173], [175]. For the comparison of two stenotic models, the heart rate was 75 bpm hear rate was selected as the baseline. Thus, the corresponding peak Reynolds number (Re) is 2,500 – 3,300 and the Womersley number (α) is 16.1. For the flow characteristics study of stenotic Model #2, three different heart rates were chosen: 50, 75, and 100 bpm under the same CO, respectively.

4.3. Results

4.3.1. Pressure Waveforms

The 2-second segments of pressure waveforms measured upstream (left ventricular, i.e. LV, pressure, blue lines) and downstream (aortic pressure, red lines) of the two valve models are displayed in Figure 4.4 (A-B), respectively. Meanwhile, the pressure gradients across the model, i.e. LV pressure minus the aortic pressure, are shown as the black lines with shaded areas. The results demonstrate that under the same flow boundary conditions, the general patterns of pressure waveforms for the two models are quite similar. The waveforms repeat with a period of 0.8 s due to the 75 bpm heartbeat setting. Driven by the 40 % systole-to-diastole ratio motion of the pump, the systolic period of the aortic pressure gradients were both 0.32 s. Note that the actual ejection time manifested by the positive pressure gradients are different for the two models due to the different leaflet structural responses to the pump pressure.

Further examinations of the waveforms reveal some different pressure loading conditions for the two valve models under the same boundary conditions. First, the LV pressure upstream of the valve in Model #2 was higher than that of Model #1 in the entire cycle, which also resulted in a greater peak pressure gradient during systole. Second, the pressure gradient of Model #1 becomes negative briefly towards the end of systole (0.4 – 0.5 s in Figure 4.4A), while that of Model #2 remains positive as shown by the pressure plateaus during the same time periods. These differences are potentially due to the greater resistance of the stiffer valve leaflets (more severe stenosis) of Model #2 and their dynamic responses to the varying pump chamber pressure.

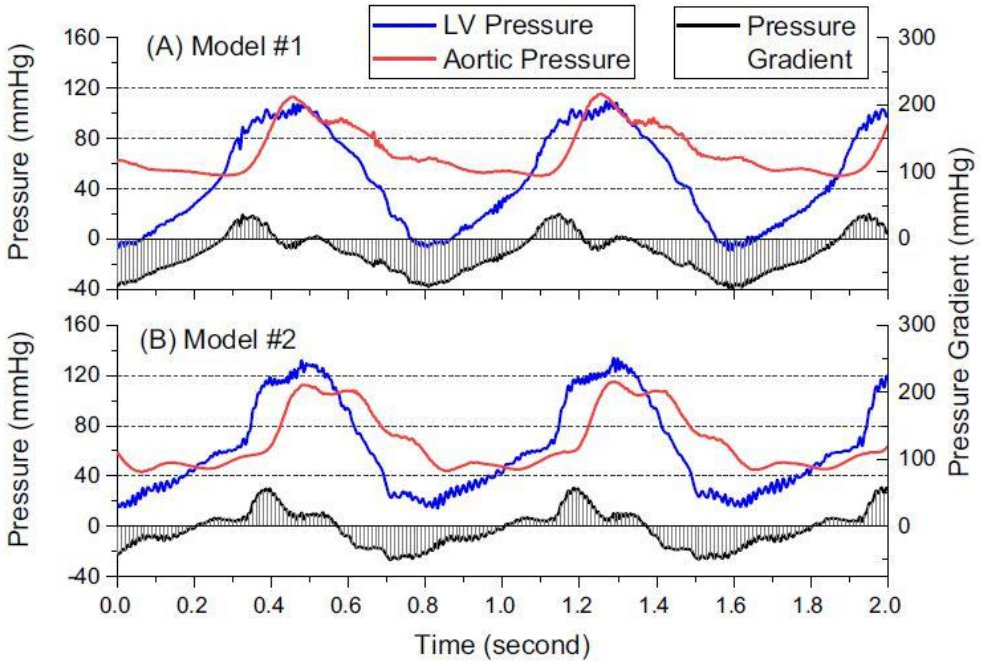

Figure 4.4. Pressure waveforms and pressure gradients for the two valve models at 75 bpm.

Table 4.1 lists the key parameters from the pressure waveforms related to the prosthetic stenosis at 75 bpm calculated from the 15-second time-serial pressure data (18.75 cycles), each consisting of 75,000 data points with a sampling frequency of 5 kHz. The uncertainty was estimated based on the standard deviations of the cycle-to-cycle data of the 18 cycles collected. The results clearly show that compared to the stented stiffened valve (Model #2), Model #1 resulted in smaller mean and peak pressure gradients. The systolic ejection time of Model #1, estimated by the positive pressure gradient duration, was significantly shorter than that of Model #2. The prolonged ejection period of the more severe stenosis case is consistent with the previous clinical research findings [176].

Table 4.1. A summary of key parameters from pressure waveform measurements at 75 bpm.

	Mean Pressure [mmHg]	Peak Gradient [mmHg]	Actual Ejection Time (ET) [seconds]
Model #1	17.4±0.8	37.7±1.8	0.263±0.005
Model #2	19.7±0.2	53.1±1.4	0.365±0.008

To understand how the pressure gradient varies across the stenotic Model #2 under different heart rates, the pressure curves of 50 – 100 bpm are shown and compared in Figure 4.5. The blue dashed line and the red solid line demonstrate the left ventricular pressure and aortic pressure, respectively, within a cardiac cycle, such that the pressure gradient (LV pressure – aortic pressure) can be compared for the three heartbeat conditions. To facilitate the comparison, the actual cardiac time (t) is normalized by the cycle durations of each heart rate (T), i.e. 1.2 s, 0.8 s, and 0.6 s for 50, 75, and 100 bpm, respectively, and the t/T = 0.0 (peak systole) of each case are aligned. Each normalized time step, i.e. t/T, is referred to as a cardiac phase in this study. The results show that the peak pressure gradient at t/T = 0.0 increased significantly from 37.9 mmHg to 53.1 mmHg and 63.8 mmHg for heart rates of 50 bpm, 75 bpm, and 100 bpm, respectively. This might be caused by the increased acceleration of flow of each cycle at the faster heart rate condition. In the meantime, the mean pressure gradient (represented by the area between the waveforms) does not vary significantly. The peak-to-peak pressure gradient, which is determined by calculating the difference of the peak pressure of the LV and the peak pressure of the aortic flow during a cycle, decreases as the heart rate increases. These pressure gradient data are listed in Table 4.2. The uncertainties of the pressure gradient in the table are estimated based on the maximum pressure reading multiplying by the maximum uncertainty of the pressure sensor measurement. These data suggest different pressure gradient indices that have been used for clinical stenosis evaluations vary significantly with the heart rate under the same cardiac output.

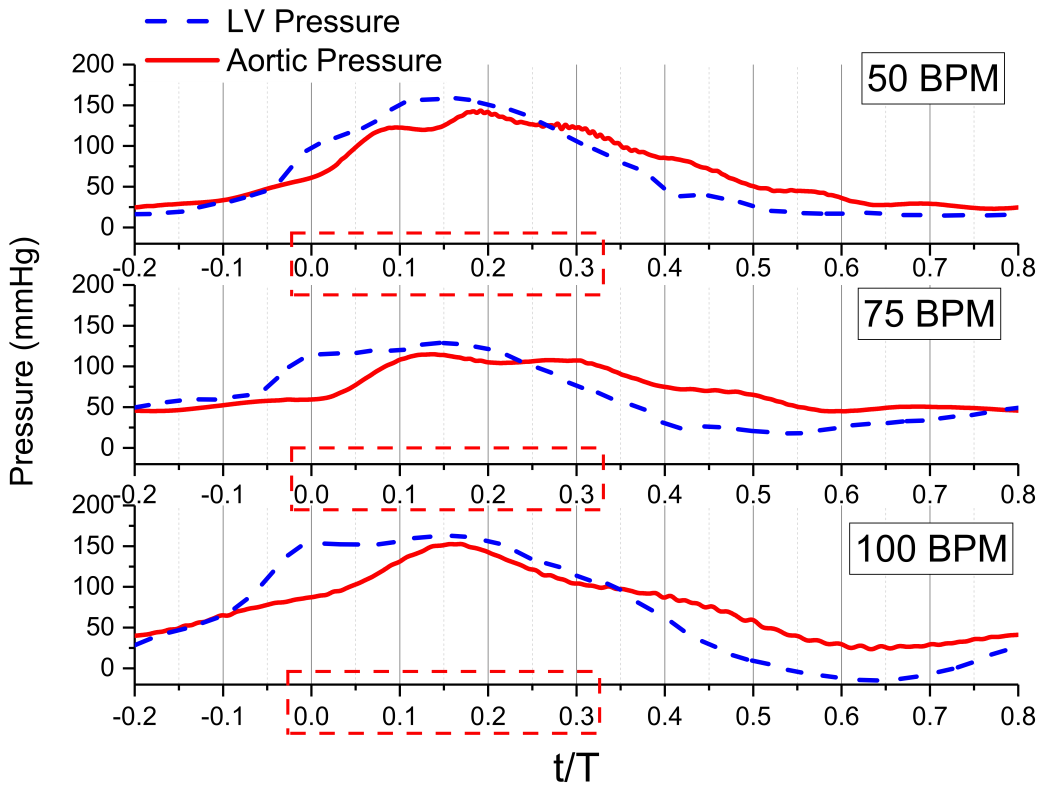

Figure 4.5. Pressure waveforms across Model #2 under different heart rates (50bpm, 75bpm and 100bpm), shown with nondimensionalized time.

Table 4.2. Summary of pressure gradients for stenotic Model #2.

HR [bpm]	Stroke volume [ml]	Max ΔP [mmHg]	Mean ΔP [mmHg]	Peak to Peak ΔP [mmHg]
50	80	37.9±1.9	21.8±0.4	28.5±3.4
75	53	53.1±1.4	19.7±0.2	25.1±2.8
100	40	63.8±3.0	23.4±0.5	17.0±3.4

4.3.2. Instantaneous and Averaged Flow Fields for Two Models at 75 bpm

Figure 4.6 shows the instantaneous flow fields and out-of-plane vorticity distributions of two models at four different flow phases. The timing of each locked phase was re-defined by setting the peak systole phase as the reference time. Specifically, the early systolic phase (10 % of the cycle) was defined as t/ T = −1/10; the peak systole phase is defined as t/ T = 0 (20 % of the cycle) when the cyclic maximum pressure gradient occurred; the late systolic phases were

defined as t/ T =+ 1/10 and + 2/10 (30 % and 40 % of the cycle, respectively). The magnitude of the z-vorticity is calculated by

$$\omega_z = \frac{\partial v}{\partial x} - \frac{\partial u}{\partial y} \tag{4.3}$$

Note that since Model #1 is entirely transparent, we were able to mark down the boundaries of the valve leaflets qualitatively from the raw PIV images for different phases. These boundaries are shown in black dashed lines in Figure 4.6 (A-D). The stented structure of Model #2 covered the flow fields upstream of the valve and therefore is not shown in Figure 4.6 (E-H).

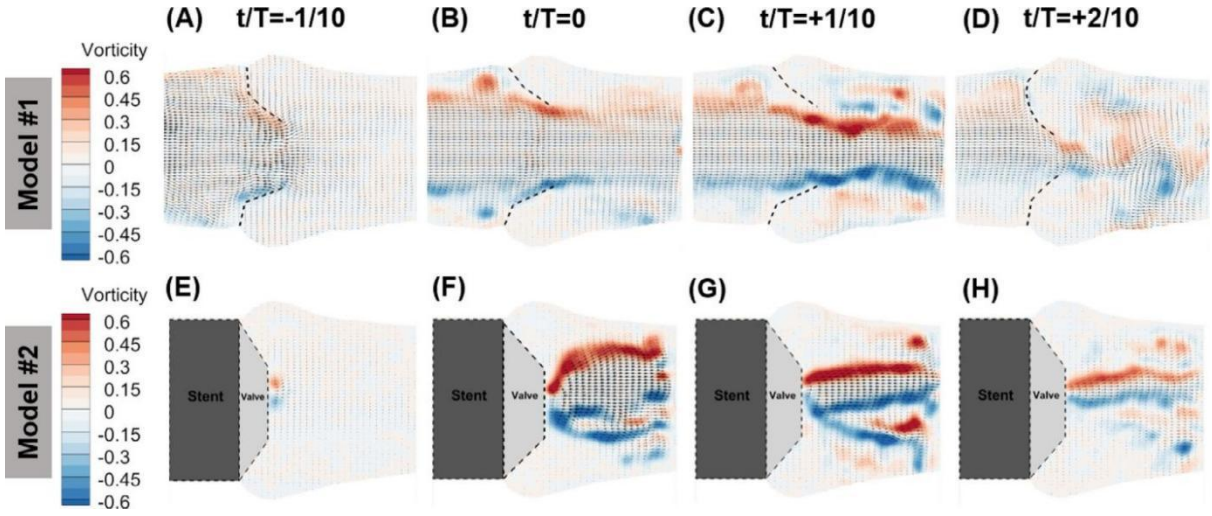

Figure 4.6. Instantaneous vorticity distribution at selected phases.

The instantaneous vorticity field demonstrates the initiation, growth, and dissipation of the aortic jet during the systolic periods of the two models. At the early systole phase (t/ T = −1/10), the opening of Model #2 was significantly smaller than that of Model #1, evidenced by the smaller distance of the pair of vortices at the jet exit (Figure 4.6A & E). At peak systole (t/ T = 0), the flow passed through Model #1 valve more smoothly and had the narrowest jet location (vena contracta) slightly downstream of the jet exit. However, Model #2 resulted in a rapid expansion of jet flow immediately downstream of the narrow orifice, which also caused

significantly higher vorticity in the free shear layer of the jet. At the phase past peak systole (t/ T =+ 1/10), it is clear that the jet started to narrow and the vorticity increased for Model #1 due to the decreasing pressure gradient and closing leaflets. Near the end of systole (t/ T =+ 2/10), the jet through Model #1 dissipated faster than that of Model #2, as shown by the weaker vorticity in Figure 4.6D and H.

The horizontal velocity U calculated from an ensemble average of 300 phase-locked instantaneous results is displayed in Figure 4.7. At t/ T = −1/10, the flow was at early-systole and a maximum jet velocity of only 0.3 m/s was found near the orifice of both valves. At t/ T = 0, a significantly greater jet velocity was seen in Model #2 than that in Model #1, as shown in the comparison of Figure 4.7 (B & F). After the peak systole, the jet velocity through Model #1 valve continued to increase, while the jet velocity of Model #2 did not change substantially, as shown in Figure 4.7 (C & G). A decrease in the width of the jet can be seen in both models as a result of decreased pressure gradient and closing leaflets. Towards the end of systole at t/ T =+ 2/10, both models show decreased jet velocities. However, it is obvious that the maximum velocity of Model #2 was still considerably higher than that of Model #1 at this phase, indicating a longer ejection period, corresponding well to findings from the previous pressure gradient results. It should be noted that the eccentricity of the jet was also increased by the severe stenosis in Model #2, as shown in Figure 4.7 (E-H), which was found less significant in Model #1.

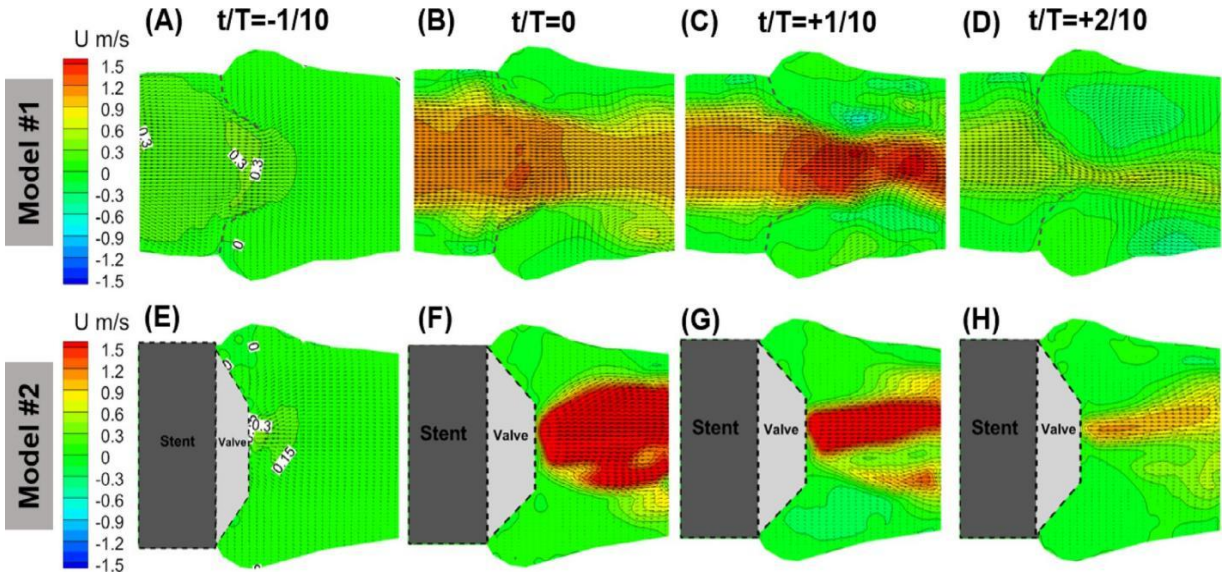

Figure 4.7. Ensemble averaged horizontal velocity at selected phases.

Figure 4.8 displays the velocity profiles of the two models extracted from the PIV data at two locations, i.e. the jet exit (set as x = 0 mm) and 15 mm downstream of the exit, which are also compared with a third scenario for which the valve leaflets were removed from Model #2 (with stent installed only). The purpose of using the "no-valve" scenario as a baseline is to identify jet flow variations induced by the valve dynamics versus the natural variations of the pulsatile flow. While there was no obvious difference in the results of pre-systolic phase (Figure 4.8A), Figure 4.8B suggests that the severe stenosis in Model #2 caused an around 2-fold increase in the peak jet velocity at peak systole (Figure 4.8B). In contrast, Model #1 did not increase the peak jet velocity significantly at both orifice and downstream locations. Meanwhile, the width of the jet at the orifice location (x = 0 mm) was strongly associated with the severity of the stenosis, while the jet width downstream did not show significant differences. At t/ T =+ 1/10, the peak jet velocity of Model #1 increased, while that of Model #2 slightly decreased from the previous phase, which quantitatively demonstrates the trends in Figure 4.7. However, Model #2 still had a higher peak jet velocity than Model #1 at this phase. At t/ T =+ 2/10, the jet of Model

#1 decreased faster than that of the no-valve case, while the jet of Model #2 was relatively stronger than the other two cases.

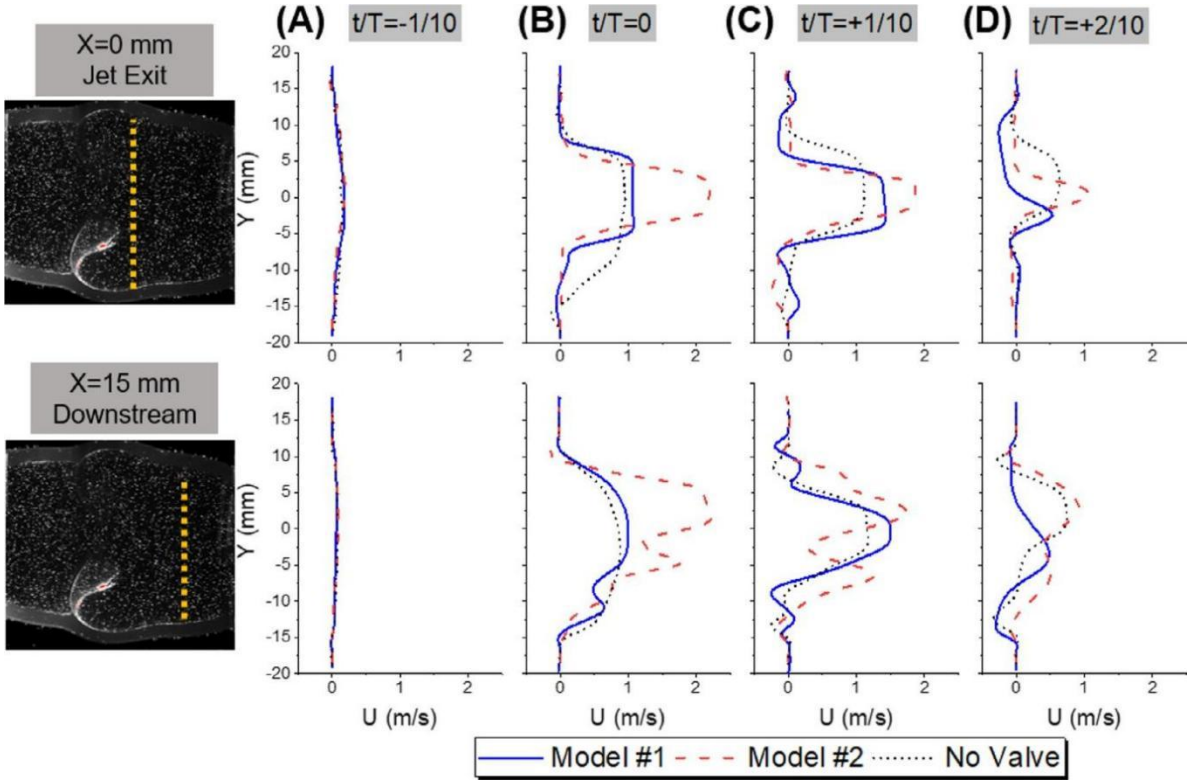

Figure 4.8. Velocity profiles extracted at the orifice (x = 0 mm) and 15 mm downstream, compared with the valve removed case.

4.3.3. Turbulent Characteristics for Two Models at 75 bpm

The turbulent characteristics of the systolic flow were analyzed by calculating the ensemble Reynolds shear stress (RSS) and turbulent kinetic energy (TKE) from the instantaneous results. The 2D normalized RSS and TKE are defined as

$$RSS = -\overline{u'v'}/U_{avg}^2 \tag{4.4}$$

$$TKE = 0.5(\overline{u'^2} + \overline{v'^2})/U_{avg}^2 \tag{4.5}$$

where u' and v' are velocity fluctuation components in horizontal and vertical directions, respectively, and U_{avg} is the reference velocity calculated by averaging the same cardiac output

flow with the same cross-sectional area for both models. Figure 4.9 (A-B) shows that the RSS of Model #1 remained very low at the early (t/ T = −1/10) and peak systole (t/ T = 0). Past the peak systole (Figure 4.9 C-D), high RSS regions were created at the interface of the free jet, indicating stronger instability was generated due to the fluid-structure interaction during closure phases of the valve. In contrast, Figure 4.9 (E-F) indicates that significantly higher RSS was generated from pre-systole to peak-systole across the stiffened valve of Model #2, particularly near the valve orifices. Much higher RSS regions were also generated downstream of the valve at t/ T =+ 1/10 (Figure 4.9G). However, at t/ T =+ 2/10, the high RSS region downstream in Model #2 dissipated faster compared with that of Model #1.

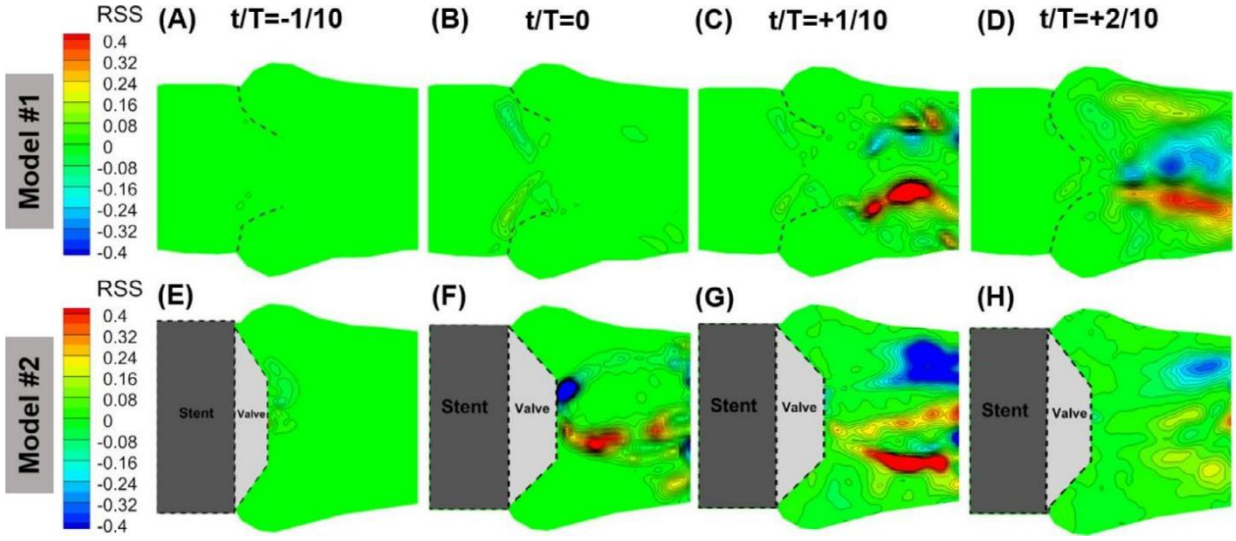

Figure 4.9. Normalized Reynolds shear stress distribution.

The TKE profiles of the two models are quantitatively compared in Figure 4.10, which also includes the “no-valve” baseline case. The normalized TKE was extracted at the valve orifice (x = 0 mm) and 15 mm downstream of the orifice. The results suggest that Model #2 generated significantly higher turbulence than Model #1 at both locations at nearly all phases during systole. The peak TKE found in Model #2 was almost 3-fold as that found in Model #1. At the peak systole (t/ T = 0), the TKE of Model #1 was almost negligible and even smaller than

the no-valve case (Figure 4.10B), whose TKE near the orifice were potentially contributed by the stent base itself. In contrast, the TKE of Model #2 was significantly larger near the orifice at the peak systole and were found transported downstream at phase t/ T =+ 1/10 (Figure 4.10C). At t/ T =+ 2/10, the TKE of Model #2 decreased, while that of the Model #1 increased from the previous phase, which indicates a stronger fluid-structure interaction between the closing leaflets and the jet towards the end systole phase in Model #1. It should be noted that both RSS and TKE calculated in the present study were limited with the assumption that the turbulence characteristics can be represented by the 2D and phase-averaged measurements. The results obtained in the experiments reflect unsteadiness of the flow fields, but the real turbulence values can only be resolved when the temporal resolution is sufficiently high and the measurement is three-dimensional.

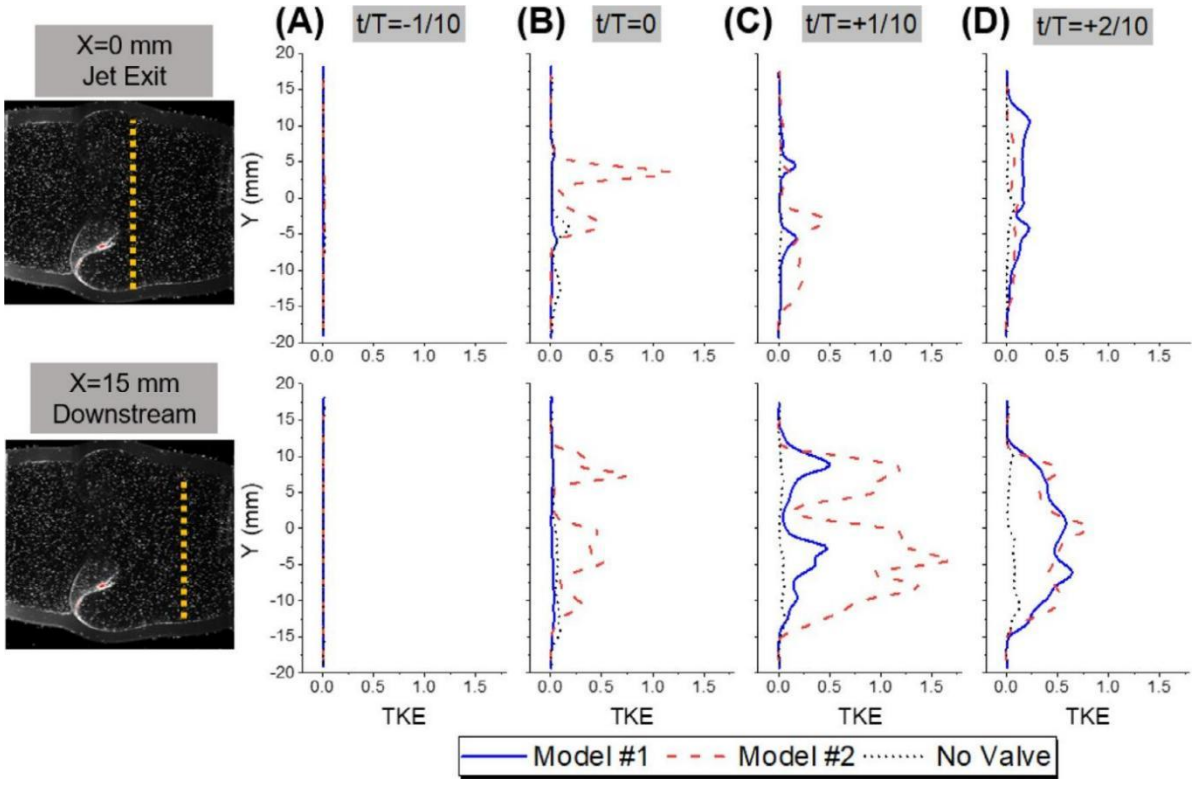

Figure 4.10. Normalized turbulent kinetic energy profiles extracted at the orifice (x = 0 mm) and 15 mm downstream, compared with the "no valve" case.

4.3.4. Phase-Averaged Flow Fields of Model #2 under Varied Heart Rates

To figure out the detailed flow characteristics inside stenotic Model #2 (stent constructed by our group), phase-locked PIV measurements were employed and the obtained results were analyzed at 10 separate phases under varied heart rates (50, 75 and 100 bpm), with the peak systole phase defined at t/T = 0. In Figure 4.11, the averaged axial velocity (U) was presented at 4 selected phases, i.e., peak systole, +1/10, +2/10 past peak, and +3/10 into the early diastole.

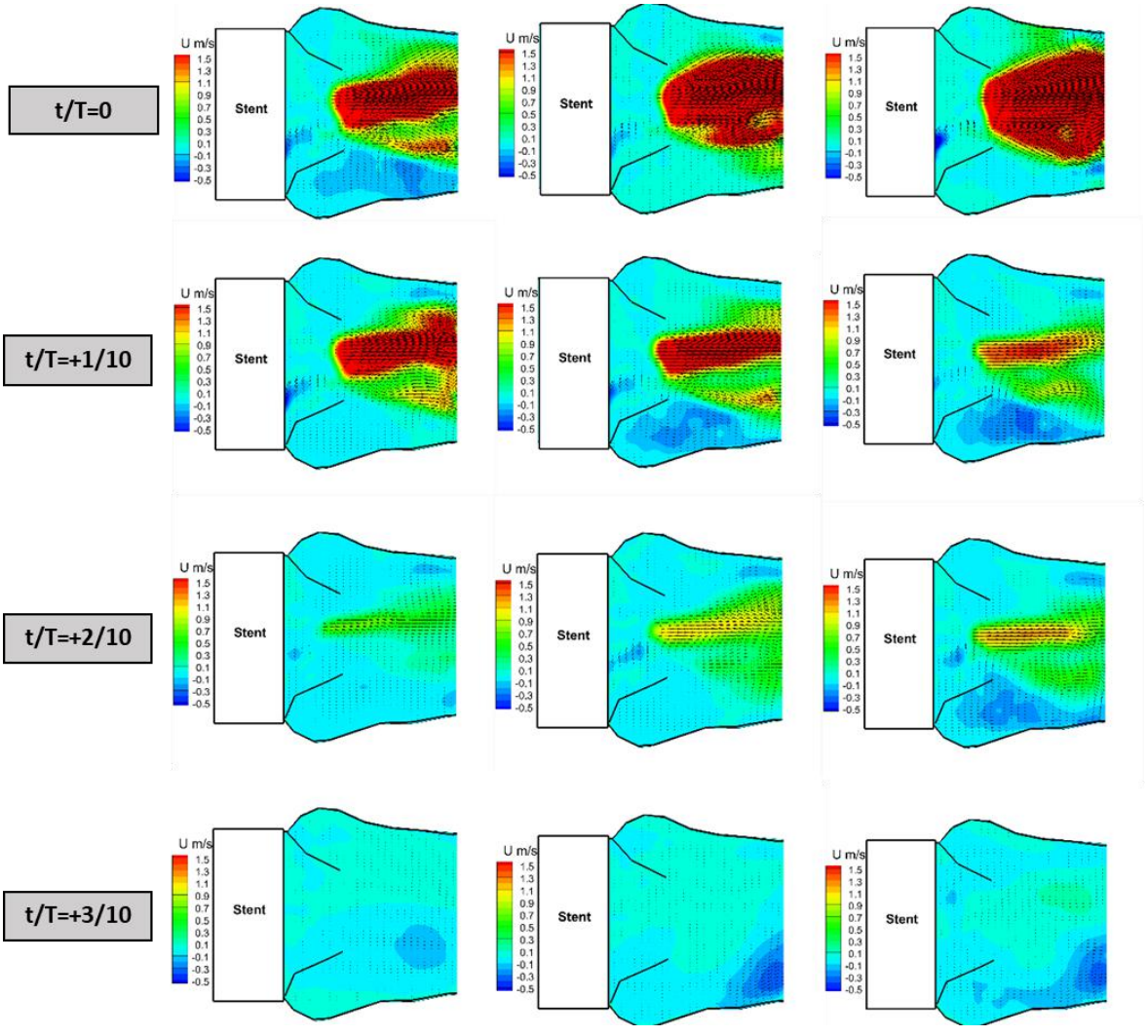

(a) 50 bpm (b) 75 bpm (c) 100 bpm

Figure 4.11. Phase-averaged velocity contours of Model #2 under varied heart rates: (a) 50 bpm; (b) 75 bpm; (c) 100 bpm (PIV data maximum uncertainty of ±5%).

In these figures, the boundary of the aortic root and valve boundaries were marked as the bold solid black lines based on raw images. The region "stent" is also illustrated in this figure to demonstrate the position where the model leaflets were fixed to the aortic root via its stent ring base, which can also be seen in Figure 4.1F.

The results clearly show that for all the cases, the jet flow peaked at t/T = 0, decreased at t/T = +1/10 to +2/10 phases, and diminished at t/T = +3/10 with the onset of diastole for all cases. A few significant differences were observed for the flow patterns downstream of stenotic Model #2 under varied heart rates:

First, the flow velocity at the peak systole (t/T = 0) was higher and the jet region was wider under a faster heart rate. To demonstrate this more clearly, Figure 4.12 compares the velocity profiles extracted from the PIV results at three locations downstream, namely the valve orifice (0 mm), 8 mm, and 16 mm downstream of the orifice. It can be seen that the widths of the jet were quite comparable at the valve orifice. The jet diameter is about 1 cm and a geometric orifice area can be estimated as 0.78 cm^2 by assuming a circular jet cross-section at this location (with ±2 % uncertainty of the velocity data). This aortic valve area confirms a severe AS case based on the classification from the guideline [171]. Overall, at 8 and 16 mm downstream of the valve orifice, the peak jet velocity was considerably higher at faster heart rate.

Second, under an increased heart rate, the jet flow dissipates faster immediately after peak systole, as evidenced by the velocity contours at t/T = +1/10. However, towards the end of systolic phase (t/T = +2/10), the maximum jet velocity was obviously higher at the 100 bpm case compared to 75 and 50 bpm cases. This trend has been made clear in Figure 4.13, which compares the jet velocity profile at 8 mm downstream of valve orifice at t/T = 0, +1/10, and +2/10 for each case. Overall, it can be summarized that the decreased heart rate (50 bpm)

contributed to a weaker peak jet flow, which however lasted longer due to the increased stroke volume. Meanwhile, the increased heart rate induced a stronger peak jet flow, whose strength quickly decreased after systole, but took longer (in term of cardiac phase) to fully dissipate.

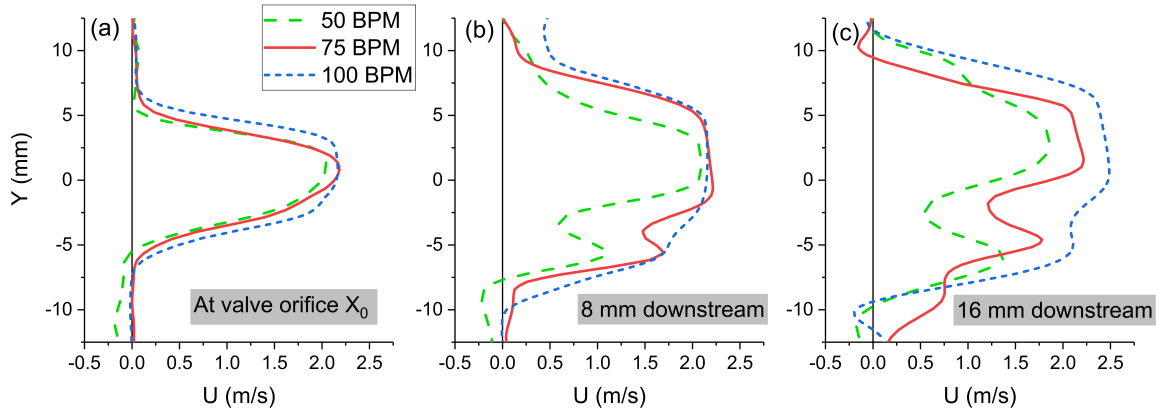

Figure 4.12. Velocity profiles of Model #2 at the valve orifice, 8mm and 16mm downstream of the valve at t/T=0.

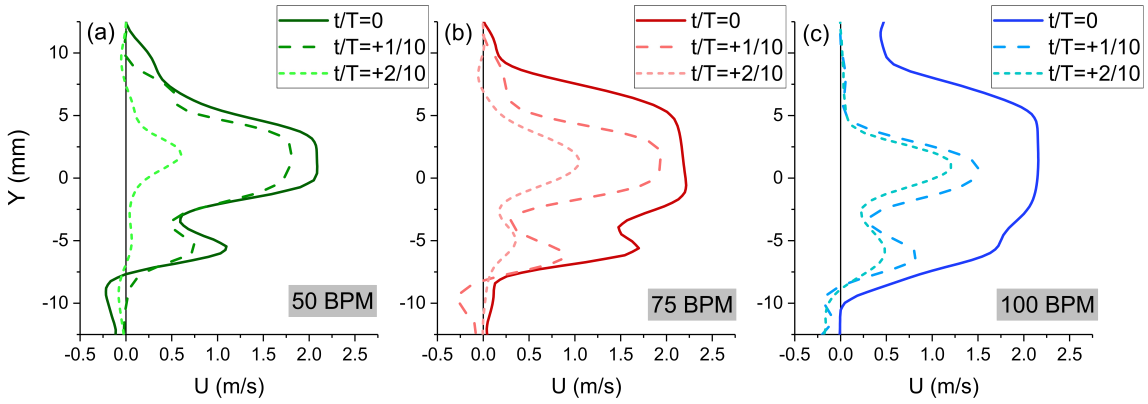

Figure 4.13 Velocity profiles of Model #2 - 8mm downstream of the valve orifice from t/T=0 to t/T=+2/10 under three heart rates.

4.3.5. Turbulence Kinetic Energy of Model #2 under Varied Heart Rates

Figure 4.14 shows the TKE contours from t/T = 0 to t/T = +3/10 for different heart rates (50 to 100 bpm). It is apparent that at peak systole (t/T = 0), the heart rate of 50 bpm generated much greater unsteadiness downstream of the valve. This result corresponds well with the finding of the narrower jet at 50 bpm (Figure 4.7). After peak systole, TKE dissipated fast at 50

bpm. In contrast, for 75 and 100 bpm cases, TKE increased significantly at t/T = +1/10. At t/T = +2/10 and early diastole t/T = +3/10, an increased heart rate caused a significantly increased TKE downstream of the stenotic valve.

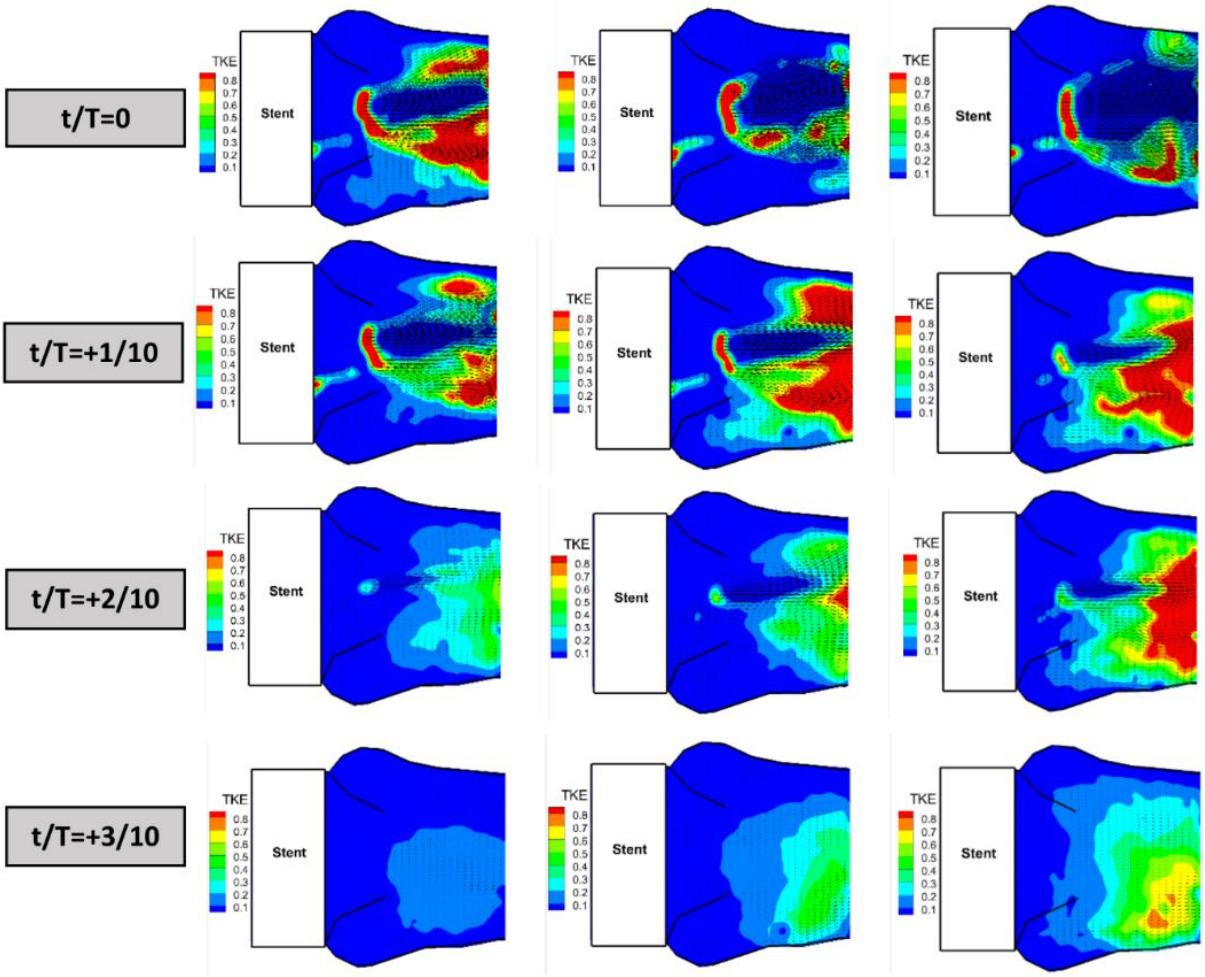

(a) 50 bpm (b) 75 bpm (C) 100 bpm

Figure 4.14. Normalized TKE contours under varied heart rates: (a) 50 bpm; (b) 75 bpm; (c) 100 bpm.

To investigate source of the stronger instability at 100 bpm, the experiments were repeated with the valve leaflet removed and only the stent installed inside the aortic root model, as shown in Figure 4.15. It is clearly demonstrated that at t/T = +2/10, the TKE was significantly lower than those shown in Figure 4.16. This result suggests that the increased late-systole

turbulence at the faster heart rates was mainly caused by the altered fluid-structural interaction between the pulsatile flow and the stenotic valve leaflets, instead of merely by the decelerating flow. However, at t/T = +3/10, the TKE was found to be greater at faster heart rates even though the stenotic valve was not involved, similar to what has been discussed in Figure 4.14. The results indicate that at early diastole, the flow unsteadiness was not less correlated with the valve leaflet dynamics, but was associated with faster flow deceleration due to the increased heart rate.

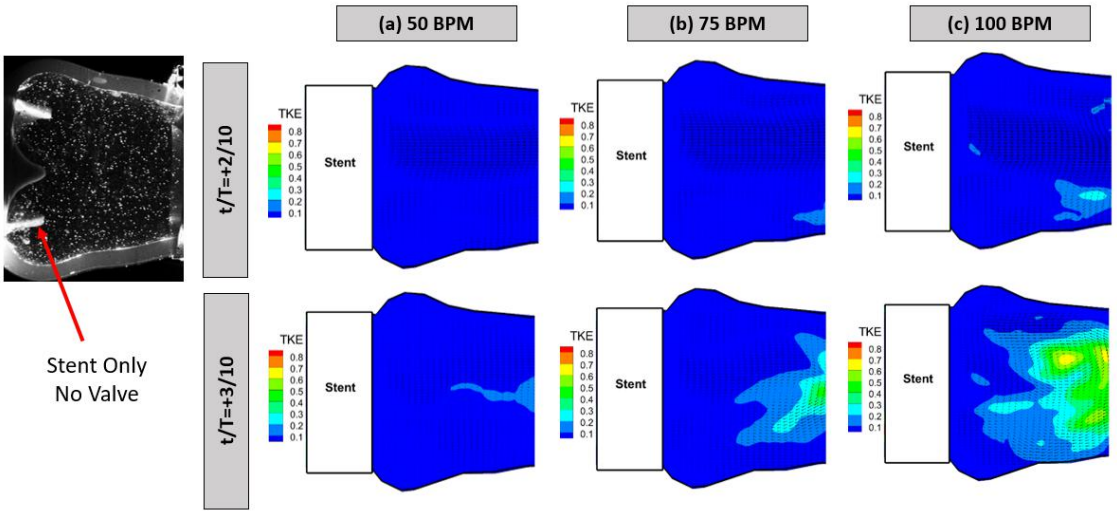

Figure 4.15. Normalized TKE contours with the stent only (no valve) under varied heart rates.

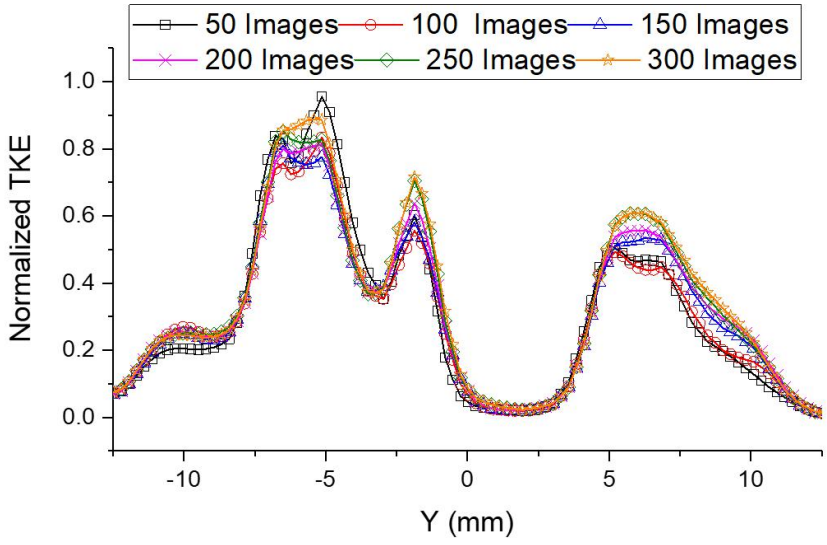

Figure 4.16. Convergence of the TKE data (8 mm downstream of the orifice, 50 bpm, t/T=0).

4.4. Discussion

4.4.1. Evaluation of Prosthetic Stenosis for Two Models at 75 bpm

For native aortic valves, severe stenosis could be diagnosed by a mean pressure gradient > 40 mm Hg according to the American College of Cardiology (ACC)/American Heart Association (AHA) guideline [171]. For more accurate assessments, an aortic valve area (AVA) or effective orifice area (EOA) that is less than 1.0 cm^2 is normally used as a criterion for several AS. The EOA can be estimated via different equations, one of which, the Gorlin equation, has been set as the gold standard for the past decades [174]. The Gorlin equation is defined as follows:

$$AVA = \frac{Q}{HR * T_s * 44.3\sqrt{\Delta P_m}} \tag{4.6}$$

where Q is the CO in mL/min, HR is the heart rate in beats per minute, T s is the systolic ejection period in seconds, ΔPm is the mean pressure gradient in mmHg. Despite its simplicity, the Gorlin equation uses several assumptions that does not consider the dynamics of a stenotic valve. For example, the Gorlin equation ignores the flow inertia to open the stenotic valve and the pulsatile aortic hemodynamics assuming a fixed orifice area and constant flow rate throughout the ejection period. Also it assumes a quadratic relation (square root) between the pressure and the flow, which could yield erroneous estimations in certain cases [175].

Using the Gorlin equation, the EOA of the two models has been calculated to be 1.65 and 0.74 cm^2, respectively (Table 4.3), indicating a moderate and severe stenosis as expected. In this table, the uncertainties estimated from the standard deviations of EOA calculated for 18 cycles (~15 s) were quite low for both models. Meanwhile, the acceleration time to ejection time ratio was estimated to be around 0.26 and 0.49 for Model #1 and Model #2, respectively, which correspond well with the clinical threshold of 0.35 for the determination of severe stenosis for

native aortic valves [177], [178]. These results suggest that the severity assessment of the prosthetic aortic valve stenosis was consistent with those used in clinical stenosis evaluations.

Table 4.3. Stenosis estimation for the two valve models used in this study.

	Effective Orifice Area (EOA, cm^2) Gorlin equation	Acceleration time (AT) to ET Ratio AT/ET
Model #1	1.65 ± 0.04	~ 0.26
Model #2	0.74 ± 0.01	~ 0.49

4.4.2. Hemodynamics of Stenotic Prosthesis for Two Models at 75 bpm

The PIV results reveal several distinct hemodynamics for moderate and severe prosthetic stenosis. First, severe stenosis increases the strength of the vorticity and jet velocity much more significantly than moderate stenosis throughout the systolic phases. The rapid increase in aortic jet velocity, which has been used as a predictor for asymptomatic severe AS for native valves [179], is also an indicator to determine prosthetic stenosis progression. Second, severe stenosis is also more likely to cause an eccentric jet flow due to the rapid expansion of flow after the narrowed orifice, as evidenced by Figure 4.5 and Figure 4.11. The eccentric jet could potentially increase the WSS leading to other significant ascending aortic diseases, similar to the impacts of congenital bicuspid aortic valve [180], [181].

In general, the turbulence level is significantly elevated in severe prosthetic stenosis. The distributions of TKE and RSS suggest the turbulence is more concentrated near the orifice and the shear layer of the jet flow under severe stenosis. The comparison to the "no-valve" case implies that the contribution of the pulsatile nature of the flow to turbulence is order-of-magnitude weaker than the contribution from the leaflet-flow interaction. The results also underline the important role of the leaflet stiffness, rather than the stent base structure, in determining the turbulence shear stress in the ascending aortic flow. The absolute values of maximum RSS ($\rho \overline{u'v'}$) for severe stenosis were estimated approximately 60 N/m^2, which is far

below the established threshold for red blood cell (RBC) damage (400 N/m^2, [182], [183]). The RSS value is very close to that reported in an in vitro experiment of a bi-leaflet mechanical valve [184]. However, it should be noted that RSS is only a statistical representation of the transport of average momentum fluctuations. The actual physical shear stress experienced by RBC or the platelet should be evaluated by the real-time viscous shear stress induced by turbulence, which could only be available in time-resolved 3D measurements. Nevertheless, according to Ge et al. [184], this RSS level is correlated to a viscous shear stress that is far below the risk threshold of hemolysis (RBC damage), but could potentially contribute to an elevated platelet activation and aggregation (threshold on the order of 10 N/m^2 , [185]).

4.4.3. Effects of Heart Rate on the Hemodynamics of Stenotic Model #2

The presence of the aortic valve stenosis causes increased jet velocity and leads to elevated WSS on the ascending aortic wall tissues downstream of the valve [186]. For Model #2, we demonstrated that the aortic jet velocity is strongly affected by heart rates under the same cardiac output. While the velocity profiles at the valve orifice were comparable, the jet velocity downstream of the valve at peak systole was significantly higher under the faster heart rate than that under the slower heart rate. Specifically, the jet velocity decreases from 0 mm to 16 mm downstream of the valve in the 50 bpm case, while in contrast, the jet flow accelerates through that distance in the 100 bpm case (Figure 4.12). According to the Bernoulli's principle, this flow acceleration downstream of the valve might indicate that a longer distance is required for pressure recovery, which is an important hemodynamic factor that quantifies the recovery of aortic blood pressure after the vena contracta. The consideration of pressure recovery is very important for an accurate assessment of AS severity through echocardiography [187]. Therefore,

the results imply that the heart rate should also be a consideration factor for determining the magnitude of pressure recovery for patient-specific AS assessment.

Aortic blood flow is one of a few cardiovascular sites where turbulence might exist even in healthy subjects due to the relatively high Re and Wo numbers [155]. Elevated blood turbulence, which is often diseased and age-related, is linked to the pathogenesis of many cardiovascular diseases, including thrombus formation and elevated WSS [188]. In this study, we show that the turbulence level induced by the stenotic aortic valve was also influenced by heart rates. While the turbulence at peak systole was higher under the 50 bpm heart rate, the turbulence during the late systole and early diastole phases was significantly higher under 100 bpm. Through the comparison with no valve cases, we also found that the differences of systolic turbulence were mainly produced by the interaction between the flow and the stenotic valve. However, the early diastolic turbulence was higher under the faster heart rate, even with the valve removed, indicating the instability of the flow at early diastolic was mainly from the deceleration of the pulsatile flow.

4.5. Conclusion

An in vitro Phase-locked particle image velocimetry (PIV) study has been conducted to investigate the fluid dynamics of two polymeric aortic valve prostheses with moderate and severe stenosis. Two models were built with similar tri-leaflet aortic valve geometries, but different materials and fabrication methods were applied. Through the pressure waveform analysis, the effective valve areas of the two models were estimated and represent moderate and severe prosthetic stenosis, respectively. Pressure waveforms also suggest that the severe stenosis caused a prolonged ejection period and an increased acceleration time ratio during the ejection period, which is similar to the clinical observations of the native aortic valve stenosis. In addition,

the pulsatile flow characteristics of the stenotic Model #2 were also investigated using PIV method under varied heart rates with the same cardiac output. Some important findings of this study are found as follows:

Phase-locked PIV was employed to study the flow fields of the two stenotic models. While the moderate stenosis did not show a significant increase in jet velocity compared with no-valve baseline, the severe prosthetic stenosis caused nearly a 2-fold increase in the peak jet velocity. Vorticity in the free shear layer of the jet flow was also increased in the severe stenosis case. Meanwhile, the severe stenosis induced a rapid expansion of jet downstream of the valve orifice, and cause a more eccentric jet flow pattern during the systolic period. Turbulence was evaluated based on the ensemble RSS and TKE in the two models. Results suggest a nearly 3-fold increase in peak TKE from the moderate to severe stenosis cases. Both valves introduced significantly higher turbulence after the peak systole than the no-valve baseline case, underscoring the important role of leaflet stiffness in the turbulence generation. The absolute RSS value is far below the risk threshold of red blood cell damage, but could potentially contribute to the elevated risk of platelet activation and aggregation.

For the flow characteristics of stenotic Model #2, the distribution of jet flow velocity downstream of this stenotic model is changed under different heart rates. While the peak velocity profiles at the valve orifice is comparable, the peak jet velocity downstream of the valve increases as the heart rate increases, implying a longer pressure recovery distance as the heart rate increases. And the normalized TKE was analyzed based on the ensemble flow field information. While the turbulence at peak systole is higher under the slower heart rate, the faster heart rate contributes to a significantly higher turbulence during the late systole and early diastole phases. Based on the comparison with no-valve cases, the systolic TKE was mainly

produced by the interaction between the pulsatile flow and the stenotic valve, while the early diastolic turbulence was still present even with the valve removed.

Results of this study indicate that a severe prosthetic stenosis causes significant changes in the flow field characteristics downstream of the stenotic aortic valve model. Some of the key parameters were consistent with the calculations by Gorlin equation used in clinical practice. The hemodynamic changes, including eccentric jet, increased jet velocity, and elevated turbulence and viscous shear stress, were associated with the stiffened leaflet materials, rather than the use of the stent base structure. Future improvements of artificial valve designs should capitalize on ultra-compliant, durable and anti-calcification leaflet materials, which will benefit patients by providing them optimal aortic hemodynamic outcomes with a prolonged lifetime after implantation.

5. COMPARISON OF PULSATILE FLOW CHARACTERISTICS IN ROMANESQUE AND GOTHIC AORTIC ARCH MODELS[3]

5.1. Introduction

In the previous two chapters (Chapter 3-4), the flow characteristics about prosthetic aortic valve models were studied. As another key part of the aorta, the dysfunctional aortic arch could also lead to the increased working load for heart causing aortic related diseases. Among them, Coarctation of the aorta (CoA) refers to the narrowing of the aorta, which is a congenital heart disease that often occurs in the aortic arch [40], [189]. Despite of successful repairs, many young patients still at high risk for cardiovascular complications, particularly systematic hypertension later in their adulthoods [39], [41], [42]. Clinical studies suggest systematic hypertension occurs for 20 - 40 % young adult survivors after successful repairs of CoA [46]. The causes of such complications have extensively been studied in recent years [43], [44]. One of the most significant factors has been identified as the deformation of the aortic arch after surgeries and the associated abnormal hemodynamics [45]. Overall, the abnormal arch geometry and related hemodynamics are associated with late systemic hypertension, aortic aneurysms, and other cardiovascular complications that are commonly seen in patients with successful surgical repairs.

Gothic and Romanesque aortic arches are two common phenotypes of deformed arch, which are named for their geometric similarity to the architecture styles. Clinically, the deformed geometries have been suggested having strong correlations with hemodynamic complications. Ou et al. [190] studied the blood pressure of three groups of patients with different deformed arch geometries, which showed the resting hypertension was significantly more frequent in

[3] The material in this chapter is adapted from a manuscript - Zhang, Yan, Zhang, Ruihang, Ullah, Al Habib, Thomas, Nick, Estevadeordal, Jordi, and Suzen, Yildirim Bora. "Experimental and Numerical Study of Pulsatile Flow Characteristics in Romanesque and Gothic Aortic Arch Models" submitted to Medical Engineering & Physics. The work was cooperated among Yan Zhang, Ruihang Zhang, Al Habib Ullah, Nick Thomas, Jordi Estevadeordal, and Yildirim Bora Suzen. Ruihang Zhang had primary responsibility for running experiments, collecting and analyzing data, and drafting the manuscript. Yan Zhang managed the project, revised the manuscript, and served as the corresponding author. Al Habib Ullah and Jordi Estevadeordal helped set up the tomographic PIV system. Nick Thomas and Yildirim Bora Suzen conducted the CFD simulations.

Gothic arch patients than in other geometry groups. In another study, Ou et al. [191] also shows that exercise-induced hypertension was also more frequent in patients with Gothic aortic arch. Their following research suggested the abnormal hemodynamics found in Gothic arch patient is strongly associated with early and enhanced systolic wave reflection and greater aortic stiffness [192]. Bruse et al. [193] analyzed the correlation between shape features and several left ventricular function indicators. They found that the deformation of aortic arch after CoA surgery was possibly associated with worsened left ventricular function. These clinical findings imply the complex hemodynamic mechanisms and highlight the needs for detailed fluid dynamic studies of deformed arch hemodynamics.

In recent years, clinical imaging and CFD simulation studies have been performed to understand the abnormal hemodynamics associated with aortic arch deformation. Hope et al. [42] performed a 4D MRI study which suggested that the Gothic arch has a tendency of having abnormal systolic helical flow in the descending thoracic aorta. Olivieri et al. [95] conducted a steady flow CFD simulation of three different deformed aortic arch geometries. Their results showed that Gothic arch has a unique location of peak wall shear stress (WSS) in the descending aorta compared with that in Romanesque and Crenel arches. Szopos et al. [94] conducted a CFD and fluid-structure interaction study of idealized Gothic and Romanesque arch hemodynamics. The aforementioned studies have different limitations in terms of quantitative flow measurements. Clinical imaging normally has limited spatial and temporal resolution, requires access to expensive facility, and is limited to specific boundary conditions.

Despite of these finding, previous CFD studies has been mostly focused on steady flow to represent the peak systolic flow in idealized geometries and the effects of pulsatile nature on the helical and vortical flow has not been fully studied so far. In addition, there is currently a lack of

experimental data of deformed aortic arch hemodynamics, which is important for direct physical insides and validation of such flow phenomena. In recent years, PIV experiments base on vessel phantoms has become an important alternative branch in hemodynamic research for various biomedical problems [75], [96]-[97], [194]. In vitro flow loop that mimics pulsatile waveforms provides a controllable way to study effects of boundary conditions.

In this study, we present a combined experimental and numerical study of the pulsatile flow characteristics within a Gothic and a Romanesque aortic arch model based on 2D planar PIV, 3D tomographic PIV, and 3D CFD simulations. The same deformed aortic arch geometries were used for the experimental phantoms and the computational domains. A pulsatile flow simulator was used for generating the flow waveforms and a phase-locked PIV setup was used to obtain ensemble-averaged data. CFD simulations were performed to provide insights into time-resolved flow characteristics and were compared with experimental results. The aim of this study is to understand the variations of primary and secondary flow features of a typical Romanesque and Gothic aortic arch, including flow separations, Dean-type vortices, and wall shear stress, under typical pulsatile flow conditions.

5.2. Experimental and Computational Methods

5.2.1. The Cardiovascular Flow Simulator

The experiment was conducted in a closed-loop pulsatile flow system as described in Chapter 2 and illustrated in Figure 5.1. The system was driven by a programmable pulsatile flow pump (PD-1100, BDC Laboratories). A diastolic pressure control module was installed at the pump outlet (upstream of the model) to adjust the diastolic negative pressure during the suction stroke of the piston pump. Furthermore, a compliance chamber and a flow resistance downstream were installed to adjust the pressure/flow magnitudes to maintain a desired

condition near the test section. A fluid reservoir was installed to collect the working fluid and to serve as a seeding particle mixer for the PIV measurements. In this experiment, pressure sensors with a high frequency response of 5 kHz were installed upstream and downstream of the aortic arch model outside the test section box. The sensors were connected to a data acquisition system (DAQ, National Instruments) to collect 75,000 pressure time series data for 15 seconds for each test case.

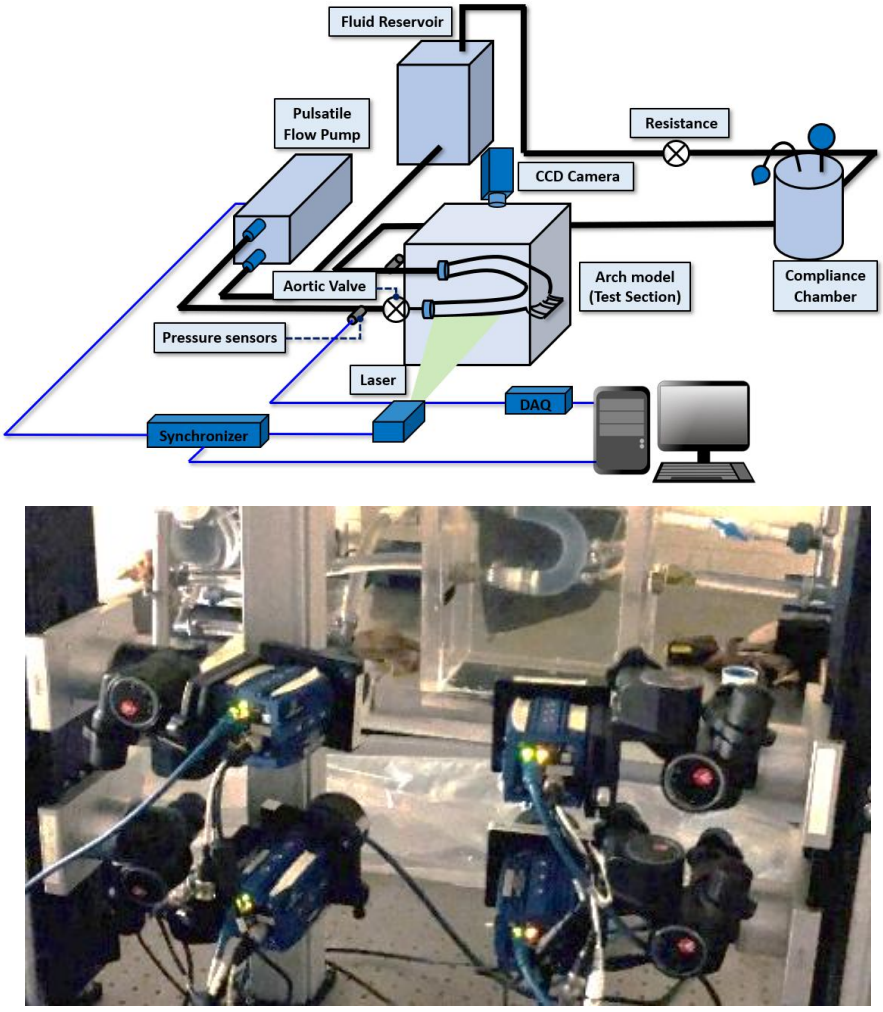

Figure 5.1. Schematic of the pulsatile flow loop (top) and tomographic PIV cameras setup (bottom).

5.2.2. Particle Image Velocimetry (PIV)

A PIV system was utilized to quantify the flow field characteristics (Figure 5.1). Double-pulsed Nd:YAG lasers with a 532 nm wavelength were selected. For the planar PIV measurement, the laser beams were shaped into a 1 mm thin laser using lens and a CCD camera with a resolution of 1,608 × 1,208 pixels was installed over the top of the model to capture the instant images. The field of view for the two models are 162 mm × 121 mm (Romanesque) and 180 mm × 135 mm (Gothic), respectively. Hollow glass microspheres (size of 10 μm and seeding density of 0.1 ppm) with a density close to that of water were used as seeding particles. The resulting Stokes number is much less than 1, which indicates that the tracers faithfully follow the streamlines. The raw images were post-processed using cross-correlation technique (LaVision DaVis software) to compute the instantaneous velocity vectors, which connected continuous frames of patterns of particle images with multi-pass interrogation process from a window size of 32 × 32 to 16 × 16 pixels. A 50 % effective overlap was selected to fulfill the Nyquist criterion. The bias error of PIV measurements mainly comes from the standard cross-correlation analysis of the raw particle images. Although the bias limit of the PIV measurements was not studied here, a good estimate of a standard PIV cross-correlations is within 5 % based on the detailed study [195]. The precision limit of the current phase-locked PIV average velocity is very small and estimated to be ±0.2 % (confidence interval of 95 %), based on the calculation of 300 velocity data samples extracted at a low turbulence flow region (standard deviation less than 2 % of the mean velocity). Thus, the maximum uncertainty of the 2D PIV is estimated to be less than 5 % of the measured data.

To obtain 3D flow data at the top cross section of the models, a tomographic PIV experiment was also performed for this study. In the tomographic setup, a combination of four

LaVision Imager LX cameras with adjustable Scheimpflug were used as shown in Figure 5.1. A volumetric laser illumination with a depth of 10 mm was formed by using a cylindrical lens and an aperture mechanism before projected into the top of models. The aperture makes the laser volume sharp at the edges and improves the data quality. To allow accurate reconstruction, the 4 cameras were placed on one side of the model with angles. After aligning the laser and cameras, the cameras were calibrated using LaVision's calibration plate and the 3D vector space was reconstructed. The calibration plate contained two surfaces to allow for 3D calibration with calibration dots of 2.5 mm in diameter and 10 mm distance vertically and horizontally from other calibration dots. All four cameras were calibrated at the same time with the center of the two calibration planes in the middle of projected laser volume. The volume correlation used 4 window sizes starting from a voxel size of 92 to 40 with each step using an overlap percentage of 75 %.

To eliminate the optical distortion caused by PDMS tube walls, a mixture of water-glycerin (40 % and 60 % respectively by volume) was used as the working mixture (a density of ρ = 1,160 kg/m^3 and a dynamic viscosity of μ = 0.012 Pa·s) to match the RI of the silicone model (RI = 1.43 under the ambient temperature). It should be noted that the viscosity of the fluid mixture is much higher than typical blood viscosity, and the non-Newtonian properties of the blood due to the red blood cells were not simulated by this fluid mixture. Nevertheless, the peak Reynolds number (~ 3,200) simulated in these experiments are within the typical range of aortic hemodynamics. The non-Newtonian properties would not affect the overall flow characteristics under the high Re aortic flow condition, as suggested by many previous PIV and CFD studies [51], [116].

5.2.3. Aortic Arch Model and Refractive Index Matching

Figure 5.2 shows the raw images of the Romanesque and Gothic aortic arch models, which were constructed from PDMS materials based on scanned patient data (BDC Laboratory). While the Romanesque model showed a relatively smooth arch and near semicircular geometry, the Gothic model was approximately a triangular geometry with a turning angle greater than 270 degrees. The height-to-width ratios (i.e., H/W in Figure 5.2) for the Romanesque and Gothic models were around 0.55 and 0.85, respectively, which fall in the normal range of clinically-observed H/W for Romanesque and Gothic arches [191]. It should be noted that both models have 3 arterial branches (i.e., innominate, left common carotid, and left subclavian arteries) in the arch section. During this study, flow through these branches were blocked to allow us to isolate the effect of arch geometry on the flow field only.

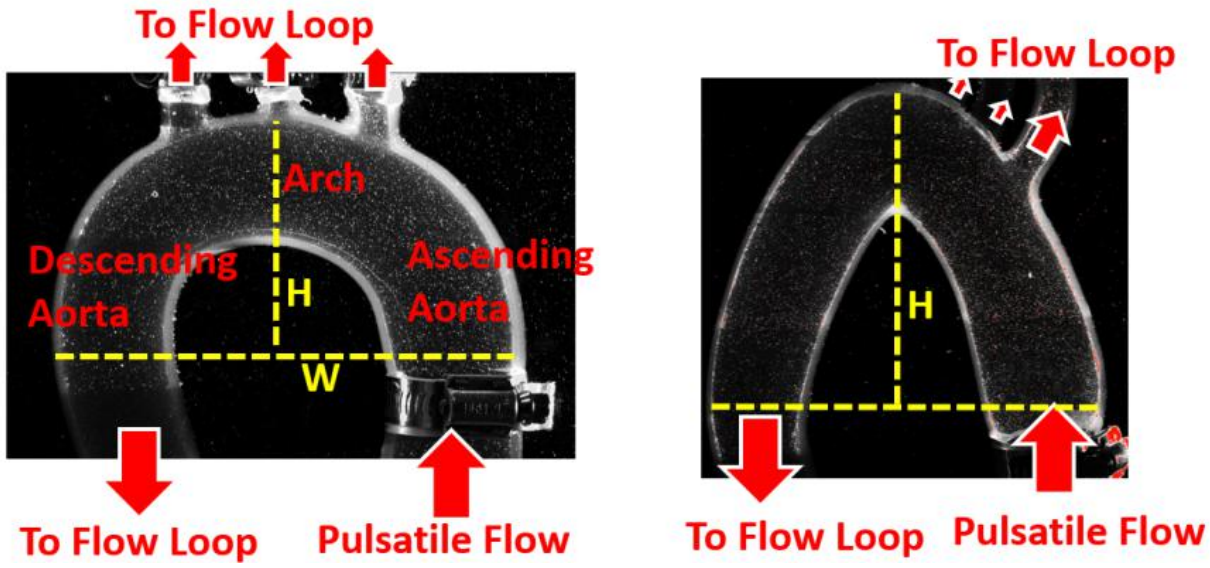

Figure 5.2. Raw PIV images of the Romanesque (left) and Gothic aortic arch (right).

5.2.4. Experimental Conditions

All experimental were conducted under an average flow rate (i.e. cardiac output) of 5 L/min and a heart rate of 60 beats per minutes (bpm). The pressure and flow waveforms (Figure

5.3) were generated by the reciprocating motion of the piston pump, which is triggered by a skewed sinusoidal signal from the function generator. The skewness was introduced to ensure that the compression stroke (i.e. ventricular systole) takes 40 % of the entire cycle time. This systole-time-ratio falls within the typical range of human cardiac physiology [154], [196]. All PIV measurements were performed at 10 phase-locked timing in a cycle. To compare results among cases, we used a normalized time, i.e. t/T, where t is the actual time and T is the cycle period for each heart rate, and then assign t/T = 0.0 to the phase when the maximum flow occurs at the inlet, i.e. the peak systole phase. The peak flow Reynolds number (Re) was around 3,200, which is defined based on the peak centerline velocity downstream of the aortic valve during the cycle. The Womersley number α, which quantifies the pulsatility of the flow, is 11.7 for 60 bpm. The equations for peak Re and α are

$$Re = \rho d_a u_p / \mu \tag{5.1}$$

$$\alpha = 0.5 d_a \sqrt{\omega \rho / \mu} \tag{5.2}$$

where u_p represents the peak velocity of the aortic inlet; d_a is the diameter of aortic arch inlet (30 mm); r_a is the radius of aortic inlet; ρ is the density of the working fluid; μ is the dynamic viscosity of the working fluid; ω is the angular frequency of the pulsatile flow from the pump. Both Re and Womersley numbers of the current experiments are within the reasonable physiological range of aortic flow [197].

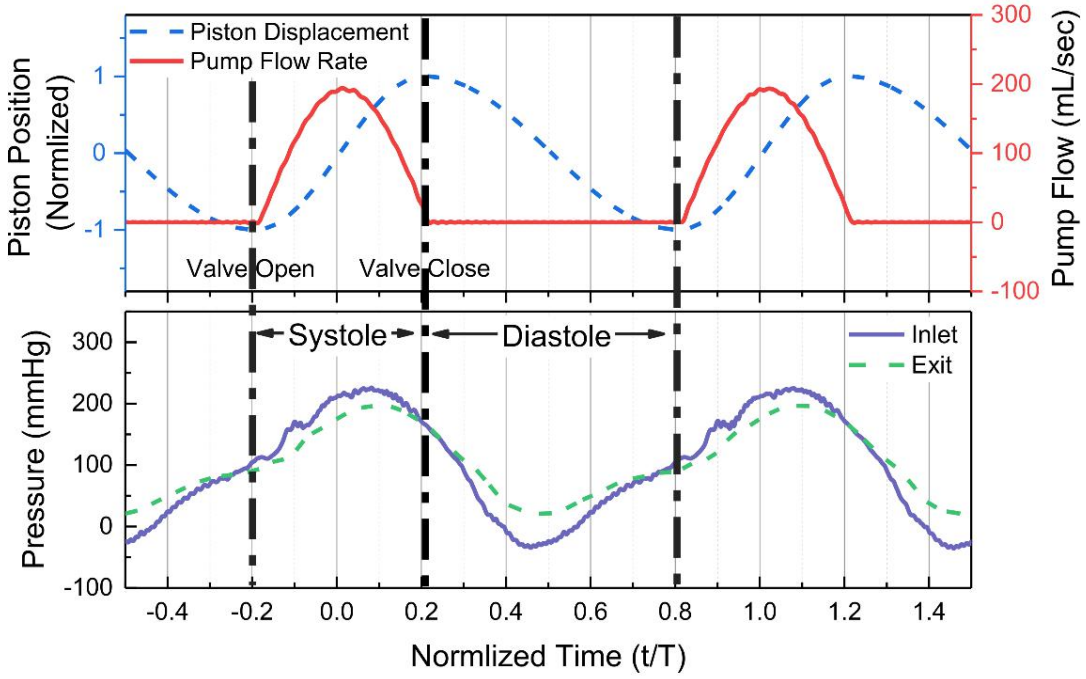

Figure 5.3. The pump displacement/flow rate (upper) and pressure waveforms (lower).

5.2.5. Computational Simulation

3D CFD simulations have been conducted for the two aortic models using ANSYS CFX. Figure 5.4 shows the computational domains and meshes generated using ANSYS ICEM. The structured mesh was constructed with hexahedra cells with a total number of approximately 1.1×10^6 and 1.5×10^6 in the Romanesque and Gothic arch models, respectively. The maximum element size is ~1 mm and an inflation of ~ 0.06 mm is applied around wall boundaries. It should also be noted that an inlet tube has been implemented in each computational domain to fully compare with the experimental condition and to provide enough entry length for flow development. For boundary conditions, the pulsatile flow rate waveform generated by the pump was used at the inlet and the outlet was set to follow the exit pressure waveform measured during the experiment. All walls were set to no-slip wall boundary conditions.

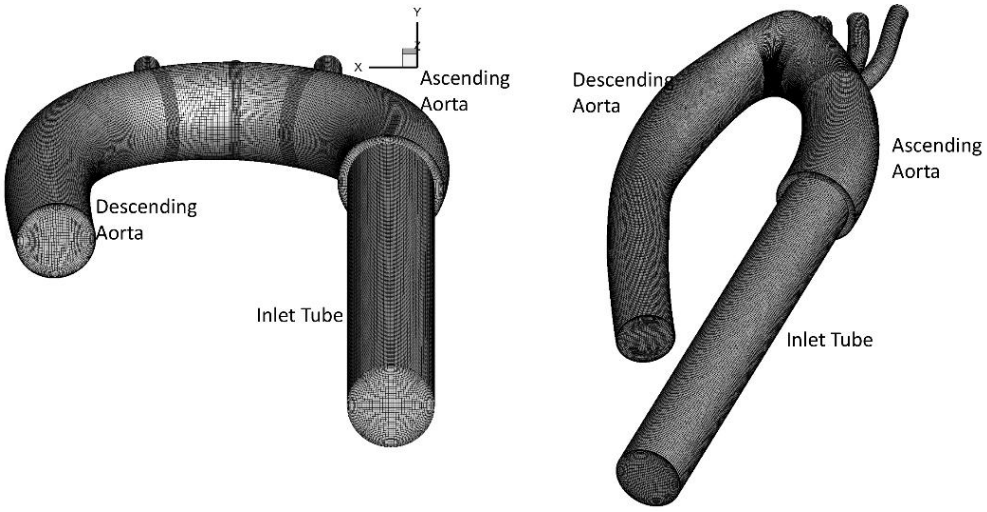

Figure 5.4. Computational domain and mesh for Romanesque (left) and Gothic (right) aortic arch models.

The Menter's $k-\omega$ Shear Stress Transport (SST) model was created in an effort to combine the best qualities of both the $k-\varepsilon$ and $k-\omega$ models [198]. It utilizes a blending function to use the $k-\omega$ model nearest to walls and the $k-\varepsilon$ farther away. In addition, a shear stress limiter is included in regions of adverse pressure gradients. To combine the $k-\omega$ and $k-\varepsilon$ models, the $k-\varepsilon$ model is first transformed into the form of a $k-\omega$ model by use of $\omega = \varepsilon/(\beta^* k)$, where $\beta^* = c_\mu$ [199]. The transport equations for turbulent kinetic energy, k, and specific dissipation rate, ω, are given below in Eq. 5.3 and Eq. 5.4.

$$\frac{\partial k}{\partial t} + \frac{\partial}{\partial x_j}(\bar{v_j} k) = \frac{\partial}{\partial x_j}\left[\left(\nu + \frac{\nu_t}{\sigma_k}\right)\frac{\partial k}{\partial x_j}\right] + P^k - \beta^* k\omega \tag{5.3}$$

$$\frac{\partial \omega}{\partial t} + \frac{\partial}{\partial x_j}(\bar{v_j}\omega) = \frac{\partial}{\partial x_j}\left[\left(\nu + \frac{\nu_t}{\sigma_\omega}\right)\frac{\partial \omega}{\partial x_j}\right] + \alpha\frac{P^k}{\nu_t} - \beta\omega^2 + 2(1-F_1)\sigma_{\omega 2}\frac{1}{\omega}\frac{\partial k}{\partial x_i}\frac{\partial \omega}{\partial x_i} \tag{5.4}$$

The key difference in the $k-\omega$ and $k-\varepsilon$ models is the inclusion of the final term in Eq. 5.4. The degree of this term's influence is controlled using the blending function F_1 given in Eq. 5.5,

where d is the distance to the nearest wall node. A value of $F_1 = 0$ reverts to the $k-\varepsilon$ formulation (far from walls), and a value of $F_1 = 1$ reverts to the $k-\omega$ formulation (near walls).

$$F_1 = \tanh(\xi^4),\ \xi = min\left[max\left\{\frac{\sqrt{k}}{\beta^*\omega d},\ \frac{500\nu}{d^2\omega}\right\},\ \frac{4\sigma_{\omega_{k-\varepsilon}} k}{CD_\omega d^2}\right], \tag{5.5}$$

$$CD_\omega = max\left\{2\sigma_{\omega_{k-\varepsilon}} \frac{1}{\omega}\frac{\partial k}{\partial x_i}\frac{\partial \omega}{\partial x_i},\ 10^{-10}\right\} \tag{5.6}$$

Constants in the transport equations (α, β, σ_k, and σ_ω) are blended linearly between their $k-\omega$ and $k-\varepsilon$ values according to F_1,

$$x = F_1 x_{k-\omega} + (1 - F_1) x_{k-\varepsilon} \tag{5.7}$$

for an arbitrary constant x.

Similarly, a second blending function, F_2 is used in the computation of the eddy viscosity, ν_t, as seen in Eq.5.8. The inclusion of the max function in the denominator is the previously mentioned shear stress limiter, which reverts to the $k-\omega$ formulation for eddy viscosity if the production is too large (when $\bar{s}$ is large) [199].

$$\nu_t = \frac{a_1 k}{max(a_1\omega, |\bar{s}|F_2)},\ F_2 = \tanh(\eta^2),\ \eta = max\left\{\frac{2\sqrt{k}}{\beta^*\omega d},\ \frac{500\nu}{d^2\omega}\right\} \tag{5.8}$$

The constants for the SST model used in this study are given below [199]:

$$\beta^* = 0.09,\ a_1 = 0.31 \tag{5.9}$$

$$\alpha_{k-\omega} = \frac{5}{9},\ \beta_{k-\omega} = \frac{3}{40},\ \sigma_{k,\ k-\omega} = 0.85,\ \sigma_{\omega,\ k-\omega} = 0.5$$

$$\alpha_{k-\varepsilon} = 0.44,\ \beta_{k-\varepsilon} = 0.0828,\ \sigma_{k,\ k-\varepsilon} = 1,\ \sigma_{\omega,\ k-\varepsilon} = 0.856$$

A timestep study was performed to determine the appropriate timestep for the transient simulation. Four different timesteps, i.e. $\Delta t = 0.01, 0.005, 0.002, 0.001$ seconds, were used in the simulation for the Romanesque geometry. The velocity profiles extracted on the top cross section were compared in Figure 5.5. Since all results agreed very well, the time step of $\Delta t = 0.01s$ was chosen for the rest of the study. For all cases, a total time of 10 seconds was simulated with the first 3 cycles to initialize. The computational data were then analyzed by averaging the remaining 7 cycle (7 seconds) data.

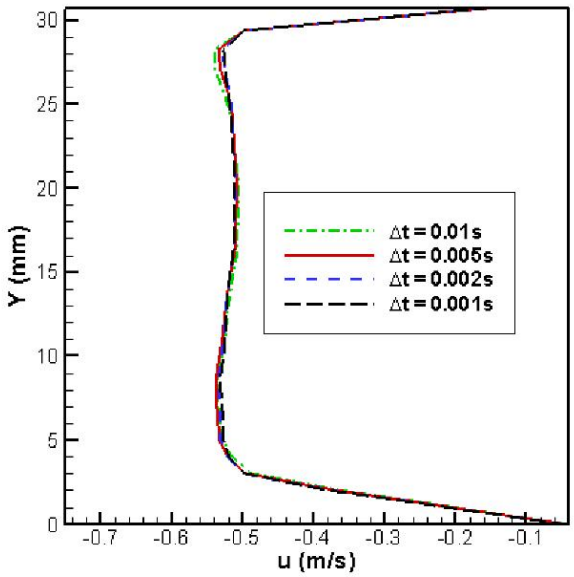

Figure 5.5. Velocity profile vertically along the top plane with varied time steps (CFD).

5.3. Results

5.3.1. Primary Flow Characteristics

The aortic flow is driven by the highly pulsatile nature of the cyclic ejection from the heart. As the heart compresses, the flow quickly accelerates into the ascending aorta, reaches the peak systolic flow, and then decelerates until the systole ends. The characteristics of these systolic flow phases in the primary plane are displayed for PIV experiments and CFD simulations in Figure 5.6 and Figure 5.7, respectively. Hereby we define the 3D space of the

results in x-y-z coordinates, in which x is the horizontal (left-right) direction, y is the vertical (inferior-superior) direction, and z is the depth (anterior-posterior) direction. The PIV results was ensemble-averaged from 300 instantaneous data that was locked at the specific phases, while the CFD results was an average of 7 continuous cycle. In these results, the velocity magnitude was normalized by the mean velocity of a cycle, i.e. $\bar{U} = Q/A$, where Q is the cardiac output of 5 L/min (cycle average), and A is the cross-sectional area of the inlet. To facilitate the comparison, the time of both experiment and simulations was normalized by the cycle period and set to t/T = 0 for the peak systole phase. It is worth mentioning that the PIV laser sheet was generated from the right to the left. Therefore, the illumination for part of the descending aorta was blocked in the Romanesque model because of the longer horizontal wall in the laser direction (the "shadow" region indicated in Figure 5.6).

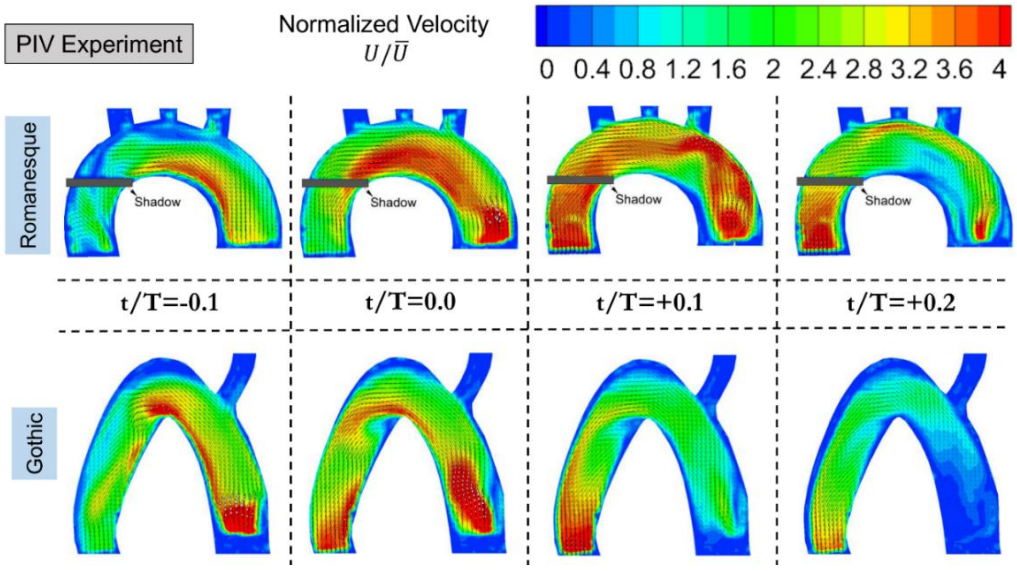

Figure 5.6. PIV normalized velocity contours in the X-Z plane for Romanesque (top row) and Gothic (bottom row) aortic arch models.

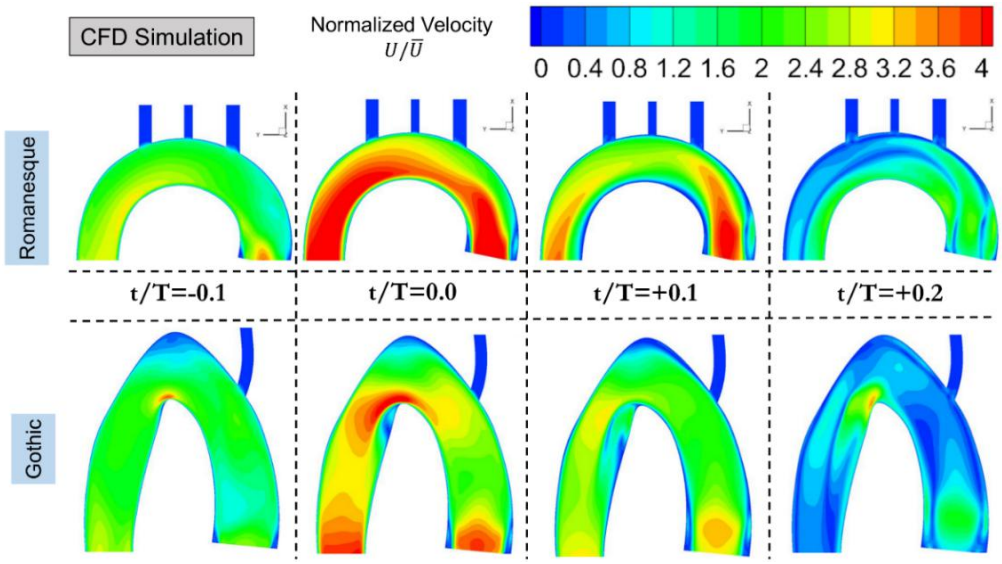

Figure 5.7. CFD normalized velocity contours in the X-Z plane for Romanesque (top row) and Gothic (bottom row) aortic arch models.

Both PIV and CFD results demonstrate several prominent features of primary flow (axial velocity) fields of Romanesque and Gothic arches. For the Romanesque arch, the high velocity region is skewed towards the inner side of the arch at the phase t/T = -0.1 before the peak systole. As the time passes the peak stole t/T = 0.0 and decelerates during t/T > +0.1, the primary flow becomes more uniform transversely. The time-dependent transverse flow change is a clear evidence of the centrifugal force acting on the fluid flow due to the smooth curvature of the model. For the Gothic arch model, however, severe distinct flow patterns were observed from both PIV and CFD results. First, the skewed high flow near the inner side consistently exists throughout the systolic phases. The high velocity develops near the sharp corner and forms a separation jet that impinges on the outer wall of the descending aorta. The flow separation also caused a recirculating “bubble” region on the inner side of the descending aorta just downstream of the arch apex. The flow fields are self-similar in distribution patterns throughout the systole despite of the flow magnitude changes. Second, there exists a constantly low velocity region near the top of the Gothic arch, as marked in Figure 5.6 and Figure 5.7, which is not seen in the

Romanesque model. The flow stagnation near the top is a direct result of the sharp curvature and might have hemodynamic implications for complications. To quantitatively examine the results, the normalized velocity profiles on the top cross-sections of the two arch models were extracted and plotted in Figure 5.8. It can be seen while the Romanesque model shows more uniform velocity distributions past peak systole, the Gothic model displays self-similar profiles of high velocity near the inner side and a low velocity near the outer side. Overall, the PIV and CFD results show a good agreement, particularly near the peak systolic phases.

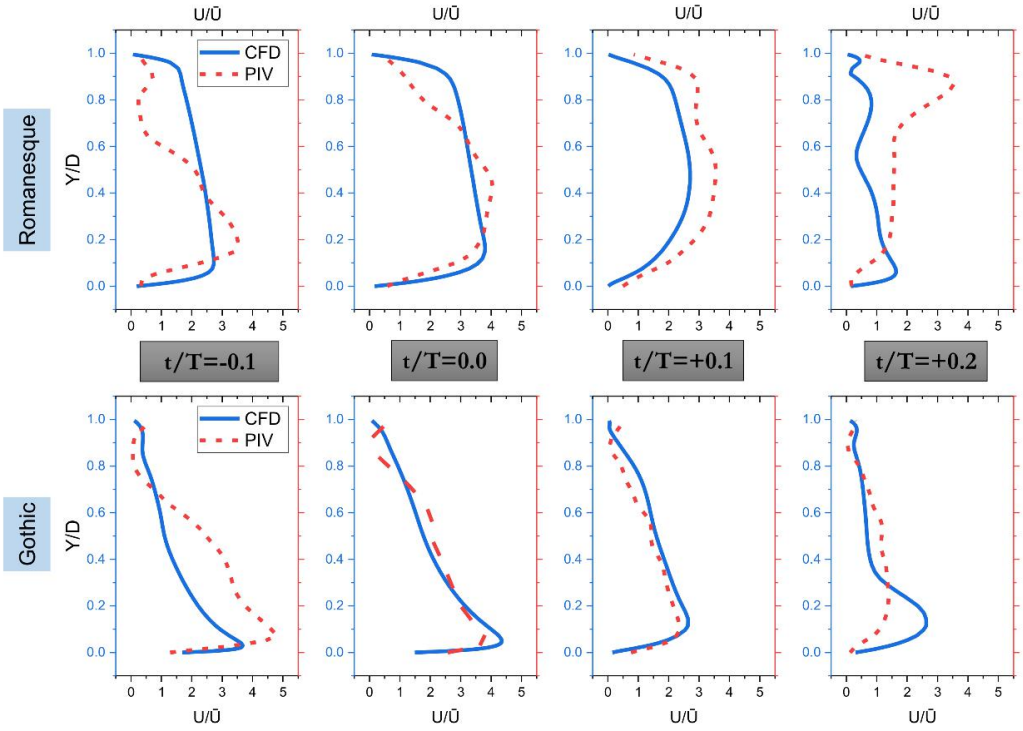

Figure 5.8. Comparison of normalized velocity profile on the top cross-section for Romanesque (top row) and Gothic (bottom row) models.

5.3.2. Secondary Flow Characteristics

The flow in both Romanesque and Gothic arches exhibits rich secondary flow characteristics and three-dimensional features. Figure 5.9 shows the 3D streamlines colored by the normalized velocity magnitude for two models at four systolic phases from the CFD simulations. The results suggest at the acceleration phase t/T=-0.1, both models display relative

straight streamlines without significant secondary flow. At peak systole t/T=0.0, helical patterns start to develop in the descending aorta. At t/T=+0.1 and +0.2, both models show strong 3D flow characteristics as the flow decelerates.

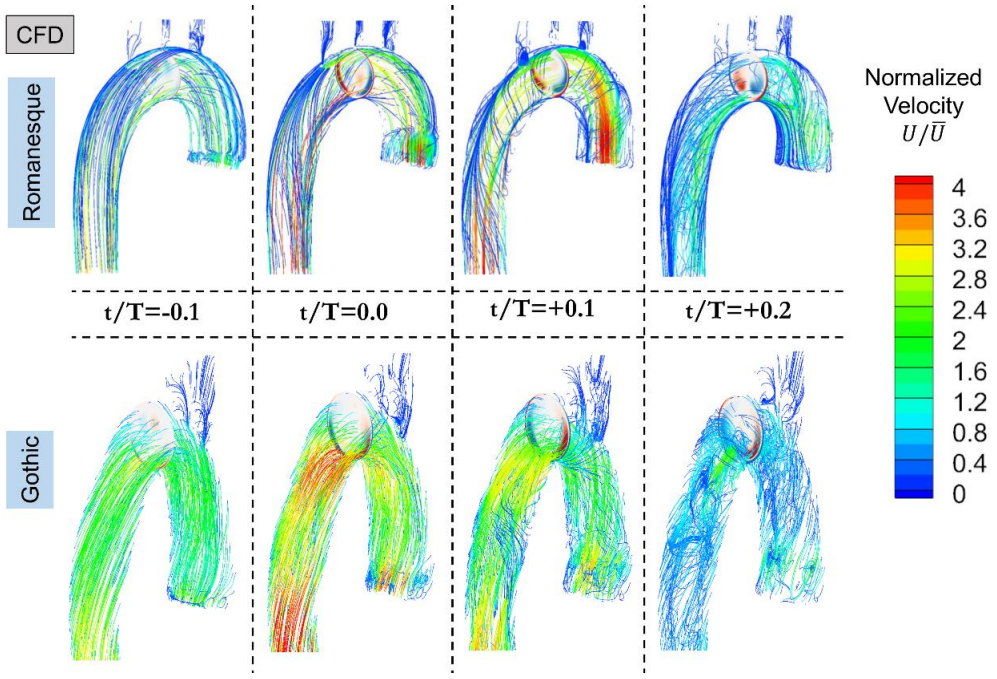

Figure 5.9. Streamlines during the systole for Romanesque (top row) and Gothic (bottom row) models (CFD simulation).

Figure 5.10 and Figure 5.11 compare the secondary flow patterns extracted from the top cross sections of the two models at the peak systole. The normalized velocity and the distribution of the out-of-the-plane vorticity are plotted from the CFD results and compared with the vorticity iso-surface generated from the tomographic PIV measurements. It can be seen that in both models, the peak flow generated a pair of counter-rotating vortices near the anterior-posterior wall surfaces. Such vortices are a common feature for flow past curved pipe, as also discussed by previous literatures [34], [200], [201]. The vortices are driven by the upward secondary flow motion near the centerlines. However, the comparison suggests a few key differences of secondary flows in the two arch models: First, the CFD results display an additional pair of vortices near the center of the Romanesque section, while such vortices are not present in the

Gothic section; Second, the wall vortices stay much closer to the wall in the Gothic section and a much greater vertical velocity was observed concentrated near the bottom of the Gothic section; Third, the velocity distribution is more uniform across the top section in the Romanesque model, compared to the stratified velocity distribution in the Gothic section. The results from CFD agree well with the tomographic iso-surfaces at the peak systole.

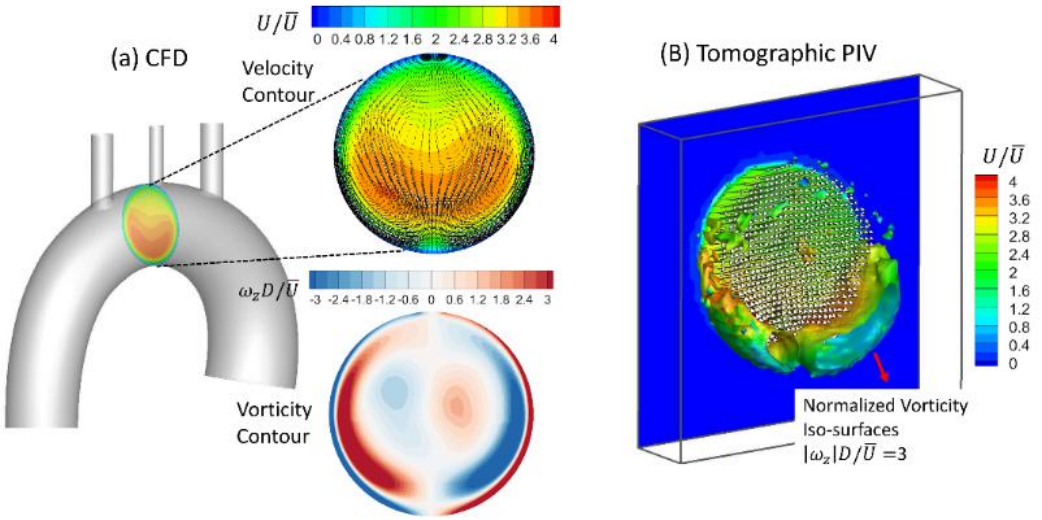

Figure 5.10. Secondary flow structures on the top cross-section of the Romanesque model shown by CFD simulation (a) and tomographic PIV measurements (b).

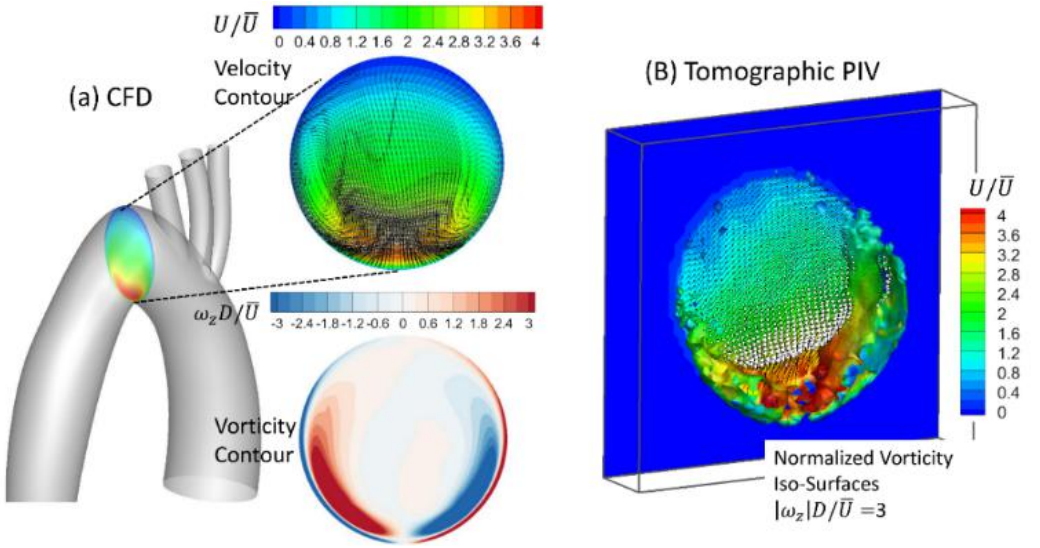

Figure 5.11. Secondary flow structures on the top cross-section of the Gothic model shown by CFD simulation (a) and tomographic PIV measurements (b).

To further examine time-dependent secondary flow features, the streamlines and velocity magnitude contours of the top sections were compared in an entire cardiac cycle for Romanesque and Gothic models, in Figure 5.12 and Figure 5.13, respectively. As can be seen in Figure 5.12, the central pair of vortices roll up during the acceleration of the flow from t/T=-0.1 to t/T=0.0 in the Romanesque model. As the flow decelerates (t/T=0.0 to t/T=+0.1), the wall vortices near the bottom develop strength and begin to dominate the entire cross section (t/T=+0.2). In diastolic phases (t/T=0.3 to t/T=-0.2), this contour-rotating vortex structure persists while the flow velocity diminishes. The vortical structure during the diastolic period resembles the "Dean-type" vortices of the steady flow passing the curved pipes, which have been discussed by previous literature. In comparison, Figure 5.13 displays distinct secondary flow characteristics for the Gothic model. In contrast to the Romanesque model, the velocity distribution of the Gothic top section is highly skewed throughout the systole, with high velocity concentrated near the inner (inferior) wall and near stagnant flow near the top. This corresponds well with the results shown for the primary plane in Figure 5.6 and Figure 5.7. In addition, although a pair of wall vortices were generated near the inner (inferior) wall at t/T=0.0 and +0.1, such vortices did not roll into the typical Dean-type vortices that occupied the entire section as similar to what was observed for the Romanesque model during the entire post-systolic phases. Instead, the vortices were drawn towards the bottom at the end of systole (t/T=+0.2) and then rolled towards the center by the secondary flow motion during the diastolic phases (t/T=+0.3 to -0.2). These distinct secondary vortex dynamics are directly associated with the skewed velocity distribution and the large vertical velocity comp caused by the sharp curvature.

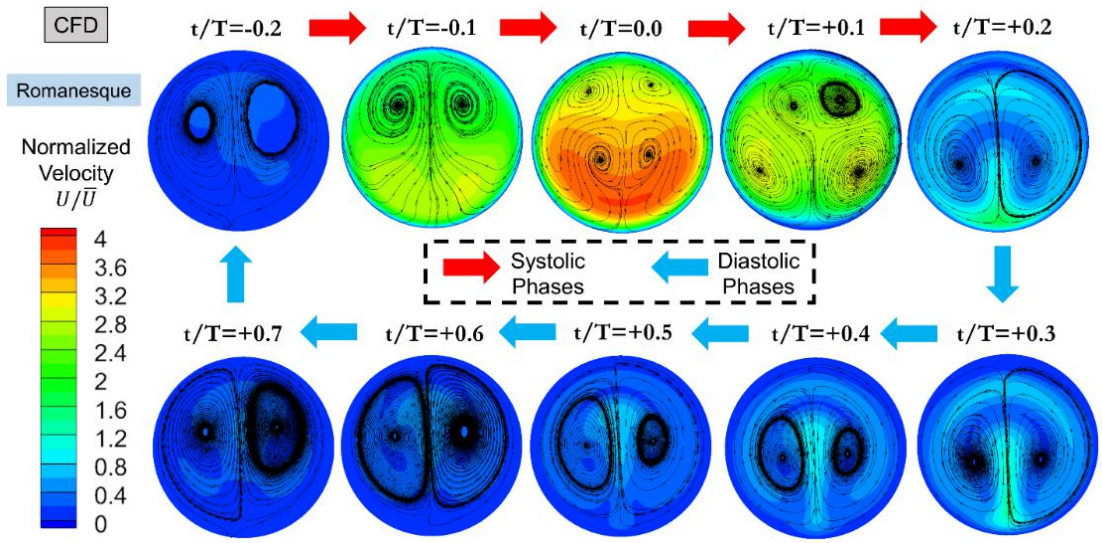

Figure 5.12. A whole-cycle variation of secondary flow features on the top cross-section of the Romanesque model (CFD).

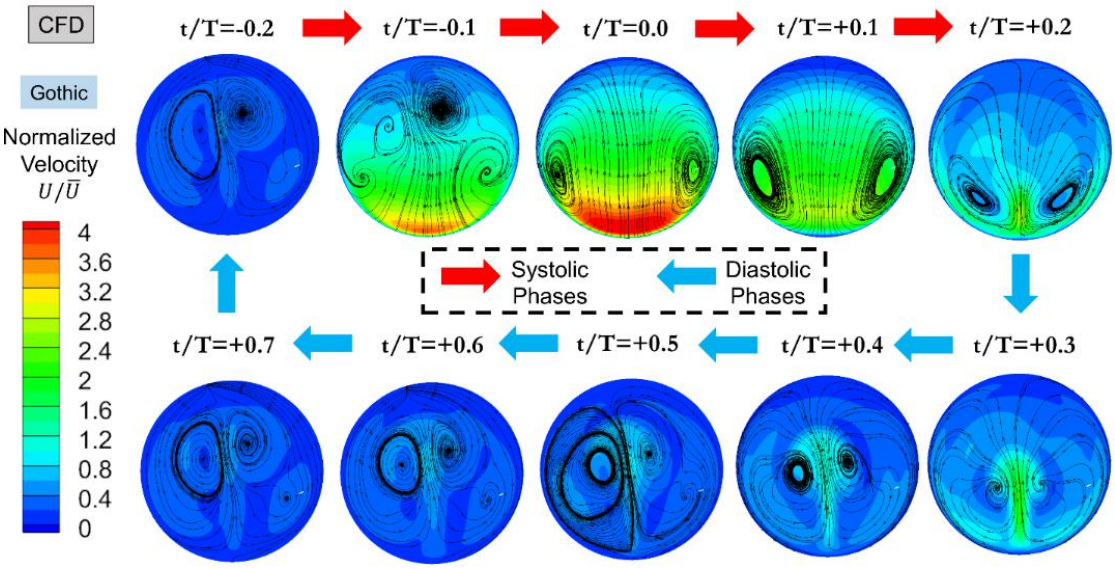

Figure 5.13. A whole-cycle variation of secondary flow features on the top cross-section of the Gothic model (CFD).

The 3D coherent structures (Q-criterion iso-surfaces) of the vortical flow were identified from the CFD results and compared between the two models in Figure 5.14 and Figure 5.15 for the systolic phases and diastolic phases, respectively. The Q criterion is calculated based on the second invariant Q of the velocity gradient tensor:

$$Q = \frac{1}{2}(\quad \Omega\|^2 - \quad S\|^2) \tag{5.10}$$

where Ω is the vorticity tensor and S is the rate of strain tensor. In these figures, the top section vorticity contours are also plotted for each phase.

In Figure 5.14, the phases t/T=-0.2 to t/T=+0.2 were displayed with the Romanesque in the top row and the Gothic in the bottom row. The Q = 10 iso-surfaces were shown for these systolic phases and was colored with normalized velocity magnitude. The results clearly suggest that in the Romanesque model, the Dean-type vortices was formed and moved towards the center of the vessel from the peak systole t/T=0.0 to the end of systole t/T=+0.2. A smoothly connect iso-surfaces was identified from the ascending aorta to the descending aorta, suggesting a continuous secondary flow behavior throughout the arch. In contrast, such continuous Dean-type vortices was not observed in the Gothic arch during the systole. At t/T=+0.2, small vortical structures formed immediately downstream of the sharp corner near the inner wall, which was mainly contributed by the flow separation and deceleration.

The trends continue into the diastolic phases from t/T=+0.3 to t/T=+0.7 as shown in Figure 5.15. It is clear that in the Romanesque arch, despite the flow strength diminished, the Dean-type vortices sustain during the diastolic phases. However, such continuous Dean-type vortices was also not observed during the diastolic phases in the Gothic arch. It is interesting to see that a pair of the vortices that formed during the systolic phases lifted up towards the outer (superior) wall in the descending aorta as the flow diminished. Nevertheless, there is a consistent lack of smooth and continuous Dean-type vortices throughout the entire cycle in the Gothic arch model.

The distinct behavior in generating Dean-type vortices were further validated through experiments. Figure 5.16 shows the comparison of the normalized downwards (z-component)

velocity on middle longitude section of the descending aorta at t/T=+0.1 phases from both PIV and CFD results. The velocity contour pattern in the Romanesque arch shows two high velocity regions separated towards the anterior and posterior walls of the descending aorta, suggesting the influence of the counter-rotating Dean vortices in this section. In Gothic model, however, the velocity distribution in the anterior-posterior direction was relatively uniform in the descending aorta, suggesting the lack of such coherent structures. The PIV and CFD results agree well in this flow phase.

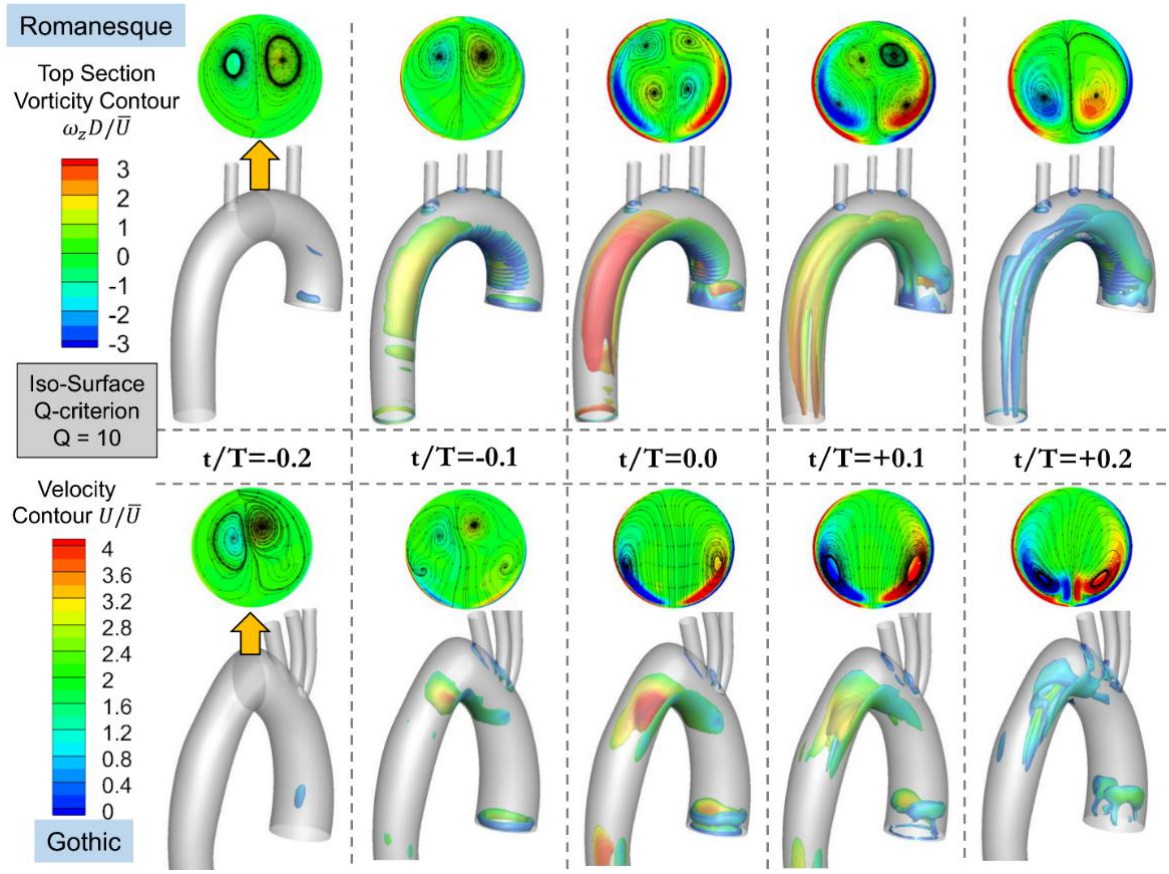

Figure 5.14. Comparison of coherent structures during the systolic period of the cycle. (CFD. Top: Romanesque; Bottom: Gothic).

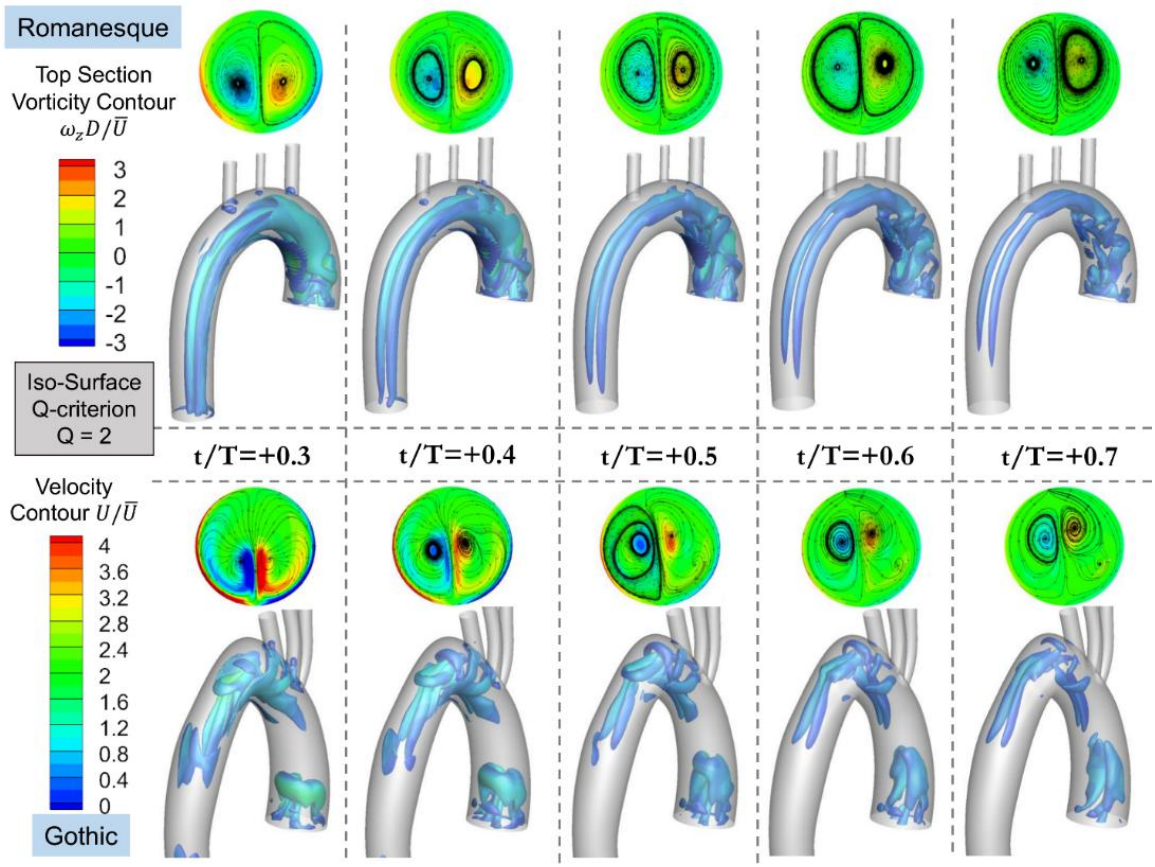

Figure 5.15. Comparison of coherent structures during the diastolic period of the cycle. (CFD. Top: Romanesque; Bottom: Gothic).

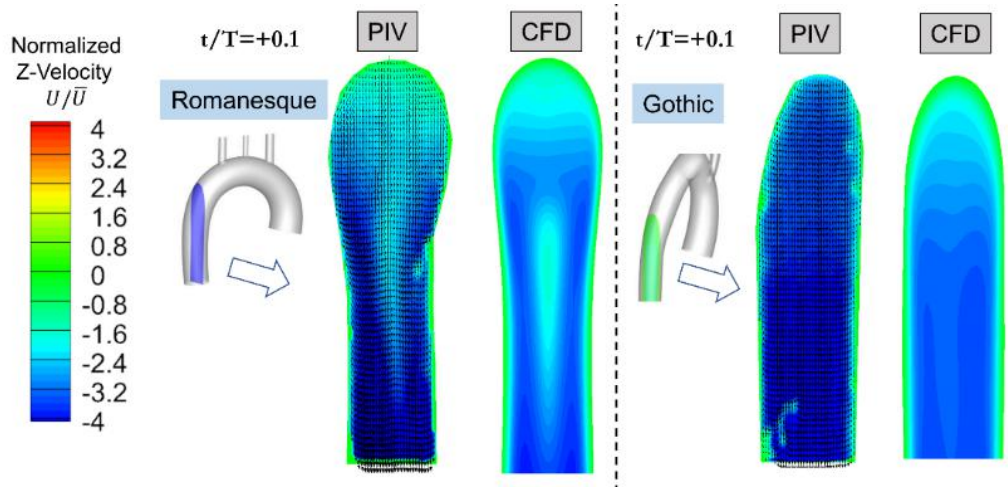

Figure 5.16. Comparison of the PIV and CFD velocity on the longitude section plane of the descending aorta (Left: Romanesque; Right: Gothic).

5.3.3. Wall Shear Stress

The distinct 3D flow patterns generate varying distributions of wall shear stress (WSS) for the two models during the systole. Figure 5.17 and Figure 5.18 display the WSS distributions from two view angles during the systolic phases for the Romanesque and Gothic arches, respectively. Figure 5.17 shows that at the phase before the peak systole (t/T = -0.1), WSS is slightly higher on the inner wall but relatively uniform on the descending aorta surface in the Romanesque model. From t/T = 0.0 to t/T = +0.1, the high WSS regions moved towards the anterior and posterior side of the wall, which was mainly caused by the formation of the pair of wall vortices in these phases. At t/T = +0.2, as the Dean-type vortices form and roll up, the inner wall sees a high WSS again relatively to the rest of the surface. Overall, the WSS distribution is relatively uniform in the axial direction throughout the systolic phases in the Romanesque model.

Figure 5.18 show that the sharp curvature of the Gothic model caused more spatial variations of WSS during the systolic phases. At t/T = -0.1, a high WSS region formed on the inner wall near the top, which was resulted from the local acceleration of the flow. At t/T = 0.0 and +0.1, high WSS regions moved to the anterior and posterior walls due to the pair of wall vortices similar to the case in the Romanesque model. But this high WSS is more localized near the arch top. Along the descending aortic wall, a local high WSS was seen on the outer wall due to the impingement of the separated jet, while the large portion of the descending wall has much lower WSS. At t/T = +0.2, a local high WSS was found on the inner surface near the top, suggesting the re-attachment of the separated jet flow from the previous phases. In this end systolic phase, the downstream of the WSS became more uniform, but the top portion of the outer wall had a very low WSS. Throughout the systolic phases, a low WSS can be seen on the top of the outer wall, which can be explained by the constantly stagnant flow shown in previous

velocity results. Overall, the Gothic arch exhibits more temporal and spatial variations of WSS during the systolic phases, implying a tendency of potential hemodynamic complications.

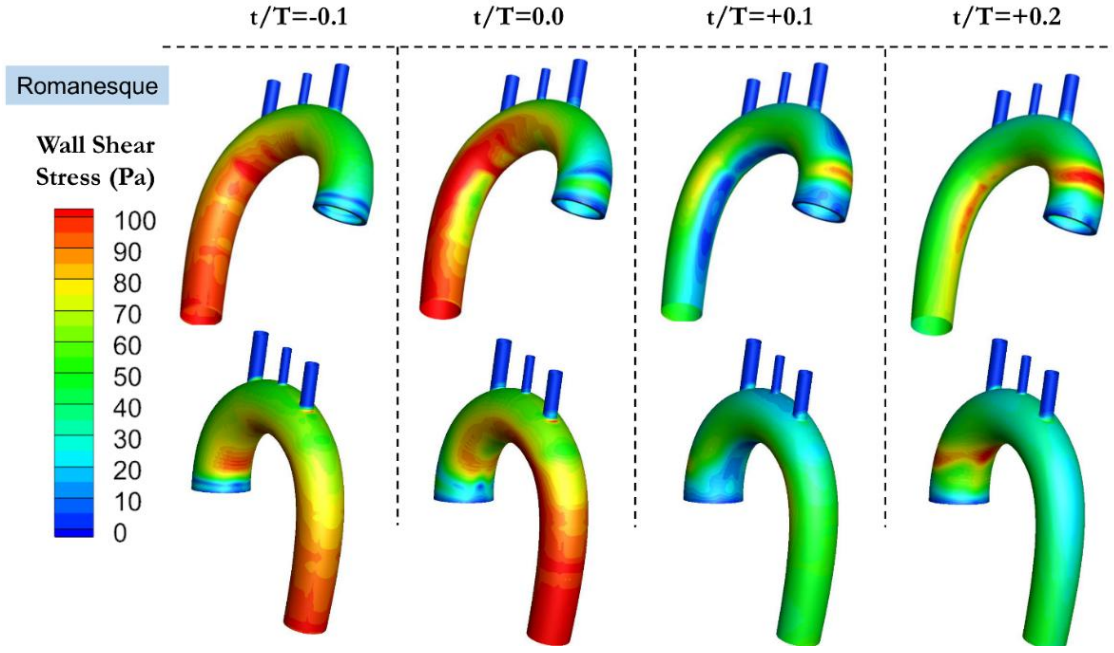

Figure 5.17. Distribution of wall shear stress of the Romanesque model (two view angles) during the systole (CFD).

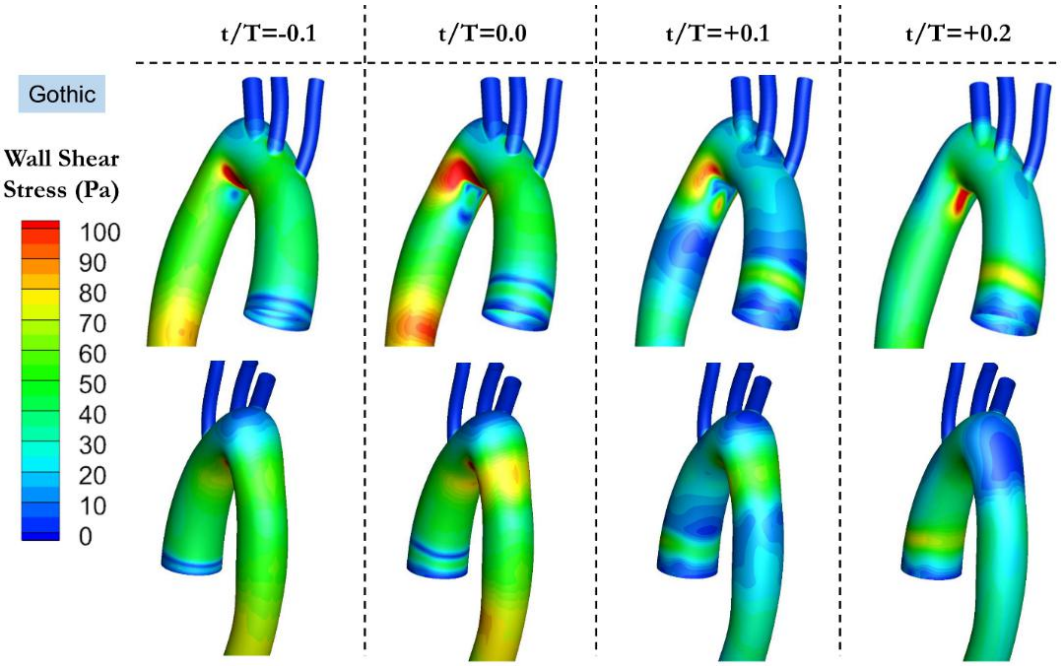

Figure 5.18. Distribution of wall shear stress of the Gothic model (two view angles) during the systole (CFD).

5.4. Discussion

Blood flow through a normal aortic arch resembles the classic Dean flow in a smooth 180-degree curved tube [202]. Steady Dean flow exhibits a strong secondary flow motion in the radial direction superimposed to the primary axial flow, resulting in overall helical streamlines. This effect is caused the curvature-induced centrifugal force. Dean flows are often recognized by the counter-rotating vortex systems in the cross-sectional plane, whose pattern is strongly dependent on the dimensionless Dean number, defined as the ratio of between the inertial and centripetal forces and the viscous forces (Eq. 5.11),

$$De = \sqrt{d/2R_C}Re \tag{5.11}$$

where d is the diameter of the tube, R_C is the radius of curvature. Generally, when De is extremely small, the secondary flow effect is very weak. As De increases, the secondary vortices develop due to the Dean instability. When De is very high, the Dean vortices get unstable and the flow becomes fully turbulent when De > 400 [203].

In aortic arch hemodynamics, the flow is further complicated by the pulsatile condition and non-uniform curvature. Previous studies of pulsatile flow in curved pipes suggested that the coherent vortical structures are most evident near the peak flow and immediately after the peak, while a loss of coherence occurs during the deceleration phases (diastole) [204], [205]. Our results from the Romanesque model (Figure 5.7 A-D) suggest a similar trend of formations of the wall vortex pairs and the Dean-type vortices starting the peak systole phase. Our results also show that the Dean-type vortex structure is continuously extended into the descending aorta and persists throughout the deceleration phases, even when the flow diminishes during the diastole. The relatively less spatial variation of the coherent structures contributes to a more uniform WSS

distribution on the Romanesque aortic wall throughout the cycle. These secondary flow characteristics are also consistent with the previous findings from CFD studies [84].

Our results also suggest that both primary and secondary flow characteristics are significantly altered by the Gothic geometry. Although the critical Dean number is not established in this study, it is certain that the De number of the Gothic model is considerably higher than that of the Romanesque model due to the small radius of the curvature (R_C) at the sharp corner. Hence, a stable pair of Dean-type vortices were not observed in the Gothic model. A pair of wall vortices were generated close to the inner wall due to the flow acceleration around the corner near the peak systole. Such vortices were less continuous and were not observed in the main portion of the descending aorta. The lack of coherent structures in the Gothic model is consistent with clinical findings by Frydrychowicz et al. [93], which suggest the helical structures were less common in patients with altered arch geometries. Furthermore, our results reveal stagnant flow near the top, flow separation and impingement on the descending aortic wall at the peak systole, and a re-attachment of the flow during the deceleration phases. The local high WSS on the outer wall of the descending aorta agrees well with the finding in Olivieri et al. [95], where the maximum after the isthmus. These unique flow characteristics as well as spatially and temporally non-uniform WSS distributions imply a potential explanation for late morbidity in patients with Gothic arch after CoA repair.

Although the pathological mechanisms of WSS effects on aortic diseases remains to be fully understood, a large body of evidence have shown that the hemodynamic forces can trigger vascular endothelial cell responses and modulate the molecular expressions [206]-[208]. Low and oscillatory WSS is predisposed to the progression of atherosclerosis lesions [93], [209], [210], which further affects the aortic distensibility and compliance [211]. These factors might

directly contribute to the late systemic hypertension in Gothic patients after surgical repair of CoA [45]. Clinical studies also indicate that development of hypertension might be linked with the long-term presence of abnormal helical flow structures in the descending aorta of the Gothic arch patients [42]. Our results confirm that the Gothic arch exhibits abnormal vortical flow structures and causes local low WSS regions and less uniformity throughout the cycle compared with the Romanesque arch, which highlights the importance for the assessment of deformed arch geometry for patients after CoA repairs.

5.5. Conclusions

A combined experimental and computational fluid dynamic study has been conducted to characterize the pulsatile flow in two different deformed aortic arches, i.e., Romanesque and Gothic models. For the experiment, an in vitro pulsatile flow simulator has been used and the flow was quantified by phase-locked planar Particle image velocimetry (PIV) and tomographic PIV measurements. CFD simulations have also been conducted for the same arch models to reveal time-resolved 3D flow characteristics. The pressure and flow waveforms were generated using a programmable pump and the flow condition mimics the aortic flow with a cardiac output of 5 L/min and a heart rate of 60 bpm.

The results revealed significantly different primary and secondary flow characteristics between the two models. In the Romanesque model, the flow velocity is high near the inner wall of the arch at the peak systole, but becomes relatively uniform across the section during the deceleration phases due to the effect of secondary flow. A pair of wall vortices and Dean-type vortices develop during the systole, and the Dean-type vortical structure is continuous into the descending aorta and remains intact during the diastole. On the other hand, the Gothic arch exhibits a high velocity skewed towards the inner wall of the arch top consistently throughout the

systolic phases. Flow separates from the sharp corner and impinges on the outer wall of the descending aorta immediately downstream. A constantly stagnate flow region was seen near the outer wall of the arch top. While a pair of wall vortices generated, typical Dean-type vortices were not observed in the Gothic model after the peak systole. Coherent are less continues in the descending portion of the Gothic arch. The distinct flow characteristics cause more variations of wall shear stress distributions on the descending arch walls of the Gothic model both spatially and temporally. Low and oscillatory WSS and the abnormal secondary flow in the Gothic arch are correlated to vascular endothelial cell remodeling and might provide hints to the increased risks of atherosclerosis, late systemic hypertension, and other common cardiovascular complications for patients with the Gothic arches after the coarctation of the aorta repair.

6. CONCLUSION AND RECOMMENDATIONS

6.1. Summary of Research Findings

1) An in vitro cardiovascular flow simulator with PIV system was designed and constructed to simulate and study the physiological conditions of realistic aortic pulsatile flow to further study the aortic problems.

2) Turbulent flow characteristics and structural deformation of an intact silicone aortic root model under different cardiac outputs were studied employing PIV technique. The results demonstrated that the distributions of the jet flow structures significantly varies at different phases of a cardiac cycle. A reduction in cardiac outputs resulted in a lower post-systolic turbulence, smaller circumferential deformation, a smaller geometric orifice area, and a shortened valve-opening period.

3) The characteristics of pulsatile flow past stenotic aortic valve models with moderate and severe stenosis have been studied under varied physiological conditions using PIV method. The PIV results suggested the severe prosthetic stenosis resulted in a two-fold increase in peak jet velocity and a three-fold increase in peak TKE compared to the moderate stenosis case. Both valves introduced significantly higher turbulence after the peak systole than the no-valve baseline case, underscoring the important role of leaflet stiffness in the turbulence generation. Overall, the hemodynamic changes, including eccentric jet, increased jet velocity, and elevated turbulence and viscous shear stress, were associated with the stiffened leaflet materials, rather than the use of the stent base structure.

4) Pulsatile flow characteristics of a Romanesque and a Gothic aortic arch model were investigated and compared based on PIV measurements and CFD simulations. In the Romanesque model, the flow velocity was high near the inner wall of the arch at the peak systole,

but became relatively uniform across the section during the deceleration phases due to the effect of secondary flow. A pair of wall vortices and Dean-type vortices developed during the systole, and the Dean-type vortical structure was continuous into the descending aorta. On the other hand, the Gothic arch exhibited a high velocity skewed towards the inner wall of the arch top consistently throughout the systolic phases. Flow separated from the sharp corner and impinged on the outer wall of the descending aorta immediately downstream. Low and oscillatory WSS and the abnormal secondary flow in the Gothic arch were correlated to vascular endothelial cell remodeling and might provide hints to the increased risks of atherosclerosis, late systemic hypertension, and other common cardiovascular complications for patients with the Gothic arches after the CoA repair.

6.2. Limitations

Due to the nature of current research and capability of our in-vitro experimental setup, these studies have a few limitations:

1) The silicone aortic models were simplified and smoothed and do not replicate the non-linear viscoelastic tissue properties, and the use of the same silicone materials for both the aortic wall and the leaflets does not reflect the real histological differences of the different tissues.

2) The silicone aortic arch models studied in the experiment were constructed relatively smoothly with key dimensions from clinical database. Realistic aortic arch geometries vary from patient to patient and might exhibits more complicated global characteristics such as twist and bending as well as local complex wall topology. The brachiocephalic, carotid, subclavian vessel branches on the top of the arch were blocked at their ends in both experimental and computational models. This helped reduce the experimental uncertainty that might be caused by

the uncontrolled branch outlet pressures (which requires additional flow loop to control) and focused our study on the main flow in the ascending and descending aorta.

3) In vitro fluid dynamic experiment has its intrinsic limitations because of its hemodynamic and physiological simplifications. The simulator generated smooth pulsatile flows using a Newtonian fluid mixture (glycerin-water) as surrogate fluid, which did not fully represent the real blood properties. Although this working fluid was used in most previous experimental works and it did not change the overall flow characteristics as the Re number of the systolic flow is relatively high, the decaying flow during diastole might slightly differ if the non-Newtonian blood was considered.

4) The left ventricular hemodynamics was simulated via an LV pressure module for the purpose of tuning the pressure waveform output from the pump. While the boundary conditions were simulated, the actual physiology and geometry of the LV-aorta junction have not been considered in the present study.

5) The study was limited in terms of temporal resolution to directly quantify time-dependent variations. Both RSS and TKE evaluated in this thesis were statistical representations of the turbulence level, which did not directly quantify the real stresses at an actual spatial location within the flow.

6.3. Recommendations

1) Although tissue-based aortic prostheses are increasingly used, they are still very different from realistic biological materials. Future research can focus on exploring approaches to improve the understanding of the hemodynamics and fluid-structure interaction phenomena in more realistic biological settings.

2) The current combined experimental and computational methods used in the aortic arch models study proved the capability of such tools and provided insights into the major primary and secondary flow patterns that differentiates the Gothic arch from the Romanesque model. Future work with more sophisticated experiment flow loop designs and non-Newtonian models are highly recommended, particularly for potential patient-specific studies.

3) Although PIV techniques enable tracking the movement of flow with high temporal and spatial resolutions, their capacities are limited. For example, it is difficult to quantify the residence time of blood. Future works could focus on developing 3D time-resolved measurements to conduct Lagrangian particle tracking analysis to accurately quantify residence time of blood elements in three-dimensional volumes.

REFERENCES

[1] G. B. Ciuffo, "A Beginner's Guide to the Hearts Structure," Jul. 30, 2021. [Online]. Available:https://heartsurgeryinfo.com/a-beginners-guide-to-heart-anatomy/[Accessed Nov. 26, 2021].

[2] J. R. Levick, An Introduction to Cardiovascular Physiology. Butterworth-Heinemann, 2013.

[3] K. M. Wilbur and C. M. Yonge, Physiology of Mollusca: Volume II. Academic Press, 2013.

[4] "Basic Physiology for the Health Sciences by Selkurt, Ewald E. (Editor): Very Good Hardcover (1982) Second Edition. UHR Books."

[5] L. Waite and J. Fine, Applied Biofluid Mechanics. McGraw-Hill Education, 2017.

[6] S. Y. Ho, "Structure and anatomy of the aortic root," European Journal of Echocardiography, vol. 10, no. 1, Jan., pp. i3–i10, 2009.

[7] P. Mathew, "A comparison of hemodynamic performance in mechanical and biological heart valve prostheses," M. S. thesis, The University of Tennessee at Chattanooga, Chattanooga, TN, 2012.

[8] L. Mesotten et al., "Nuclear cardiology, Part I: Anatomy and function of the normal heart," Journal of Nuclear Medicine Technology, vol. 26, no. 1, Mar., pp. 4–8, 1998.

[9] D. W. Brown et al., "Sudden Unexpected Death After Balloon Valvuloplasty for Congenital Aortic Stenosis," Journal of the American College of Cardiology, vol. 56, no. 23, Nov., pp. 1939–1946, 2010.

[10] V. T. Nkomo, J. M. Gardin, T. N. Skelton, J. S. Gottdiener, C. G. Scott, and M. Enriquez-Sarano, "Burden of valvular heart diseases: a population-based study," The Lancet, vol. 368, no. 9540, Sep., pp. 1005–1011, 2006.

[11] E. Falk, "Coronary thrombosis: Pathogenesis and clinical manifestations," The American Journal of Cardiology, vol. 68, no. 7, Sep., pp. B28–B35, 1991.

[12] Otto Catherine M. et al., "Prospective study of asymptomatic valvular aortic stenosis," Circulation, vol. 95, no. 9, May, pp. 2262–2270, 1997.

[13] V. Nguyen et al., "Haemodynamic and anatomic progression of aortic stenosis," Heart, vol. 101, no. 12, Jun., pp. 943–947, 2015.

[14] K. Maganti, V. H. Rigolin, M. E. Sarano, and R. O. Bonow, "Valvular heart disease: diagnosis and management," Mayo Clinic Proceedings, vol. 85, no. 5, May, pp. 483–500, 2010.

[15] A. Walker, "In vitro evaluation of mechanical heart valve performance using a novel test chamber in an automated mock circulatory loop," M. S. thesis, Virginia Commonwealth University, Richmond, VA, 2010.

[16] P. Bloomfield, "Choice of heart valve prosthesis," Heart, vol. 87, no. 6, Jun., pp. 583–589, 2002.

[17] H. Nygaard et al., “Two-dimensional color-mapping of turbulent shear stress distribution downstream of two aortic bioprosthetic valves in vitro,” Journal of Biomechanics, vol. 25, no. 4, Apr., pp. 429–440, 1992.

[18] H. Nygaard, P. K. Paulsen, J. M. Hasenkam, E. M. Pedersen, and P. E. Rovsing, “Turbulent stresses downstream of three mechanical aortic valve prostheses in human beings,” The Journal of Thoracic and Cardiovascular Surgery, vol. 107, no. 2, Feb., pp. 438–446, 1994.

[19] C.-P. Li, C.-W. Lo, and P.-C. Lu, “Estimation of viscous dissipative stresses induced by a mechanical heart valve using PIV data,” Annals of Biomedical Engineering, vol. 38, no. 3, Mar., pp. 903–916, 2010.

[20] S. J. Head, M. Çelik, and A. P. Kappetein, “Mechanical versus bioprosthetic aortic valve replacement,” European Heart Journal, vol. 38, no. 28, Jul., pp. 2183–2191, 2017.

[21] A. P. Yoganathan, Z. He, and S. C. Jones, “Fluid mechanics of heart valves,” Annual Review of Biomedical Engineering, vol. 6, no. 1, pp. 331–362, 2004.

[22] P. Sidhu et al., “Mechanical or bioprosthetic valves in the elderly: a 20-year comparison,” The Annals of Thoracic Surgery, vol. 71, no. 5, May, pp. S257–S260, 2001.

[23] H. L. Leo, L. P. Dasi, J. Carberry, H. A. Simon, and A. P. Yoganathan, “Fluid dynamic assessment of three polymeric heart valves using particle image velocimetry,” Annals of Biomedical Engineering, vol. 34, no. 6, Jun., pp. 936–952, 2006.

[24] M. Valente, M. Minarini, A. F. Maizza, U. Bortolotti, and G. Thiene, “Heart valve bioprosthesis durability: a challenge to the new generation of porcine valves,” European Journal of Cardio-thoracic Surgery, vol. 6 Suppl 1, pp. S82-90, 1992.

[25] E. Braunwald, R. L. Frye, M. M. Aygen, and J. W. Gilbert, “Studies on Starling's law of the heart. III. Observations in patients with mitral stenosis and atrial fibrillation on the relationships between left ventricular end-diastolic segment length, filling pressure, and the characteristics of ventricular contraction,” The Journal of Clinical Investigation, vol. 39, no. 12, Dec., pp. 1874–1884, 1960.

[26] R. L. Frye, E. Braunwald, and E. R. Cohen, “Studies on Starling's law of the heart. I. The circulatory response to acute hypervolemia and its modification by ganglionic blockade,” The Journal of Clinical Investigation, vol. 39, no. 7, Jul., pp. 1043–1050, 1960.

[27] Roe Benson B., Kelly Paul B., Myers John L., and Moore David W., “Tricuspid leaflet aortic valve prosthesis,” Circulation, vol. 33, no. 4s1, Apr., p. I–124, 1966.

[28] Y. H. Kuan, L. P. Dasi, A. Yoganathan, and H. L. Leo, “Recent advances in polymeric heart valves research,” International Journal of Biomaterials Research and Engineering, vol. 1, no. 1, pp. 1–17, 2011.

[29] A. Maton, Human biology and health. Englewood Cliffs, NJ: Prentice Hall, 1997.

[30] R. Erbel et al., “Diagnosis and management of aortic dissection,” European Heart Journal, vol. 22, no. 18, Sep., pp. 1642–1681, 2001.

[31] R. Erbel and H. Eggebrecht, “Aortic dimensions and the risk of dissection,” Heart, vol. 92, no. 1, Jan., pp. 137–142, 2006.

[32] A. Evangelista et al., “Echocardiography in aortic diseases: EAE recommendations for clinical practice,” European Journal of Echocardiography, vol. 11, no. 8, Sep., pp. 645–658, 2010.

[33] OER Services, “Circulatory Pathways | Anatomy and Physiology II.” [Online]. Available:https://courses.lumenlearning.com/suny-ap2/chapter/circulatory-pathways/. [Accessed May 20, 2021].

[34] D. N. Ku, “Blood flow in arteries,” Annual Review of Fluid Mechanics. vol. 29, no. 1, Jan., pp. 399–434, 1997.

[35] K. W. Johnston, R. B. Rutherford, M. D. Tilson, D. M. Shah, L. Hollier, and J. C. Stanley, “Suggested standards for reporting on arterial aneurysms,” Journal of Vascular Surgery, vol. 13, no. 3, Mar., pp. 452–458, 1991.

[36] P. Hagan et al., “The international registry of acute aortic dissection (IRAD): new insights into an old disease,” JAMA, vol. 283, Feb., pp. 897–903, 2000.

[37] A. White, J. Broder, J. Mando-Vandrick, J. Wendell, and J. Crowe, “Acute aortic emergencies—Part 2 aortic dissections,” Advanced Emergency Nursing Journal, vol. 35, no. 1, Mar., pp. 28–52, 2013.

[38] F. J. Criado, “Aortic dissection: a 250-year perspective,” Texas Heart Institute Journal, vol. 38, no. 6, pp. 694–700, 2011.

[39] de Divitiis Marcello et al., “Vascular dysfunction after repair of coarctation of the aorta,” Circulation, vol. 104, no. Suppl I, Sep., pp. I–165–I–170, 2001.

[40] M. Cohen, V. Fuster, P. M. Steele, D. Driscoll, and D. C. McGoon, “Coarctation of the aorta. Long-term follow-up and prediction of outcome after surgical correction,” Circulation, vol. 80, no. 4, Oct., pp. 840–845, 1989.

[41] G. Webb, “Treatment of coarctation and late complications in the adult,” Seminars in Thoracic and Cardiovascular Surgery, vol. 17, no. 2, Jun., pp. 139–142, 2005.

[42] M. D. Hope et al., “Clinical evaluation of aortic coarctation with 4D flow MR imaging,” Journal of Magnetic Resonance Imaging, vol. 31, no. 3, pp. 711–718, 2010.

[43] J. M. Oliver, P. Gallego, A. Gonzalez, A. Aroca, M. Bret, and J. M. Mesa, “Risk factors for aortic complications in adults with coarctation of the aorta,” Journal of the American College of Cardiology, vol. 44, no. 8, Oct., pp. 1641–1647, 2004.

[44] J. W. J. Vriend and B. J. M. Mulder, “Late complications in patients after repair of aortic coarctation: implications for management,” International Journal of Cardiology, vol. 101, no. 3, Jun., pp. 399–406, 2005.

[45] L. Donazzan, R. Crepaz, J. Stuefer, and G. Stellin, “Abnormalities of aortic arch shape, central aortic flow dynamics, and distensibility predispose to hypertension after successful repair of aortic coarctation,” World Journal for Pediatric and Congenital Heart Surgery, vol. 5, no. 4, Oct., pp. 546–553, 2014.

[46] D. S. Celermajer, “Survivors of coarctation repair: fixed but not cured,” Heart, vol. 88, no. 2, Aug., pp. 113–114, 2002.

[47] S. K. Dahl, “Numerical Simulations of Blood Flow in the Left Side of the Heart,” Ph.D. thesis, Norwegian University of Science and Technology, Trondheim, Norway, 2012.

[48] K. P. Shung, R. A. Sigelmann, and G. Schmer, “Ultrasonic measurement of blood coagulation time,” IEEE Transactions on Biomedical Engineering, vol. BME-22, no. 4, Jul., pp. 334–337, 1975.

[49] P. W. Rand, E. Lacombe, H. E. Hunt, and W. H. Austin, “Viscosity of normal human blood under normothermic and hypothermic conditions,” Journal of Applied Physiology, vol. 19, no. 1, Jan., pp. 117–122, 1964.

[50] G. J. Tortora and B. H. Derrickson, Principles of Anatomy and Physiology, 13th Edition. John Wiley & Sons, 2018.

[51] L. Ge, H.-L. Leo, F. Sotiropoulos, and A. P. Yoganathan, “Flow in a mechanical bileaflet heart valve at laminar and near-peak systole flow rates: CFD simulations and experiments,” Journal of Biomechanical Engineering, vol. 127, no. 5, Oct., pp. 782–797, 2005.

[52] E.-B. Shim and K.-S. Chang, “Numerical analysis of three-dimensional Bjo¨rk–Shiley valvular flow in an aorta,” Journal of Biomechanical Engineering, vol. 119, no. 1, Feb., pp. 45–51, 1997.

[53] L. P. Dasi, L. Ge, H. A. Simon, F. Sotiropoulos, and A. P. Yoganathan, “Vorticity dynamics of a bileaflet mechanical heart valve in an axisymmetric aorta,” Physics of Fluids, vol. 19, no. 6, Jun., pp. 067105, 2007.

[54] Y. Shi, Y. Zhao, T. J. H. Yeo, and N. H. C. Hwang, “Numerical simulation of opening process in a bileaflet mechanical heart valve under pulsatile flow condition,” Journal of Heart Valve Disease, vol. 12, no. 2, Mar., pp. 245–255, 2003.

[55] S. G. D. Kelly, “Computational fluid dynamics insights in the design of mechanical heart valves,” Artificial Organs, vol. 26, no. 7, Jul., pp. 608–613, 2002.

[56] B. M. Yun et al., “A numerical investigation of blood damage in the hinge area of aortic bileaflet mechanical heart valves during the leakage phase,” Annals of Biomedical Engineering, vol. 40, no. 7, Jul., pp. 1468–1485, 2012.

[57] J. D. Hart, G. W. M. Peters, P. J. G. Schreurs, and F. P. T. Baaijens, “A three-dimensional computational analysis of fluid–structure interaction in the aortic valve,” Journal of Biomechanics, vol. 36, no. 1, Jan., pp. 103–112, 2003.

[58] K. Cao, M. BukaČ, and P. Sucosky, “Three-dimensional macro-scale assessment of regional and temporal wall shear stress characteristics on aortic valve leaflets,” Computer Methods in Biomechanics and Biomedical Engineering, vol. 19, no. 6, Apr., pp. 603–613, 2016.

[59] G. Marom, R. Haj-Ali, E. Raanani, H.-J. Schäfers, and M. Rosenfeld, “A fluid–structure interaction model of the aortic valve with coaptation and compliant aortic root,” Medical & Biological Engineering & Computing, vol. 50, no. 2, Feb., pp. 173–182, 2012.

[60] R. Haj-Ali, L. P. Dasi, H.-S. Kim, J. Choi, H. W. Leo, and A. P. Yoganathan, “Structural simulations of prosthetic tri-leaflet aortic heart valves,” Journal of Biomechanics, vol. 41, no. 7, Jan., pp. 1510–1519, 2008.

[61] M. R. Labrosse, K. Lobo, and C. J. Beller, “Structural analysis of the natural aortic valve in dynamics: From unpressurized to physiologically loaded,” Journal of Biomechanics, vol. 43, no. 10, Jul., pp. 1916–1922, 2010.

[62] S. Krucinski, I. Vesely, M. A. Dokainish, and G. Campbell, “Numerical simulation of leaflet flexure in bioprosthetic valves mounted on rigid and expansile stents,” Journal of Biomechanics, vol. 26, no. 8, Aug., pp. 929–943, 1993.

[63] D. Kamensky et al., “An immersogeometric variational framework for fluid-structure interaction: application to bioprosthetic heart valves,” Computer Methods in Applied Mechanics and Engineering, vol. 284, Feb., pp. 1005–1053, 2015.

[64] M. C. Hsu, D. Kamensky, Y. Bazilevs, M. S. Sacks, and T. J. R. Hughes, “Fluid–structure interaction analysis of bioprosthetic heart valves: Significance of arterial wall deformation,” Computational Mechanics, vol. 54, no. 4, Oct., pp. 1055–1071, 2014.

[65] V. B.Makhijani, H. Q. Yang, P. J. Dionne, and M. J. Thubrikar, “Three-dimensional coupled fluid-structure simulation of pericardial bioprosthetic aortic valve function.,” ASAIO Journal (American Society for Artificial Internal Organs: 1992), vol. 43, no. 5, Sep., pp. M387-92, 1997.

[66] P. Midha, V. Raghav, I. Okafor, and A. Yoganathan, “The effect of valve-in-valve implantation height on sinus flow,” Annals of Biomedical Engineering, vol. 45, May 2016.

[67] W. L. Lim, Y. T. Chew, T. C. Chew, and H. T. Low, “Steady flow dynamics of prosthetic aortic heart valves: a comparative evaluation with PIV techniques,” Journal of Biomechanics, vol. 31, no. 5, May, pp. 411–421, 1998.

[68] A. Balducci et al., “Investigation of the flow field downstream of an artificial heart valve by means of PIV and PTV,” Experiments in Fluids, vol. 36, no. 1, Jan., pp. 204–213, 2004.

[69] A. Bellofiore and N. J. Quinlan, “High-resolution measurement of the unsteady velocity field to evaluate blood damage induced by a mechanical heart valve,” Annals of Biomedical Engineering, vol. 39, no. 9, Sep., pp. 2417–2429, 2011.

[70] D. Garcia, P. Pibarot, J. G. Dumesnil, F. Sakr, and L. G. Durand, “Assessment of aortic valve stenosis severity: A new index based on the energy loss concept,” Circulation, vol. 101, no. 7, Feb., pp. 765–771, 2000.

[71] R. S. Heinrich et al., “Experimental analysis of fluid mechanical energy losses in aortic valve stenosis: Importance of pressure recovery,” Annals of Biomedical Engineering, vol. 24, no. 6, Nov., pp. 685–694, 1996.

[72] M. Ismail, F. Kabinejadian, Y. N. Nguyen, E. Tay Lik Wui, S. Kim, and H. L. Leo, “Hemodynamic assessment of extra-cardiac tricuspid valves using particle image velocimetry,” Medical Engineering & Physics, vol. 50, Dec., pp. 1–11, 2017.

[73] E. M. Groves, A. Falahatpisheh, J. L. Su, and A. Kheradvar, “The effects of positioning of transcatheter aortic valve on fluid dynamics of the aortic root,” ASAIO journal (American Society for Artificial Internal Organs: 1992), vol. 60, no. 5, pp. 545–552, 2014.

[74] P. S. Gunning, N. Saikrishnan, L. M. McNamara, and A. P. Yoganathan, “An in vitro evaluation of the impact of eccentric deployment on transcatheter aortic valve

hemodynamics," Annals of Biomedical Engineering, vol. 42, no. 6, Jun., pp. 1195–1206, 2014.

[75] D. Hasler, A. Landolt, and D. Obrist, "Tomographic PIV behind a prosthetic heart valve," Experiments in Fluids, vol. 57, no. 5, May, 2016.

[76] A. H. de F. Avelar, M. A. G. E. Stófel, G. D. Vieira, J. A. Canestri, and R. Huebner, "Analysis of leaflet flutter in biological prosthetic heart valves using PIV measurements," Acta Scientiarum. Technology, vol. 42, pp. e41746–e41746, 2020.

[77] W. L. Lim, Y. T. Chew, T. C. Chew, and H. T. Low, "Pulsatile flow studies of a porcine bioprosthetic aortic valve in vitro: PIV measurements and shear-induced blood damage," Journal of Biomechanics, vol. 34, no. 11, Nov., pp. 1417–1427, 2001.

[78] N. Saikrishnan, C. H. Yap, N. C. Milligan, N. V. Vasilyev, and A. P. Yoganathan, "In vitro characterization of bicuspid aortic valve hemodynamics using particle image velocimetry," Annals of Biomedical Engineering, vol. 40, no. 8, Aug., pp. 1760–1775, 2012.

[79] R. Toninato, J. Salmon, F. M. Susin, A. Ducci, and G. Burriesci, "Physiological vortices in the sinuses of Valsalva: An in vitro approach for bio-prosthetic valves," Journal of Biomechanics, vol. 49, no. 13, Sep., pp. 2635–2643, 2016.

[80] K. Dellimore, I. Kemp, R. Rodriguez, and C. Scheffer, "In vitro characterization of an aortic bioprosthetic valve using Doppler echocardiography and qualitative flow visualization," In 2012 Annual International Conference of the IEEE Engineering in Medicine and Biology Society, Aug., 2012, pp. 6641–6644.

[81] D. N. Ku, D. P. Giddens, C. K. Zarins, and S. Glagov, "Pulsatile flow and atherosclerosis in the human carotid bifurcation. Positive correlation between plaque location and low oscillating shear stress," Arteriosclerosis: An Official Journal of the American Heart Association, Inc., vol. 5, no. 3, Jun., pp. 293–302, 1985.

[82] E. P. Efstathopoulos, G. Patatoukas, I. Pantos, O. Benekos, D. Katritsis, and N. L. Kelekis, "Measurement of systolic and diastolic arterial wall shear stress in the ascending aorta," Physica Medica, vol. 24, no. 4, Dec., pp. 196–203, 2008.

[83] P. J. Kilner, G. Z. Yang, R. H. Mohiaddin, D. N. Firmin, and D. B. Longmore, "Helical and retrograde secondary flow patterns in the aortic arch studied by three-directional magnetic resonance velocity mapping," Circulation, vol. 88, no. 5 Pt 1, Nov., pp. 2235–2247, 1993.

[84] N. Shahcheraghi, H. A. Dwyer, A. Y. Cheer, A. I. Barakat, and T. Rutaganira, "Unsteady and three-dimensional simulation of blood flow in the human aortic arch," Journal of Biomechanical Engineering, vol. 124, no. 4, Jul., pp. 378–387, 2002.

[85] H. Fujioka and K. Tanishita, "Computational fluid mechanics of the blood flow in an aortic vessel with realistic geometry," In Clinical Application of Computational Mechanics to the Cardiovascular System. Tokyo: Springer Japan, 2000, pp. 99–117.

[86] S. Miyazaki et al., "Validation of numerical simulation methods in aortic arch using 4D flow MRI," Heart Vessels, vol. 32, no. 8, Aug., pp. 1032–1044, 2017.

[87] M. Nakamura, S. Wada, and T. Yamaguchi, “Computational analysis of blood flow in an integrated model of the left ventricle and the aorta,” Journal of Biomechanical Engineering, vol. 128, no. 6, Apr., pp. 837–843, 2006.

[88] U. Morbiducci, R. Ponzini, D. Gallo, C. Bignardi, and G. Rizzo, “Inflow boundary conditions for image-based computational hemodynamics: Impact of idealized versus measured velocity profiles in the human aorta,” Journal of Biomechanics, vol. 46, no. 1, Jan. pp. 102–109, 2013.

[89] S. Jin, J. Oshinski, and D. P. Giddens, “Effects of wall motion and compliance on flow patterns in the ascending aorta,” Journal of Biomechanical Engineering, vol. 125, no. 3, Jun., pp. 347–354, 2003.

[90] D. Hardman, S. I. Semple, J. M. J. Richards, and P. R. Hoskins, “Comparison of patient-specific inlet boundary conditions in the numerical modelling of blood flow in abdominal aortic aneurysm disease,” International Journal for Numerical Methods in Biomedical Engineering, vol. 29, no. 2, Feb., pp. 165–178, 2013.

[91] H. H. Yeh, S. W. Rabkin, and D. Grecov, “Hemodynamic assessments of the ascending thoracic aortic aneurysm using fluid-structure interaction approach,” Medical & Biological Engineering & Computing, vol. 56, no. 3, Mar., pp. 435–451, 2018.

[92] E. K. Shang et al., “Peak wall Stress predicts expansion rate in descending thoracic aortic aneurysms,” The Annals of Thoracic Surgery, vol. 95, no. 2, Feb., pp. 593–598, 2013.

[93] A. Frydrychowicz et al., “Interdependencies of aortic arch secondary flow patterns, geometry, and age analysed by 4-dimensional phase contrast magnetic resonance imaging at 3 Tesla,” European Radiology, vol. 22, no. 5, May, pp. 1122–1130, 2012.

[94] M. Szopos et al., “Computational modeling of blood flow in the aorta—insights into eccentric dilatation of the ascending aorta after surgery for coarctation,” The Journal of Thoracic and Cardiovascular Surgery, vol. 148, no. 4, Oct., pp. 1572–1582, 2014.

[95] L. J. Olivieri, D. A. de Zélicourt, C. M. Haggerty, K. Ratnayaka, R. R. Cross, and A. P. Yoganathan, “Hemodynamic modeling of surgically repaired coarctation of the aorta,” Cardiovascular Engineering and Technology, vol. 2, no. 4, Dec., pp. 288–295, 2011.

[96] T. B. Le, D. R. Troolin, D. Amatya, E. K. Longmire, and F. Sotiropoulos, “Vortex Phenomena in Sidewall Aneurysm Hemodynamics: Experiment and Numerical Simulation,” Annals Biomedical Engineering, vol. 41, no. 10, Oct., pp. 2157–2170, 2013.

[97] V. Deplano, C. Guivier-Curien, and E. Bertrand, “3D analysis of vortical structures in an abdominal aortic aneurysm by stereoscopic PIV,” Experiments in Fluids, vol. 57, no. 11, Nov., p. 167, 2016.

[98] G. Rosenberg, W. M. Phillips, D. L. Landis, and W. S. Pierce, “Design and evaluation of the Pennsylvania State University mock circulatory system,” ASAIO journal (American Society for Artificial Internal Organs : 1992), vol. 4, no. 2, Jan., pp. 41–49, 1981.

[99] S. Deutsch, J. M. Tarbell, K. B. Manning, G. Rosenberg, and A. A. Fontaine, “Experimental fluid mechanics of pulsatile artificial blood pumps,” Annual Review of Fluid Mechanics, vol. 38, no. 1, pp. 65–86, 2006.

[100] Z. Ritchie, “Particle Image Velocimetry Design & Installation,” B. S. thesis, University of Arkansas, Fayetteville, AR, 2016.

[101] M. Raffel, C. E. Willert, F. Scarano, C. J. Kähler, S. T. Wereley, and J. Kompenhans, Particle Image Velocimetry: A Practical Guide. Springer, 2018.

[102] J. E. Geusic, H. M. Marcos, and L. G. Van Uitert, “Laser oscillations in Nd ‐ doped yttrium aluminum, yttrium gallium and gadolinium garnets,” Applied Physics Letters., vol. 4, no. 10, May, pp. 182–184, 1964.

[103] Y. Amnon, Quantum Electronics, 3rd Edition, Wiley, 1991.

[104] W. Koechner, Solid-State Laser Engineering, Springer, 2013.

[105] DataRay, “Pulsed Lasers and External Trigger Mode,” Dec. 02, 2016. [Online]. Available:https://dataray.com/blogs/dataray-blog/pulsed-lasers-and-external-trigger-mode [Accessed Jun. 09, 2021].

[106] D. Dabiri, “Cross-correlation digital particle image velocimetry – A review,” Turbul. ABCM Curitiba, pp. 155–199, 2006.

[107] J. Westerweel, “Fundamentals of digital particle image velocimetry,” Measurement Science and Technology, vol. 8, no. 12, Dec., pp. 1379–1392, 1997.

[108] J. Song, B. Li, L. Chen, and X. Li, “Ultrasensitive refractive index sensor based on the resonant scattering effect between double air circular-holes on silicon waveguides,” Optics Express, vol. 21, no. 23, Nov., pp. 27796–27801, 2013.

[109] S. Kasap, H. Ruda, and Y. Boucher, Cambridge Illustrated Handbook of Optoelectronics and Photonics. Cambridge University Press, 2009.

[110] S. Wiederseiner, N. Andreini, G. Epely-Chauvin, and C. Ancey, “Refractive-index and density matching in concentrated particle suspensions: a review,” Experiments in Fluids, vol. 50, no. 5, May., pp. 1183–1206, 2011.

[111] C. Brücker, U. Steinseifer, W. Schröder, and H. Reul, “Unsteady flow through a new mechanical heart valve prosthesis analysed by digital particle image velocimetry,” Measurement Science and Technology, vol. 13, no. 7, Jul., pp. 1043–1049, 2002.

[112] K. B. Manning, V. Kini, A. A. Fontaine, S. Deutsch, and J. M. Tarbell, “Regurgitant flow field characteristics of the St. Jude bileaflet mechanical heart valve under physiologic pulsatile flow using particle image velocimetry,” Artificial Organs, vol. 27, no. 9, Sep., pp. 840–846, 2003.

[113] R. Kaminsky, S. Kallweit, H.-J. Weber, T. Claessens, K. Jozwik, and P. Verdonck, “Flow visualization through two types of aortic prosthetic heart valves using stereoscopic high-speed particle image velocimetry,” Artificial Organs, vol. 31, no. 12, Dec., pp. 869–879, 2007.

[114] J. Brunette, R. Mongrain, J. Laurier, R. Galaz, and J. C. Tardif, “3D flow study in a mildly stenotic coronary artery phantom using a whole volume PIV method,” Medical Engineering & Physics, vol. 30, no. 9, Nov., pp. 1193–1200, 2008.

[115] J. Brunette, R. Mongrain, and J. C. Tardif, “A realistic coronary artery phantom for particle image velocimetry,” Journal of Visualization, vol. 7, no. 3, Jan., pp. 241–248, 2004.

[116] N. A. Buchmann, C. Atkinson, M. C. Jeremy, and J. Soria, “Tomographic particle image velocimetry investigation of the flow in a modeled human carotid artery bifurcation,” Experiments in fluids, vol. 50, no. 4, pp. 1131–1151, 2011.

[117] F. Hegner, D. Hess, and C. Brücker, “Volumetric 3D PIV in heart valve flow,” In 11th International Symposium on Particle Image Velocimetry - PIV 15, Sep. 2015.

[118] M. Büsen et al., “Development of an in vitro PIV setup for preliminary investigation of the effects of aortic compliance on flow patterns and hemodynamics,” Cardiovascular Engineering and Technology, vol. 8, no. 3, Sep., pp. 368–377, 2017.

[119] L. Haya and S. Tavoularis, “Effects of bileaflet mechanical heart valve orientation on fluid stresses and coronary flow,” Journal of Fluid Mechanics, vol. 806, Nov., pp. 129–164, 2016.

[120] B. M. Vennemann, T. Rösgen, T. P. Carrel, and D. Obrist, “Time-resolved micro PIV in the pivoting area of the triflo mechanical heart valve,” Cardiovasc Eng Tech, vol. 7, no. 3, Sep., pp. 210–222, 2016.

[121] D. Hasler and D. Obrist, “3D flow topology behind an aortic valve prosthesis,” In 18th International Symposium on the Application of Laser and Imaging Techniques to Fluid Mechanics, Jul. 2016.

[122] F. Cozzi, G. Felisati, and M. Quadrio, “Velocity measurements in nasal cavities by means of stereoscopic PIV-preliminary tests,” In Journal of Physics: Conference Series, vol. 882, Aug., 2017, pp. 012010.

[123] Z. Lou and W. J. Yang, “A computer simulation of the non-Newtonian blood flow at the aortic bifurcation,” Journal of Biomechanics, vol. 26, no. 1, Jan., pp. 37–49, 1993.

[124] A. D. Caballero and S. Laín, “Numerical simulation of non-Newtonian blood flow dynamics in human thoracic aorta,” Computer Methods in Biomechanics and Biomedical Engineering, vol. 18, no. 11, Aug., pp. 1200–1216, 2015.

[125] A. Melling, “Tracer particles and seeding for particle image velocimetry,” Measurement Science and Technology., vol. 8, no. 12, Dec., pp. 1406–1416, 1997.

[126] J. Novotný and L. Manoch, “The criterion of choosing the proper seeding particles,” In 18th International Conference Engineering Mechanics 2012, May, 2012, pp. 945–954.

[127] M. Jahanmiri, “Particle Image Velocimetry: Fundamentals and Its Applications,” p. 58.

[128] C. Tu, Z. Yin, J. Lin, and F. Bao, “A review of experimental techniques for measuring micro- to nano-particle-laden gas flows,” Applied Sciences, vol. 7, no. 2, Feb., pp. 120, 2017.

[129] R. H. Davis and A. Acrivos, “Sedimentation of noncolloidal particles at low reynolds numbers,” Annual Review of Fluid Mechanics, vol. 17, no. 1, pp. 91–118, 1985.

[130] E. Guyon, J. P. Hulin, L. Petit, and C. D. Mitescu, Physical Hydrodynamics, 2nd Edn. Oxford University Press, 2015.

[131] D. Cromer and L. Pruisner, “Snow, rain, and the Stokes number,”.

[132] A. McNally, A. Madan, and P. Sucosky, “Morphotype-dependent flow characteristics in bicuspid aortic valve ascending aortas: a benchtop particle image velocimetry Study,” Frontiers in Physiology, vol. 8, Feb., pp. 44, 2017.

[133] F. M. Susin, S. Espa, R. Toninato, S. Fortini, and G. Querzoli, “Integrated strategy for in vitro characterization of a bileaflet mechanical aortic valve,” BioMedical Engineering Online, vol. 16, no. 1, Dec., pp. 1–14, 2017.

[134] I. Okafor, V. Raghav, J. F. Condado, P. A. Midha, G. Kumar, and A. P. Yoganathan, “Aortic regurgitation generates a kinematic obstruction which hinders left ventricular filling,” Annals of Biomedical Engineering, vol. 45, no. 5, May., pp. 1305–1314, 2017.

[135] D. Amatya, D. R. Troolin, and E. K. Longmire, “3D3C velocity measurements downstream of artificial heart valves,” In 8th International Symposium of Particle Image Velocimetry - PIV09, Aug., 2009.

[136] A. Hasan et al., “Biomechanical properties of native and tissue engineered heart valve constructs,” Journal of Biomechanics, vol. 47, no. 9, Jun., pp. 1949–1963, 2014.

[137] S. R. Kapadia et al., “5-year outcomes of transcatheter aortic valve replacement compared with standard treatment for patients with inoperable aortic stenosis (PARTNER 1): a randomised controlled trial,” The Lancet, vol. 385, no. 9986, Jun., pp. 2485–2491, 2015.

[138] Y. Wang et al., “Comparison of Flow Measurement by 4D Flow Magnetic Resonance Imaging and by Particles Image Velocimetry on Phantom of Abdominal Aortic Aneurysm,” SM Vascular Medecine, Dec., 2016.

[139] C. Y. Chen, R. Antón, M. Hung, P. Menon, E. A. Finol, and K. Pekkan, “Effects of intraluminal thrombus on patient-specific abdominal aortic aneurysm hemodynamics via stereoscopic particle image velocity and computational fluid dynamics modeling,” Journal of Biomechanical Engineering, vol. 136, no. 3, Feb., pp. 031001-031001–9, 2014.

[140] Y. Knapp and E. Bertrand, “Particle imaging velocimetry measurements in a heart simulator,” Journal of Visualization, vol. 8, no. 3, Sep., pp. 217–224, 2005.

[141] P. P. Sengupta et al., “Left ventricular isovolumic flow sequence during sinus and paced rhythms: new insights from use of high-resolution Doppler and ultrasonic digital particle imaging velocimetry,” Journal of the American College of Cardiology, vol. 49, no. 8, Feb., pp. 899–908, 2007.

[142] G. R. Hong et al., “Characterization and quantification of vortex flow in the human left ventricle by contrast echocardiography using vector particle image velocimetry,” JACC: Cardiovascular Imaging, vol. 1, no. 6, Nov., pp. 705–717, 2008.

[143] A. Falahatpisheh and A. Kheradvar, “High-speed particle image velocimetry to assess cardiac fluid dynamics in vitro: From performance to validation,” European Journal of Mechanics - B/Fluids, vol. 35, Sep., pp. 2–8, 2012.

[144] R. Asami, T. Tanaka, K. Kawabata, K. Hashiba, T. Okada, and T. Nishiyama, “Accuracy and limitations of vector flow mapping: left ventricular phantom validation using stereo particle image velocimetory,” Journal of Echocardiography, vol. 15, no. 2, Jun., pp. 57–66, 2017.

[145] S. W. Day, J. C. McDaniel, H. G. Wood, P. E. Allaire, N. Landrot, and A. Curtas, “Particle image velocimetry measurements of blood velocity in a continuous flow ventricular assist device,” ASAIO Journal, vol. 47, no. 4, Aug., pp. 406–411, 2001.

[146] M. Laumen et al., “Flow analysis of ventricular assist device inflow and outflow cannula positioning using a naturally shaped ventricle and aortic branch,” Artificial Organs, vol. 34, no. 10, Oct., pp. 798–806, 2010.

[147] K. Lavon et al., “Fluid–structure interaction models of bicuspid aortic valves: the effects of nonfused cusp angles,” Journal of Biomechanical Engineering, vol. 140, no. 3, Mar., pp. 031010, 2018.

[148] G. Pisani et al., “Role of the sinuses of Valsalva on the opening of the aortic valve,” The Journal of Thoracic and Cardiovascular Surgery, vol. 145, no. 4, Apr., pp. 999–1003, 2013.

[149] A. Salica et al., “The combined role of sinuses of Valsalva and flow pulsatility improves energy loss of the aortic valve,” European Journal of Cardio-thoracic Surgery, vol. 49, no. 4, Apr., pp. 1222–1227, 2016.

[150] V. V. Lomivorotov, S. M. Efremov, M. Y. Kirov, E. V. Fominskiy, and A. M. Karaskov, “Low-cardiac-output syndrome after cardiac surgery,” Journal of Cardiothoracic and Vascular Anesthesia, vol. 31, no. 1, Feb., pp. 291–308, 2017.

[151] V. Rao, J. Ivanov, R. D. Weisel, J. S. Ikonomidis, G. T. Christakis, and T. E. David, “Predictors of low cardiac output syndrome after coronary artery bypass,” The Journal of thoracic and cardiovascular surgery, vol. 112, no. 1, Jul., pp. 38–51, 1996.

[152] T. Bombardini et al., “Diastolic time – frequency relation in the stress echo lab: filling timing and flow at different heart rates,” Cardiovascular Ultrasound, vol. 6, Apr., pp. 1–20, 2008.

[153] R. Sarnari, R. Y. Kamal, M. K. Friedberg, and N. H. Silverman, “Doppler assessment of the ratio of the systolic to diastolic duration in normal children: relation to heart rate, age and body surface area,” Journal of the American Society of Echocardiography, vol. 22, no. 8, Aug., pp. 928–932, 2009.

[154] C. S. Chung, M. Karamanoglu, and S. J. Kovács, “Duration of diastole and its phases as a function of heart rate during supine bicycle exercise,” American Journal of Physiology-Heart and Circulatory Physiology, vol. 287, no. 5, Nov., pp. H2003-H2008, 2004.

[155] P. D. Stein and H. N. Sabbah, “Measured turbulence and its effect on thrombus formation,” Circulation Research, vol. 35, no. 4, Oct., pp. 608–614, 1974.

[156] Y. C. Fung, Biomechanics: Mechanical Properties of Living Tissues. Springer Science & Business Media, 2013.

[157] R. Trip, D. J. Kuik, J. Westerweel, and C. Poelma, “An experimental study of transitional pulsatile pipe flow,” Physics of Fluids, vol. 24, no. 1, Jan., pp. 014103, 2012.

[158] M. Borse, S. Bhushan, D. K. Walters, and G. W. Burgreen, “Numerical simulations of flow pattern and particle trajectories in feline aorta for hypertrophic cardiomyopathy heart conditions,” Engineering Applications of Computational Fluid Mechanics, vol. 12, no. 1, Jan., pp. 57–73, 2018.

[159] V. Bell et al., “Longitudinal and circumferential strain of the proximal aorta,” Journal of the American Heart Association, vol. 3, no. 6, Dec., pp. e001536, 2014.

[160] B. Moore and L. P. Dasi, “Spatiotemporal complexity of the aortic sinus vortex,” Experiments in Fluids, vol. 55, no. 7, Jul., pp. 1–12, 2014.

[161] E. Lansac et al., “A four-dimensional study of the aortic root dynamics,” European Journal of Cardio-thoracic Surgery,, vol. 22, no. 4, Oct., pp. 497–503, 2002.

[162] M. A. Clavel et al., “Validation and characterization of transcatheter aortic valve effective orifice area measured by doppler echocardiography,” JACC: Cardiovascular Imaging, vol. 4, no. 10, Oct., pp. 1053–1062, 2011.

[163] J. Soler-Soler and E. Galve, “Worldwide perspective of valve disease,” Heart, vol. 83, no. 6, Jun., pp. 721–725, 2000.

[164] B. A. Carabello and W. J. Paulus, “Aortic stenosis,” The Lancet, vol. 373, no. 9667, Mar., pp. 956–966, 2009.

[165] R. Rosenhek, “Mild and moderate aortic stenosis Natural history and risk stratification by echocardiography,” European Heart Journal, vol. 25, no. 3, Feb., pp. 199–205, 2004.

[166] J. J. Pereira, K. Balaban, M. S. Lauer, B. Lytle, J. D. Thomas, and M. J. Garcia, “Aortic valve replacement in patients with mild or moderate aortic stenosis and coronary bypass surgery,” The American Journal of Medicine, vol. 118, no. 7, Jul., pp. 735–742, 2005.

[167] P. Varadarajan, N. Kapoor, R. C. Bansal, and R. G. Pai, “Clinical profile and natural history of 453 nonsurgically managed patients with severe aortic stenosis,” The Annals of Thoracic Surgery, vol. 82, no. 6, Dec., pp. 2111–2115, 2006.

[168] C. R. Smith, L. G. Svensson, R. R. Makkar, V. H. Thourani, H. C. Herrmann, and S. J. Pocock, “Transcatheter versus surgical aortic-valve replacement in high-risk patients,” The New England Journal of Medicine,vol. 364, no. 23, Jun., pp. 2187–2198, 2011.

[169] A. P. Yoganathan, Y. R. Woo, and H. W. Sung, “Turbulent shear stress measurements in the vicinity of aortic heart valve prostheses,” Journal of Biomechanics, vol. 19, no. 6, Jan., pp. 433–442, 1986.

[170] P. G. Walker and A. P. Yoganathan, “In vitro pulsatile flow hemodynamics of five mechanical aortic heart valve prostheses,” European Journal of Cardio-thoracic Surgery, vol. 6, no. Supplement_1, Jan., pp. S113–S123, 1992.

[171] “2014 AHA/ACC Guideline for the Management of Patients With Valvular Heart Disease: Executive Summary,” pp. 53.

[172] R. Zhang and Y. Zhang, “An experimental study of pulsatile flow in a compliant aortic root model under varied cardiac outputs,” Fluids, vol. 3, no. 4, Dec., pp. 71, 2018.

[173] A. F. Stalder et al., “Assessment of flow instabilities in the healthy aorta using flow-sensitive MRI,” Journal of Magnetic Resonance Imaging, vol. 33, no. 4, Mar., pp. 839–846, 2011.

[174] R. Gorlin and S. G. Gorlin, “Hydraulic formula for calculation of the area of the stenotic mitral valve, other cardiac valves, and central circulatory shunts. I,” American Heart Journal, vol. 41, no. 1, Jan., pp. 1–29, 1951.

[175] Y. N. V. Reddy and R. A. Nishimura, “Evaluating the severity of aortic stenosis: a re-look at our current ‘gold standard’ measurements,” European Heart Journal, vol. 39, no. 28, Jul., pp. 2656–2658, 2018.

[176] R. J. Bache, Y. Wang, and J. C. Greenfield, “Left ventricular ejection time in valvular aortic stenosis,” Circulation, vol. 47, no. 3, Mar., pp. 527–533, 1973.

[177] S. Ben Zekry et al., “Flow acceleration time and ratio of acceleration time to ejection time for prosthetic aortic valve function,” JACC: Cardiovascular Imaging, vol. 4, no. 11, Nov., pp. 1161–1170, 2011.

[178] S. Gamaza-Chulián, E. Díaz-Retamino, S. Camacho-Freire, D. Ruiz-Fernández, A. Gutiérrez-Barrios, and J. Oneto-Otero, “Acceleration time and ratio of acceleration time to ejection time in aortic stenosis: new echocardiographic diagnostic parameters,” Journal of the American Society of Echocardiography, vol. 30, no. 10, Oct., pp. 947–955, 2017.

[179] M. Del Trigo et al., “Incidence, timing, and predictors of valve hemodynamic deterioration after transcatheter aortic valve replacement: multicenter registry,” Journal of the American College of Cardiology, vol. 67, no. 6, Feb., pp. 644–655, 2016.

[180] Hope Michael D. et al., “4D flow CMR in assessment of valve-related ascending aortic disease,” JACC: Cardiovascular Imaging, vol. 4, no. 7, Jul., pp. 781–787, 2011.

[181] N. Saikrishnan, L. Mirabella, and A. P. Yoganathan, “Bicuspid aortic valves are associated with increased wall and turbulence shear stress levels compared to trileaflet aortic valves,” Biomechanics and Modeling Mechanobiology, vol. 14, no. 3, Jun., pp. 577–588, 2015.

[182] A. M. Sallam and N. H. Hwang, “Human red blood cell hemolysis in a turbulent shear flow: contribution of Reynolds shear stresses,” Biorheology, vol. 21, no. 6, Dec., pp. 783–797, 1984.

[183] P. C. Lu, H. C. Lai, and J. S. Liu, “A reevaluation and discussion on the threshold limit for hemolysis in a turbulent shear flow,” Journal of Biomechanics, vol. 34, no. 10, Oct., pp. 1361–1364, 2001.

[184] L. Ge, L. P. Dasi, F. Sotiropoulos, and A. P. Yoganathan, “Characterization of hemodynamic forces induced by mechanical heart valves: Reynolds vs. viscous stresses,” Annals of Biomedical Engineering, vol. 36, no. 2, Feb., pp. 276–297, 2008.

[185] J. D. Hellums, “1993 Whitaker lecture: Biorheology in thrombosis research,” Annals of Biomedical Engineering, vol. 22, no. 5, Sep., pp. 445–455, 1994.

[186] E. S. Farag et al., “Aortic valve stenosis and aortic diameters determine the extent of increased wall shear stress in bicuspid aortic valve disease,” Journal of Magnetic Resonance Imaging, vol. 48, no. 2, Aug., pp. 522–530, 2018.

[187] Bahlmann Edda et al., “Impact of pressure recovery on echocardiographic assessment of asymptomatic aortic stenosis: a SEAS substudy,” JACC: Cardiovascular Imaging, vol. 3, no. 6, Jun., pp. 555–562, 2010.

[188] H. Ha et al., “Age-related vascular changes affect turbulence in aortic blood flow,” Frontier in Physiology, vol. 9, pp. 36, 2018.

[189] M. de Divitiis, P. Rubba, and R. Calabrò, "Arterial hypertension and cardiovascular prognosis after successful repair of aortic coarctation: a clinical model for the study of vascular function," Nutrition, Metabolism and Cardiovascular Diseases, vol. 15, no. 5, Oct., pp. 382–394, 2005.

[190] P. Ou et al., "Late systemic hypertension and aortic arch geometry after successful repair of coarctation of the aorta," European Heart Journal, vol. 25, no. 20, Oct., pp. 1853–1859, 2004.

[191] P. Ou et al., "Aortic arch shape deformation after coarctation surgery: effect on blood pressure response," The Journal of Thoracic and Cardiovascular Surgery, vol. 132, no. 5, Nov., pp. 1105–1111, 2006.

[192] P. Ou et al., "Angular (Gothic) aortic arch leads to enhanced systolic wave reflection, central aortic stiffness, and increased left ventricular mass late after aortic coarctation repair: evaluation with magnetic resonance flow mapping," The Journal of Thoracic and Cardiovascular Surgery, vol. 135, no. 1, Jan., pp. 62–68, 2008.

[193] J. L. Bruse et al., "How successful is successful? aortic arch shape after successful aortic coarctation repair correlates with left ventricular function," The Journal of Thoracic and Cardiovascular Surgery, vol. 153, no. 2, Feb., pp. 418–427, 2017.

[194] M. Büsen, T. A. S. Kaufmann, M. Neidlin, U. Steinseifer, and S. J. Sonntag, "In vitro flow investigations in the aortic arch during cardiopulmonary bypass with stereo-PIV," Journal of Biomechanics, vol. 48, no. 10, Jul., pp. 2005–2011, 2015.

[195] D. J. Forliti, P. J. Strykowski, and K. Debatin, "Bias and precision errors of digital particle image velocimetry," Experiments in Fluids, vol. 28, no. 5, May, pp. 436–447, 2000.

[196] O. Bazan and J. P. Ortiz, "Duration of systole and diastole for hydrodynamic testing of prosthetic heart valves: comparison between ISO 5840 standards and in vivo studies," Brazilian Journal of Cardiovascular Surgery, vol. 31, no. 2, Mar., pp. 171–173, 2016.

[197] Y. C. Fung, Biomechanics: Circulation. Springer Science & Business Media, 2013.

[198] F. R. Menter, "Two-equation eddy-viscosity turbulence models for engineering applications," AIAA Journal, vol. 32, no. 8, Aug., pp. 1598–1605, 1994.

[199] L. Davidson. TME 226. Class Lecture, Topic: "Fluid mechanics, turbulent flow and turbulence modeling.", Department of Mechanics and Maritime Sciences, Chalmers University of Technology, Göteborg, Sweden, Nov. 26, 2021.

[200] X. Liu, Y. Fan, and X. Deng, "Effect of spiral flow on the transport of oxygen in the aorta: a numerical study," Annals of Biomedical Engineering, vol. 38, no. 3, Mar., pp. 917–926, 2010.

[201] Z. Keshavarz-Motamed et al., "Effect of coarctation of the aorta and bicuspid aortic valve on flow dynamics and turbulence in the aorta using particle image velocimetry," Experiments in Fluids, vol. 55, no. 3, Mar., 2014.

[202] W. R. Dean, "Note on the motion of fluid in a curved pipe," Philosophical Magazine and Journal of Science, vol. 4, no. 20, Jul., pp. 208–223, 1927.

[203] P. M. Ligrani, “A Study of Dean Vortex Development and Structure in a Curved Rectangular Channel with Aspect Ratio of 40 at Dean Numbers up to 430,” Naval Postgraduate School, Monterey, California, Contractor Report ARL-CR-144, prepared for U.S. Army Research Laboratory, Jul., 1994.

[204] K. V. Bulusu, S. Hussain, and M. W. Plesniak, “Determination of secondary flow morphologies by wavelet analysis in a curved artery model with physiological inflow,” Experiments in Fluids, vol. 55, no. 11, Nov., pp. 1832, 2014.

[205] M. W. Plesniak and K. V. Bulusu, “Morphology of secondary flows in a curved pipe with pulsatile inflow,” Journal Fluids Engineering, vol. 138, no. 10, Oct., 2016.

[206] Chappell David C., Varner Signe E., Nerem Robert M., Medford Russell M., and Alexander R. Wayne, “Oscillatory shear stress stimulates adhesion molecule expression in cultured human endothelium,” Circulation Research, vol. 82, no. 5, Mar., pp. 532–539, 1998.

[207] G. Helmlinger, B. C. Berk, and R. M. Nerem, “Calcium responses of endothelial cell monolayers subjected to pulsatile and steady laminar flow differ,” Am J Physiol, vol. 269, no. 2 Pt 1, Aug., pp. C367-375, 1995.

[208] O. Traub and B. C. Berk, “Laminar shear stress: mechanisms by which endothelial cells transduce an atheroprotective force,” Arteriosclerosis, Thrombosis, and Vascular Biology, vol. 18, no. 5, May, pp. 677–685, 1998.

[209] M. J. Thubrikar and F. Robicsek, “Pressure-induced arterial wall stress and atherosclerosis,” The Annals of Thoracic Surgery, vol. 59, no. 6, Jun., pp. 1594–1603, 1995.

[210] A. Harloff et al., “In vivo assessment of wall shear stress in the atherosclerotic aorta using flow-sensitive 4D MRI,” Magnetic Resonance in Medicine, vol. 63, no. 6, Apr., pp. 1529–1536, 2010.

[211] P. F. Davies, K. A. Barbee, R. Lal, A. Robotewskyj, and M. L. Griem, “Hemodynamics and atherogenesis: endothelial surface dynamics in flow signal transduction,” Annals of the New York Academy of Sciences, vol. 748, no. 1, Jan., pp. 86–102, 1994.

APPENDIX. LIST OF PUBLICATIONS

Journal Paper Publications:

1. **R. Zhang,** Y. Zhang, "An experimental study of pulsatile flow past compliant aortic valve using particle image velocimetry," Biomedical Sciences Instrumentation, Vol. 54, no. 1, Apr., pp. 278-285, 2018.
2. **R. Zhang,** Y. Zhang, "An experimental study of pulsatile flow in a compliant aortic root model under varied cardiac outputs," Fluids, vol. 3, no. 4, Oct., pp. 71, 2018.
3. **R. Zhang,** Y. Zhang, "Effects of heart rate on the pulsatile flow characteristics of a stenotic aortic valve model: an in vitro experimental study," Journal of Fluids Engineering, vol. 142, no. 10, Oct., pp. 101205, 2020.
4. **R. Zhang,** Y. Zhang, "Experimental analysis of pulsatile flow characteristics in prosthetic aortic valve models with stenosis," Medical Engineering & Physics. vol. 79, May, pp. 10-18, 2020.
5. Yan Zhang, **Ruihang Zhang,** Nick Thomas, Al Habib Ullah, Benjamin Eichholz, Jordi Estevadeordal, Yildirim Bora Suzen, "Experimental and numerical study of pulsatile flow characteristics in Romanesque and Gothic aortic arch models", Submitted to Medical Engineering & Physics for review.

Conference Paper Publications:

1. **R. Zhang,** Y. Zhang, "Pulsatile flow characteristics in a stenotic aortic valve model: an in vitro experimental study," In ASME-JSME-KSME 2019 8th Joint Fluids Engineering Conference, Nov., 2019, vol. 59025, paper no. V001T01A019.
2. B. Eichholz, **R. Zhang,** Y. Zhang, "Diversion of pulsatile flow over a rectangular sidewall cavity using superhydrophobic mesh," In ASME 2020 Fluids Engineering Division

Summer Meeting collocated with the ASME 2020 Heat Transfer Summer Conference and the ASME 2020 18th International Conference on Nanochannels, Microchannels, and Minichannels, Oct., 2020, vol. 2, paper no. V002T03A014.

Conference Presentations:

1. **R. Zhang,** Y. Zhang, "An experimental study of pulsatile flow past compliant aortic valve using particle image velocimetry," presented at 55th Annual Rocky Mountain Bioengineering Symposium 2018, Fargo, ND, US, 2018.
2. **R. Zhang,** G. Naughton, Y. Zhang, "An integrated scheme for unsteady cardiovascular hemodynamics research," presented at First Annual Symposium on Joint NDSU-UND Biomedical Engineering Graduate Programs, Fargo, ND, US, 2018.
3. **R. Zhang,** Y. Zhang, "An experimental study of pulsatile flow in natural and artificial aortic valves under varied heart rates," presented at Second Annual Joint NDSU-UND Biomedical Engineering Symposium 2018, Grand Forks, ND, US, 2018.
4. **R. Zhang,** Y. Zhang, "Pulsatile flow characteristics in a stenotic aortic valve model: an in vitro experimental study," presented at ASME-JSME-KSME 2019 8th Joint Fluids Engineering Conference, San Francisco, CA, US, 2019.
5. **R. Zhang,** Y. Zhang, B. Eichholz, "An Experimental Study of Pulsatile Flow over Rectangular Sidewall Cavities," presented at APS DFD Conference, November 2019, Seattle, WA, US, 2019.